2022

A GLOBAL SURVEY OF VOLCANIC SO2 EMISSIONS AND HEAT FLUX MEASURED FROM SPACE

Nelmary Rodríguez-Sepúlveda
Michigan Technological University, nrodrgue@mtu.edu

A GLOBAL SURVEY OF VOLCANIC SO_2 EMISSIONS AND HEAT FLUX MEASURED FROM SPACE

By

Nelmary Rodríguez-Sepúlveda

A THESIS

Submitted in partial fulfillment of the requirements for the degree of

MASTER OF SCIENCE

In Geology

MICHIGAN TECHNOLOGICAL UNIVERSITY

2022

This thesis has been approved in partial fulfillment of the requirements for the Degree of MASTER OF SCIENCE in Geology.

Department of Geological and Mining Engineering and Sciences

Thesis Advisor:	*Simon A. Carn*
Committee Member:	*Snehamoy Chatterjee*
Committee Member:	*Greg Waite*
Department Chair:	*Aleksey Smirnov*

Contents

List of Figures

Acknowledgements

I would like to thank Dr. Simon A. Carn for his guidance and patience during these past two and a half years, and Katie Nelson, Edwin Irizarry, Cristhian Salas, Dr. Luke Bowman and Dr. John Gierke for their ongoing support and friendship. I would also like to thank the Michigan Space Grant Consortium for providing me with the opportunity and funds to develop this project, and NASA for launching satellites we can use to improve volcanic monitoring.

Abstract

Over the past two decades, the availability of satellite measurements of volcanic gas emissions and heat flux has driven the development of new methodologies to improve global-scale volcano monitoring. In this work we explored the relationship between volcanic sulfur dioxide (SO_2) emissions and radiant heat flux (RHF) measurements from NASA's Ozone Monitoring Instrument (OMI) and Moderate Resolution Imaging Spectroradiometer (MODIS), respectively, to gain insight into how it associates to volcanic processes and eruption styles. The OMI SO_2 emissions data are derived from existing databases developed by using the methodology in Fioletov et al. (2016), which contain global, passive volcanic SO_2 degassing fluxes (PVF) for approximately 90-100 active volcanoes calculated at annual and seasonal intervals from 2005-2019 and 2005-2016, respectively. Volcanoes with available SO_2 flux datasets and measurable MODIS RHF data were identified using the University of Hawaii's near-time thermal monitoring of global hot-spots (MODVOLC) thermal alert system. The MODIS data was then integrated to match the annual and seasonal intervals at which the SO_2 fluxes were calculated and converted from RHF to Volcanic Radiative Energy (VRE). Both parameters were analyzed quantitatively by building seasonal and annual timeseries and studying how they changed together. This successfully allowed us to see a variety of activity patterns, including but not limited to identifying endogenic and exogenic behavior and transitions between the two states in certain volcanoes. In addition, the VRE and SO_2 annual and seasonal data was subjected to a simple linear regression analysis, through which we assessed the strength of the relationship given different types of activity, silica compositions and temporal scales. For example, we looked at six felsic dome/flow volcanoes with higher silica content products whose regressions using annual data returned a strong correlation that weakened when using their seasonally integrated data. Seven of the volcanoes with stronger correlations were used to extrapolate SO_2 values from 2000-2005 (prior to the launch of the OMI satellite) based on 2000-2005 MODIS heat emissions data. Given the general lack of SO_2 data for that period, it was not possible to corroborate the values and additional studies must be conducted to determine this method's feasibility. Finally, we conducted an "excess" sulfur analysis where we quantitatively compared melt inclusion-derived sulfur content and total degassed sulfur estimates from 15 volcanoes which also returned high VRE-SO_2 correlations. Our results show that there is no clear relationship between tectonic environments, magma composition or activity type (individually) and the amount of "excess" sulfur emitted by a volcano. Additional analyses are needed to determine if any specific combination between these could produce a higher correlation.

1 Introduction

Volcanic sulfur dioxide (SO_2) emissions data and radiant heat flux (RHF) measurements from satellite instruments have individually proven essential for monitoring changes in volcanic activity. The nature and extent of the relationship between these parameters, however, has not been established on a global scale. This study aims to address this by analyzing satellite measured SO_2 emissions and volcanic radiative energy (integrated RHF; VRE) data from 56 active volcanic systems with varying activity type and latitude that show both continuous SO_2 degassing and persistent heat flux detectable from space (Figure 1). We expect the correlation between these parameters (and its temporal variation) obtained from simple linear regression analyses to provide insight into the nature of volcanic unrest, e.g., 'open-system' SO_2 degassing from active lava lakes should yield a strong correlation between SO_2 emissions and VRE, whereas degassing from a deeper magmatic source may yield a weaker correlation (or no detectable VRE signal). We also expect that time series analyses of these parameters integrated at identical timescales will help identify transitions from primarily endogenous (or non-eruptive) to primarily exogenous (or eruptive) activity, and vice versa, during eruption sequences, with implications for volcanic hazards and volcano growth.

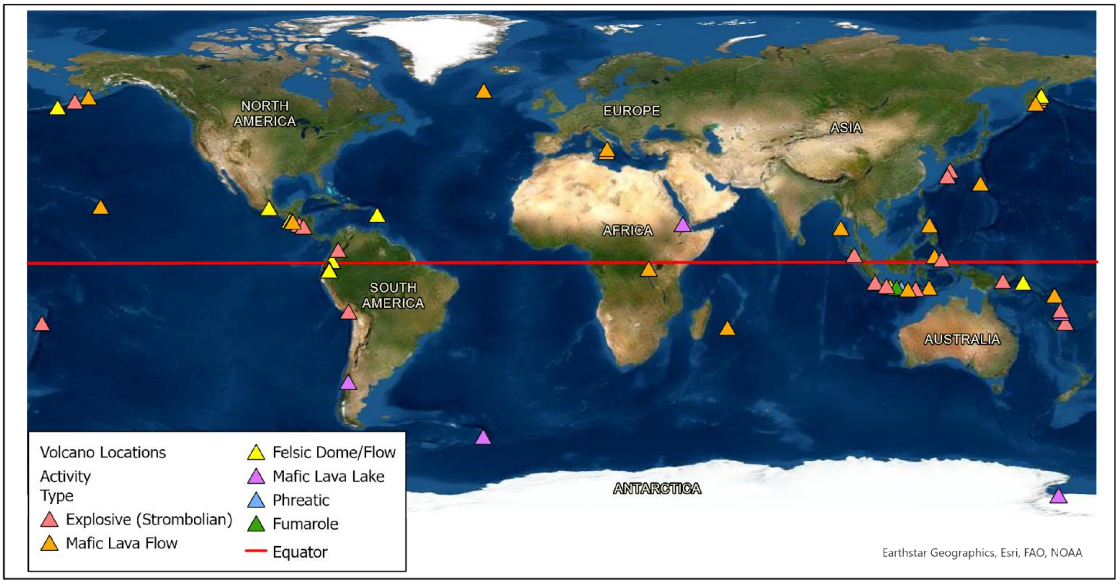

Figure 1. Global map showing the locations of all the volcanoes used for this study and their main type of activity.

The SO_2 emissions and RHF measurements used for this investigation come from NASA's Ozone Monitoring Instrument (OMI) and Moderate Resolution Imaging Spectroradiometer (MODIS) instruments, respectively. The annual and seasonal SO_2 emission data (ranging from 2005-2009 and 2005-2015) had been previously processed by Fioletov et al. (2016). RHF measurements for each volcano were downloaded via the University of Hawaii's MODVOLC thermal alert system website (http://modis.higp.hawaii.edu/) and were integrated to match the time frames of the OMI SO_2 data.

Our understanding of how sulfur content influences volcanic activity is limited by our ability to obtain physical samples of erupted material that contain intact melt inclusions (Shinohara, 2008). This results in gaps in scientific knowledge for volcanoes that are particularly dangerous or difficult to reach. In addition to comparing the interaction between SO_2 emissions and VRE, volcanoes with high correlation coefficients resulting from the SO_2-VRE simple linear regressions will be subjected to an excess sulfur analysis.

"Excess" sulfur refers to the difference between the amount of degassed sulfur and the amount of sulfur measured in inclusions within erupted magma (the first of which is often much more abundant) (Shinohara, 2008). Shinohara (2008) explains that many volcanoes emit more gasses than can be dissolved in magma during volcanic activity (e.g., explosive, or effusive eruptions, passive degassing, etc.). The offset between what is degassed and what remains trapped in inclusions can therefore be attributed to degassing from unerupted magma deep within the system (Shinohara, 2008).

We calculated an estimate of the amount of remotely sensed degassed sulfur for volcanoes that show a robust SO_2-VRE relationship (i.e., where SO_2 degassing and magma eruption correlate highly at given timescales) by using each volcano's radiant density, or c c_{rad} (in J/m^3). A volcano's c_{rad} value draws a relationship between a lava body's silica content and its ability to radiate heat based on how it changes its area to insulate its inner core (Coppola et al., 2013). Because the ratio of thickness to eruption duration will vary equitably along with changes in insulation conditions during a given eruption, Harris et al (2010) explains that we can assume that the c_{rad} will remain constant throughout an eruptive event (Coppola et al., 2013). This assumption allows us to draw proportionality between the volume of erupted material and the eruption's VRE:

$$Vol = \frac{VRE}{c_{rad}} \quad (1)$$

Coppola et al.'s (2013) visualization of this relationship is shown in Figure 2a. This plot shows a distinct grouping of a variety of eruptions from different volcanoes according to lava composition, with only slight overlap between intermediate and basic lava types. When plotting the c_{rad} values against SiO_2 content (Fig 2b), this distinction is highlighted and the following equation is drawn to summarize the inverse relationship between lava composition and radiant density (Coppola et al., 2013):

$$c_{rad} = 6.45 \times 10^{25} \times (X_{SiO_2})^{-10.4} \quad (2)$$

The resulting degassed S estimates are compared to the amounts of expected sulfur measured in melt inclusion analyses described in the literature for each volcanic source.

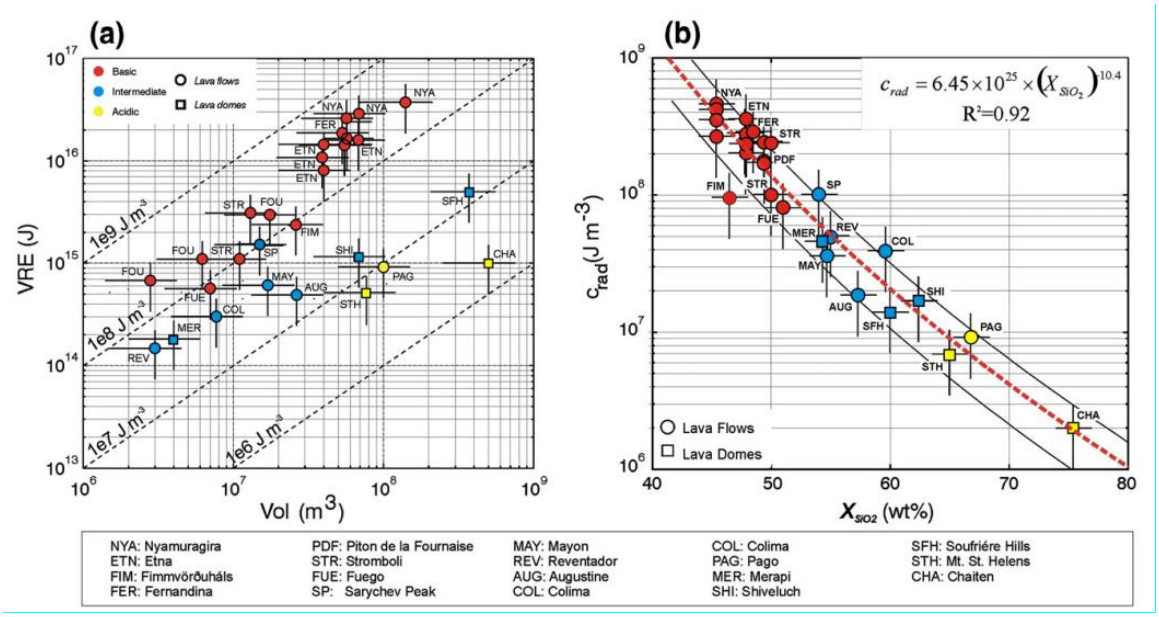

Figure 2. Coppola et al's (2013) radiant density (c_{rad}) data visualization. (a) Shows distinct groupings of volcanic eruptions VRE and volume data according to silica composition. (b) Shows the regression used to draw the relationship between silica content and c_{rad}.

2 Data

2.1 Surface Radiant Heat Flux measurements

NASA's MODIS (Moderate Resolution Imaging Spectrometer) instruments on the Terra and Aqua Earth Observing System (EOS) platforms can measure the surface radiant heat flux of all Earth's subaerial volcanic eruptions (Wright, 2016). Their 2,330 km viewing swath allows them to view the entire Earth's surface every 24-48 hours (https://modis.gsfc.nasa.gov/data/) and enables them to provide the global, near real-time imaging needed to identify and record thermal volcanic signals emitted by active lava bodies (Wright, 2016).

The RHF raw data corresponding to the period of study used for this project are available from the University of Hawaii's MODIS Volcano Thermal Alert System (MODVOLC) website (http://modis.higp.hawaii.edu/). The MODVOLC algorithm (operational since February 28, 2000) analyzes Level 1B MODIS data pixel by pixel to identify volcanic thermal anomalies. (Wright et. al, 2015; Zacksek et al., 2014; Wright, 2016) and uses Planck's Blackbody Radiation Law to draw the relationship between spectral radiance (L_λ, W m^{-2} sr^{-1} μm^{-1}) a nd kinetic temperature (Wright et al., 2015; Wright, 2016). The base equation for this relationship defines spectral radiant exitance (M_λ) and is written as follows (Wright, 2015):

$$M_\lambda = \frac{c_1}{\lambda^5(e^{c_2/\lambda T}-1)} \qquad (3)$$

In the equation above, M_λ is the spectral radiant exitance (in W m^{-2} sr^{-1} μm^{-1}), c_1 and c_2 are radiation constants (valued at Wm^{-2} μm^4 and μm K, respectively), λ is the wavelength (in μm) and T is temperature (in K) (Wright, 2016). Spectral radiance ($L\lambda$) can then be calculated by dividing $M\lambda$ by π (Wright, 2016).

Because of operational constraints on the MODIS volcano product, the algorithm had to be designed as a point operation (i.e., it requires pixels containing thermal anomalies to be analyzed in relation to neighboring pixels). The data for this analysis comes from two long-wave infrared (LIR) passbands centered at 11.03 μm and 12.02 μm, and one middle-wave infrared (MIR) passband centered at 3.959 μm (Wright, 2004). The difference between the MIR and LIR passband allows greater distinction between heat emitted from active lava bodies and background spectral radiance. However, it is not enough to discriminate between volcanically emitted radiances and background radiances when the lava body's area is sub-pixel sized (i.e., < $1km^2$) (Wright, 2015). To remedy this, MODVOLC normalizes the difference between the emitted LIR and MIR spectral radiances (Wright et. al, 2015). A Normalized Thermal Index (NTI) is calculated using the following equation:

$$NTI = (L_{3.959} - L_{12.06})/(L_{3.959} + L_{12.06}) \quad (4)$$

where $L_{3.959}$ and $L_{12.06}$ are the spectral radiances of the bands centered at 3.959 μm and 12.02 μm, respectively (Wright et. al, 2015; Zacksek et al., 2014; Wright, 2016). To reduce the number of false positives and measurement variation from imaging volcanoes at different latitudes or imaging a volcano in different seasons, a single NTI threshold is used to classify volcanic thermal anomalies, or hotspots, within MODIS data (Wright, 2016). The MODVOLC team drew the threshold at -0.80 NTI after an empirical analysis of 300 MODIS images selected from around the world (Wright, 2016). The results showed that

active lava sources had NTI's greater than -0.85 NTI (Wright, 2016). However, the possibility of false positives was much greater than the possibility of overlooking low intensity hotspots and it was decided that the threshold should remain at -0.80 to increase the precision of the algorithm (Wright, 2016).

The MODVOLC algorithm also converts the 3.959 μm spectral radiance measured in each hotspot pixel into a radiant heat flux measurement (in $_e$, in Watts, or J s^{-1}) via the following relationship (Wooster et al., 2003; Wright et al., 2015):

$$\phi_e = 1.89 \times 10^7 (L_{3.959} - L_{3.959,\mathrm{bg}}) \qquad (5)$$

where $L_{3.959,\,bg}$ is the spectral radiance emitted from pixels neighboring a hotspot., which are used to account for the background temperatures when the hotspot is sub-pixel sized (Wright et al., 2015).

The observation time, coordinates, spectral radiances (in W m^{-2} sr^{-1} μm^{-1}) at MODIS's three wavelengths (3.959 μm, 11.03 μm, 12.02 μm) of all detected "hotspots" are automatically uploaded to the MODVOLC website (Wright et. al, 2015). The data also contains an "Excess" column. According to the MODVOLC website, this "Excess" is expressed in W m^{-2} sr^{-1} μm^{-1} and is obtained by comparing the measured spectral radiance to the expected temperature for a specific location (http://modis.higp.hawaii.edu/contents.html). This project follows the methodology of Wright et al. (2015) and uses the excess radiation exclusively from MODIS nighttime measurements to reduce the influence of sunlight or solar heating contamination. Above-background heat fluxes (i.e., volcanogenic RHF) of over 50 volcanoes at varying latitudes were then located.

Some of the MODIS sensor's sources of uncertainty are directly associated with its geometric constraints. For example, MODIS's ground-projected instantaneous field of view (GIFOV) can be affected by its ± 55° viewing swath, increasing the error of radiance measurements in topographically "hidden" locations. Because of this, radiance measurements for hotspots inside volcanic craters are subject to underestimation. In addition, meteorological clouds or thick volcanic plumes are also capable of obstructing hotspot features (Flower and Carn, 2015).

2.2 SO_2 flux measurements

SO_2 is typically the third most abundant gas in volcanic emissions, preceded by water vapor ($H_2O_{(vapor)}$) and carbon dioxide (CO_2), respectively (Carn et al., 2016). A lack of background SO_2 in the atmosphere at volcanic emission altitudes and its ability to remain for up to hours or days in the atmosphere give it a trace gas quality that water vapor and CO_2 have not been able to attain (Carn et al., 2016). Volcanogenic SO_2 is, therefore, more easily distinguishable from background noise than its counterparts and is essential for hazard mitigation (Carn et al., 2016).

SO_2 emissions serve as an indicator for changes in volcanic activity given that SO_2 fluxes tend to increase over time when juvenile magma is injected into a volcanic system (Carn et al., 2013; Theys et al.; 2013, Rodriguez, 2019). SO_2 can also build up underneath a plug when magma crystallizes in the upper conduit, creating a seal and causing an increase in pressure (Theys et al., 2013; Rodriguez, 2019). Theys et al. (2013) explains that both cases might signal an oncoming eruption (Rodriguez, 2019). On the other hand, a gradual decrease in SO_2 levels due to volatile exhaustion or decreasing permeability caused

by hydrothermal mineral precipitation in the upper conduit can lead to reduced volcanic activity (Stoiber et al., 1983; Edmonds et al., 2003; Theys et al., 2013; Rodriguez, 2019). SO_2 also often oxidizes when coming into contact with other plume particles or atmospheric constituents and creates sulfate aerosols, which can become environmental and health hazards (Theys et al., 2013; Rodriguez, 2019).

The SO2 emissions data to be used in this project are available in existing databases (Fioletov et al., 2016; Carn et al., 2017), which contain global SO_2 passive volcanic degassing measured using NASA's Ozone Monitoring Instrument (OMI) onboard the Aura satellite. Rodriguez (2019) describes the characteristics of the OMI satellite as follows:

> "The Ozone Monitoring Instrument (OMI) is a UV/visible spectrometer launched aboard NASA's Aura Satellite in 2004, capable of measuring atmosphere-backscattered sunlight (OMI Team, 2009). Aura's sun synchronous orbit is repeated every 16 days, such that OMI can complete global coverage in 24 hours (OMI Team, 2009). The instrument has a spectral range between 264 nm and 504 nm, with a resolution between 0.42 nm and 0.63 nm. The spatial resolution is 13 x 24 km at nadir (OMI Team, 2009) Although originally built to measure ozone (O_3), OMI has proven useful for detecting SO_2 because, much like O_3, it also absorbs UV radiation at 310-315 nm (Vandaele et al., 1994)."

OMI data collected in 2005-2019 were processed using a Principal Component Analysis (PCA) algorithm (Li et al., 2013) to produce a low-noise, operational OMI planetary boundary layer (PBL) SO2 product (Fioletov et al., 2016).

The resulting SO_2 data were used to estimate annual and seasonal emissions of each volcanic source or paired source detectable by OMI (Fioletov et al., 2016). Paired sources are clusters of volcanoes that are within OMI's spatial resolution (~13 x 24 km) and whose emissions therefore cannot be individually discriminated (e.g. Nyiragongo and Nyamuragira volcanoes, D.R. Congo) (Carn et al., 2017).

There are three main sources of error for these SO_2 flux estimates: the input values and assumptions attached to the air mass factor (AMF) calculations, the error attributed to the linear regression model used to estimate the total SO_2 mass, and the error resulting from fitting the model (Fioletov et al., 2016).The algorithm additionally excludes the great majority of measurements acquired while there was snow on the ground given that it does not account for snow albedo (Fioletov et al., 2016). Some error in the final estimates may also be attributed to gaps in the imagery on aleatory dates caused by the OMI's Row Anomaly (ORA), which affects all OMI data retrieved after June 25th, 2007 (OMI Team, 2009; Carn et al. 2013; Rodriguez, 2019).

The total error for the annual SO_2 estimates adds to 55% for sources emitting over 100 kt/yr and >67% for those emitting under 50 kt/ yr (Fioletov et al., 2016; Carn et al., 2017). A full description of the associated error percentages and error sources for the annual SO_2 estimates arising from the PCA algorithm is available in Fioletov et al. (2016).

3 Methods

3.1 Assumption of Linearity

Our investigation is built on the assumption that there is a linear relationship between volcanic SO_2 emissions and VRE. Although this relationship has not been explicitly discussed in previous literature, there is theoretical evidence that points to linearity between each of these parameters and lava effusion rate.

The linear relationship between SO_2 emissions and volumetric lava effusion rate is based on evidence of these two occurring at similar rates during effusive eruptions, assuming constant melt density and sulfur content (Carn, 2016). This relationship was initially tested with ground based SO_2 measurements. For example, Carn (2016) mentions that Sutton et al. (2003) quantitatively summarized this theoretical relationship by applying the following equation to ground based SO_2 emission rates from Kilauea:

$$E_{SO_2} = V_m W_{SO_2} \rho_m \qquad (6)$$

where E_{SO_2} is the SO_2 emission rate (metric tons/day), V_m is the rate of volumetric lava effusion (m^3/day), W_{SO_2} is the fraction of degassed SO_2 per mass unit of erupted magma and ρ_m is lava density in m^{-3} (Carn, 2016). A decade later, Koeppen et al. (2013) also conducted investigation in Kilauea and reimagined the equation as:

$$V_m = E_{SO_2} K_d \qquad (7)$$

where K_d is equal to the reciprocal of $W_{SO_2} \times \rho_m$ (Carn, 2016).

With the increasing availability of satellite-based SO_2 measurements, it was necessary to incorporate a variable that accounted for the space-detected fraction of SO_2. Given this new information, Carn (2016) extended the equation to:

$$V_m = \frac{1}{f_v} E_{SO_2} K_d \qquad (8)$$

where f_v is an estimate of the amount of SO_2 detected by satellite data.

Coppola et al. (2013) argues that the relationship between VRE and time-averaged lava discharge rates (TADR) is tied by the radiant density parameter (c_{rad}). According to Harris et al. (2010) c_{rad} is constant independently of insulation conditions. Assuming c_{rad} remains constant, the relationship can be summarized in Equation 1 (Coppola et al., 2013).

3.2 SO2 vs. VRE Time Series and Regression Analysis

Integration of the RHF data with respect to time yields an estimate of the total volcanic radiative energy (VRE, in Joules). The RHF data for individual eruptive events at each volcano (considered finalized after seven days) were collected and integrated over two timescales (annually and seasonally) to match those of the OMI detected SO_2 emission secondary data used for this investigation. In this instance, "seasonal data" refers to three-month periods starting in December (e.g., December-February, March-May, etc.). The resulting VRE and SO_2 emissions data for the volcanoes were then plotted on time series graphs to study how the parameters changed together qualitatively at each volcano on an annual and seasonal basis (Figure 3). In addition to being analyzed individually, four of these volcanoes (Nyamuragira, Nyiragongo, Fuego and Pacaya) were analyzed as pair sources due to their geographical proximity (< 50 km apart) and the OMI satellite's inability to separate their individual SO_2 emissions data. In these cases, the VRE values of

each were added (i.e., Nyamuragira and Nyiragongo; Fuego and Pacaya) and analyzed as a single volcanic system. The volcanos Raung and Ijen are also geographically close enough to be considered a source pair within the OMI data, but were not analyzed as such given that reports from the Smithsonian Institution Global Volcanism Program (GVP) website (https://volcano.si.edu/) confirm that Raung did not degas significant amounts of SO_2 during the study period. It was thus considered reasonable to analyze data from Ijen individually.

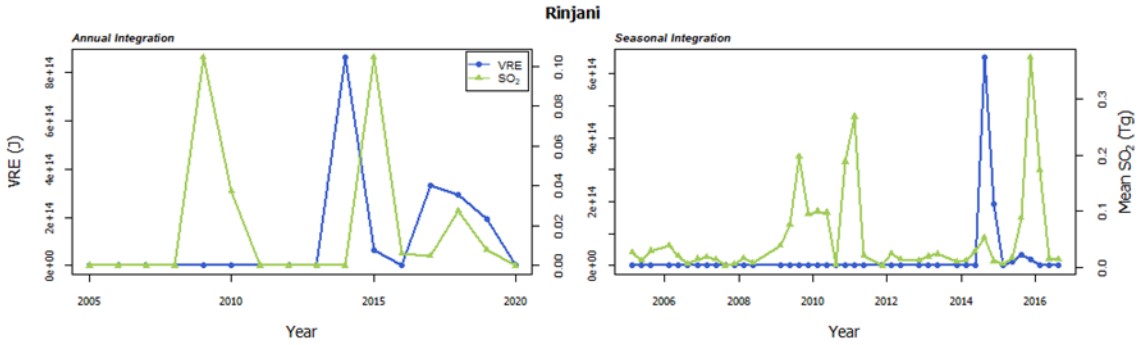

Figure 3. SO_2 flux (green) and VRE (blue) time series of Rinjani volcano drawn at annual and seasonal intervals.

The VRE and SO_2 emissions data for each volcano or source pair was further subjected to a simple linear regression analysis conducted in the R programming language. Each of the volcanoes was classified according to their main activity type following the identification method used by Coppola et al. (2013) using information from the general information section in volcano profiles in the GVP website. The correlation coefficients were then analyzed in terms of the volcanoes' latitude and activity type. The volcanoes were classified into six groups according to their main activity type using the following acronyms: mlf (mafic lava flows), ex (explosive; mainly strombolian), fdf (felsic domes or flows), fum (fumarolic), mll (mafic lava lakes), phr (phreato-magmatic) or pair (pair source).

3.3 Excess Sulfur Analysis

"Excess" sulfur calculations provide insight into the offset between inclusion-derived sulfur content measurements and the total, satellite-measured amount of sulfur degassed during an eruption (Shinohara, 2008). The goal of this analysis is to estimate the fraction of degassed sulfur of 15 volcanoes exhibiting a high VRE-SO_2 correlation coefficient ($R^2 > 0.25$) in their regression analysis and compare it to sulfur measurements derived from melt inclusion studies reported in the literature. Only the regression with a higher correlation coefficient will be selected for this analysis.

To obtain the mass fraction of degassed sulfur (S), we first calculated each volcano's radiant density (c_{rad}) using an SiO_2 (wt %) value representative of their magma composition into equation #. These SiO_2 wt % values were obtained from the literature or by calculating a modal SiO_2 concentration from whole rock analyses conducted on recent eruptive products (no older than a century, depending on available data) and reported in the GEOROC database (https://georoc.eu/.). Having obtained the c_{rad} values for each

volcano, we calculated a range of degassed SO_2 mass (M_{SO_2}, in Tg/kg) using the following equation:

$$\left(\frac{c_{rad} \times m}{\rho_{min-max}}\right) = M_{SO_2} \quad (9)$$

where m is the slope of the VRE-SO_2 regression line (in Tg/J) calculated in the regression analysis, and $\rho_{min\text{-}max}$ is the corresponding magma density range (in kg/m^3) according to silica composition (Farooq, 2021). The reciprocal of the resulting maximum and minimum degassed SO_2 masses were then multiplied by 5×10^8 kg/Tg (to convert SO_2 mass to sulfur (S) mass) and converted to ppm. These values were then compared to melt inclusion-derived sulfur measurements.

A ±50% error is associated with the c_{rad} calculation and is mainly attributed to uncertainties in erupted volume measurements and variability in eruption thickness, insulation conditions and duration (Coppola et al., 2013). There is additional error stemming from the calculation of representative silica contents and magma densities in this investigation, as well as from the individual inclusion-derived S estimates. Descriptions of the errors associated with the individual S inclusion-derived values can be found in the literature.

3.4 SO_2 value extrapolation (2000-2005)

Seven of the volcanoes were chosen to extrapolate preliminary annual or seasonal estimates of sulfur dioxide emissions before the launch of the OMI satellite (2000-2004) based on their VRE for the same time period. Barren Island and Piton de la Fournaise were analyzed based on their seasonal data; Bagana, Popocatepetl, Kliuchevskoy, Santiaguito (Santa María) and Erta Ale were analyzed based on their annual data. Each volcano's dataset was chosen for the purpose of predicting SO_2 flux values from January 2000 until December 2004 by using the timeframe that would reasonably maximize the number of points available for each regression. Statistical methods were then used to calculate 95% confidence and prediction intervals associated with the regressions.

The volcanoes were selected based on whether their regression analyses yielded good correlation coefficients ($R^2 > 0.40$) on either seasonal or annual time frames, or both. In the last case, only the data with a higher correlation coefficient was used. The data selected also needed to show significant variation in the time series patterns for the extrapolations to be significant. For example, the simple linear regression for the Kizimen data yielded excellent correlation coefficient in both time frames but was not used in this analysis because their regression lines were controlled by a single point representing a greater-magnitude, isolated event (Figure 4). Data from Sangeang Api and Sinabung were not used for this analysis on the same basis.

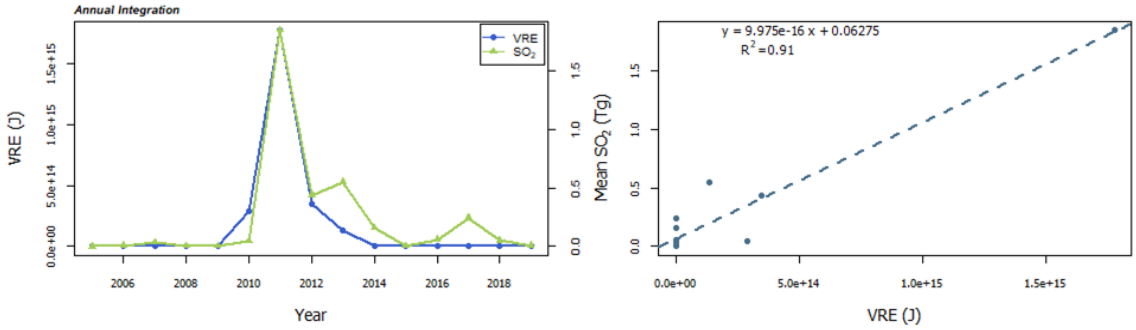

Figure 4. Kizimen's annual regression yields a 91% correlation dependent on a single, isolated event. Because of this, its VRE data was not selected for predicting mean SO_2 flux values prior to 2005.

4 Results

4.1 SO_2 vs. VRE simple linear regressions

The results of the SO_2 vs. VRE annual and seasonal regression analyses for the individual and source pair volcanic systems are shown in Table 1. 19 of the 55 volcanoes studied in this investigation exhibited mainly mafic lava flow activity, 18 exhibited explosive (strombolian) activity, 10 showed mainly felsic dome/flow extrusion, 6 had active mafic lava lakes, 1 exhibited fumarolic activity and 1 was mainly phreatomagmatic in nature. In addition, two source pairs were analyzed as single volcanic sources (Nyamuragira and Nyiragongo; Fuego and Pacaya). In terms of latitudinal distribution, 37 of the individual volcanoes (not source pairs) are found in tropical regions, 3 are in subtropical latitudes, 14 are in temperate regions and 1 is located within the Antarctic Circle. Figure 5 shows the distribution of correlation values according to each volcano or source pair's latitude and activity type when analyzing the data in annual and seasonal timeframes, respectively. Figure 5 shows that 25 volcanoes returned correlation coefficients $R^2 \geq 0.25$ when analyzing the VRE-SO_2 relationship in annual intervals. Only 15 volcanoes have $R^2 \geq 0.50$: 3 of them exhibit mafic lava flows, 4 show explosive behavior, 6 show felsic dome/flow activity and 2 have lava lakes. As for the source pairs, Fuego and Pacaya showed an annual 37% correlation, and Nyiragongo and Nyamuragira returned NA due to lack of SO_2 or heat emission data, or both.

Figure 5 shows the correlation coefficients of the VRE-SO_2 regressions of the seasonally integrated data. The number of volcanoes whose correlation coefficient surpasses 0.25 decreases from 25 in the annually integrated data to 11 in the seasonally integrated data. Furthermore, there are only 6 volcanoes that show more than a 50% correlation; half of them mainly exhibit mainly mafic lava flow activity and, the other half, explosive activity. Finally, there was no SO2 and/or heat emissions data to conduct a regression analysis on the Fuego and Pacaya source pair; the Nyiragongo and Nyamuragira source pair returned less than a 5% correlation.

Table 1. Shows the latitudes and summary statistics of the annual and seasonal regressions of 55 volcanoes and two source pair volcanic systems. The statistics include correlation coefficients (R^2), the standard error of the regression (RSE), P-values, and whether the regression line slope was positive (+) or negative (-). Activity types are abbreviated as follows: explosive/strombolian activity (ex), felsic domes/flows (fdf), mafic lava flows (mlf), mafic lava lakes (mll), phreatomagmatic (phr), fumarolic (fum). All statistics that were unable to be calculated due to lack of either SO_2 emissions data, heat emissions data, or both are marked "NA".

			Annual Regression				**Seasonal Regression**			
Volcano	**Lat.**	**Act. Type**	**R^2**	**RSE**	**P value**	**m (+/-)**	**R^2**	**RSE**	**P value**	**m (+/-)**
San Miguel	13.42	ex	NA	NA	NA	NA	NA	NA	NA	NA
Kizimen	55.12	ex	0.91	0.148	0	+	0.88	0.225	0.89	+
Sangeang Api	-8.21	ex	0.78	0.017	0	+	0.75	0.039	0	+
Sabancaya	-15.8	ex	0.74	0.073	0	+	0.77	0.089	0	+

Sinabung	3.17	ex	0.66	0.124	0	+	0.6	0.2	0	+
Yasur	-19.53	ex	0.49	0.186	0.002	+	0.02	0.356	0.023	+
Langila	-5.53	ex	0.44	0.134	0.007	+	0.19	0.3	0.008	+
Tungurahua	-1.47	ex	0.33	0.079	0.026	+	0.14	0.147	0.03	+
Nevado del Ruiz	4.9	ex	0.24	0.323	0.064	+	0.07	0.589	0.177	+
Dukono	1.68	ex	0.21	0.178	0.087	-	0.04	0.374	0.085	-
Sakurajima	31.59	ex	0.13	0.217	0.182	+	0.37	0.284	0.118	+
Krakatau	-6.11	ex	0.11	0.07	0.224	+	0.09	0.126	0.222	+
San Cristobal	12.7	ex	0.08	0.1	0.295	-	0	0.154	0.745	-
Aoba	-15.4	ex	0.05	0.468	0.429	+	NA	NA	0.425	NA
Shishaldin	54.76	ex	0.03	0.09	0.529	-	0.29	0.117	0.677	+
Tofua	-19.75	ex	0	0.038	0.808	-	0	0.051	0.369	+
Suwanosejima	29.64	ex	0	0.12	0.84	-	0.02	0.216	0.73	+
Slamet	-7.24	ex	0	0.044	0.969	+	0.01	0.181	0.954	-
Semeru	54.76	fdf	NA	NA	NA	NA	0	0.46	0.968	-
Galeras	1.2	fdf	0.88	0.033	0	+	0.15	0.137	0	+
Popocatepetl	19.02	fdf	0.86	0.124	0	+	0.15	0.499	0	+
Merapi	-7.56	fdf	0.81	0.008	0	+	0.01	0.138	0	+
Bagana	-6.09	fdf	0.72	0.24	0	+	0.31	0.527	0.002	+
Soufriere Hills	16.72	fdf	0.61	0.179	0.001	+	0.39	0.283	0.001	+
Santiaguito	14.76	fdf	0.55	0.023	0.002	+	0	0.071	0.002	-
Sangay	-2.01	fdf	0.08	0.027	0.275	+	NA	NA	0.001	NA
Shiveluch	56.64	fdf	0.03	0.118	0.501	+	0.09	0.175	0.682	+
Cleveland	52.83	fdf	0.01	0.047	0.708	+	NA	NA	0.708	NA
Arjuno	-7.733	fum	0.01	0.051	0.678	-	NA	NA	NA	NA
Batu Tara	-7.79	mlf	NA	NA	NA	NA	0	0.116	0.669	-
Montagu	58.42	mlf	0.86	0.021	0	+	0.07	0.146	0	+
Mayon	13.26	mlf	0.72	0.067	0	+	0.44	0.097	0	+
Piton de la Fournaise	-21.23	mlf	0.7	0.04	0	+	0.68	0.073	0	+
Barren Island	12.28	mlf	0.49	0.076	0.004	+	0.6	0.127	NA	+
Kliuchevskoy	56.06	mlf	0.44	0.17	0.005	+	0.04	0.682	0.001	+
Karangetang	2.78	mlf	0.43	0.048	0.006	+	0.11	0.054	0.005	+
Veniaminof	56.17	mlf	0.4	0.062	0.012	+	0.06	0.158	0.016	+
Fuego	14.47	mlf	0.38	0.047	0.008	+	0.06	0.056	0.007	+
Tinakula	-10.38	mlf	0.26	0.076	0.042	+	0.08	0.122	0.011	+
Nishinoshima	27.25	mlf	0.22	0.113	0.068	+	NA	NA	0	NA
Etna	37.73	mlf	0.15	0.264	0.134	+	0.15	0.265	0.281	+
Stromboli	38.79	mlf	0.04	0.027	0.44	+	0	0.085	0.586	+
Karymsky	54.05	mlf	0.03	0.129	0.527	+	0.05	0.195	0.689	+
Kilauea	19.42	mlf	0.02	1.057	0.632	+	0	1.283	0.625	+
Rinjani	-8.42	mlf	0.01	0.036	0.67	-	0	0.081	0.616	-

Pacaya	14.38	mlf	0.01	0.055	0.69	-	NA	NA	0.356	NA
Nyamuragira	-1.41	mlf	0	0.894	0.826	+	0.06	1.411	0.992	+
Reventador	38.79	mlf	0	0.063	0.882	-	0	0.221	0.875	-
Nyiragongo	-1.52	mll	NA	NA	NA	NA	0	1.457	NA	+
Erta Ale	13.6	mll	0.89	0.049	0	+	0.14	0.024	0	+
Erebus	-77.53	mll	0.54	0.007	0.001	+	0.1	0.008	0.002	+
Villarrica	-39.42	mll	0.27	0.044	0.048	+	0.08	0.129	0.075	+
Michael	-57.8	mll	0.14	0.02	0.173	-	0.04	0.093	0.124	+
Ambrym	-16.25	mll	0.12	0.993	0.204	+	0.03	1.508	0.218	+
Ijen	-8.06	phr	0.02	0.097	0.574	-	0.03	0.239	0.662	-
Nyamuragira + Nyiragongo	NA	pair	NA	NA	NA	NA	0.02	1.44	NA	+
Fuego + Pacaya	NA	pair	0.37	0.038	0.016	+	NA	NA	NA	NA

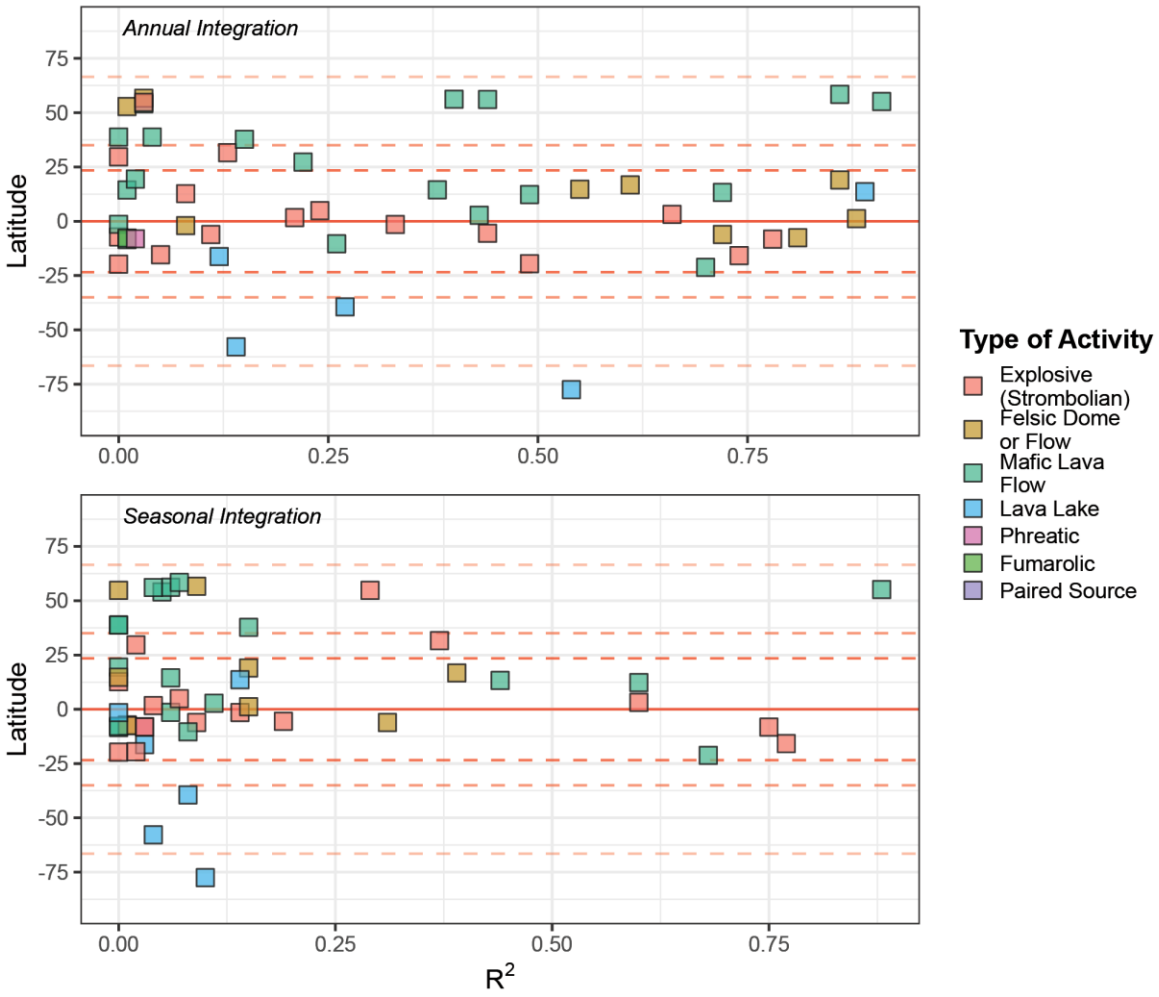

Figure 5. Shows the correlation coefficients (R^2) of the annual and seasonal regressions of each volcano plotted according to their latitudinal location (vertical scale) and type of activity (color range).

4.2 Time Series Analysis

The time series plots constructed during this investigation allow insight into several outstanding volcanic activity patterns. For example, the time series for Kizimen, Sabancaya, Sinabung, Sangeang Api volcanoes, whose regression analyses demonstrated high regression coefficients (~ $R^2 > 0.50$) in both the annual and seasonal regression analyses (Figures 6a-e), show strong, isolated peaks associated with activity that caused degassing and extrusion to occur at the same time and at similar rates (Figures 6b-d). The regression analysis for Piton de la Fournaise, whose activity is usually characterized by mafic lava flows, also returned elevated R^2 values both annually and seasonally (Michon et al., 2013). However, unlike the aforementioned volcanoes, its time series plots show multiple simultaneous peaks in VRE and SO_2 activity that occur at similar rates Figures 6e.

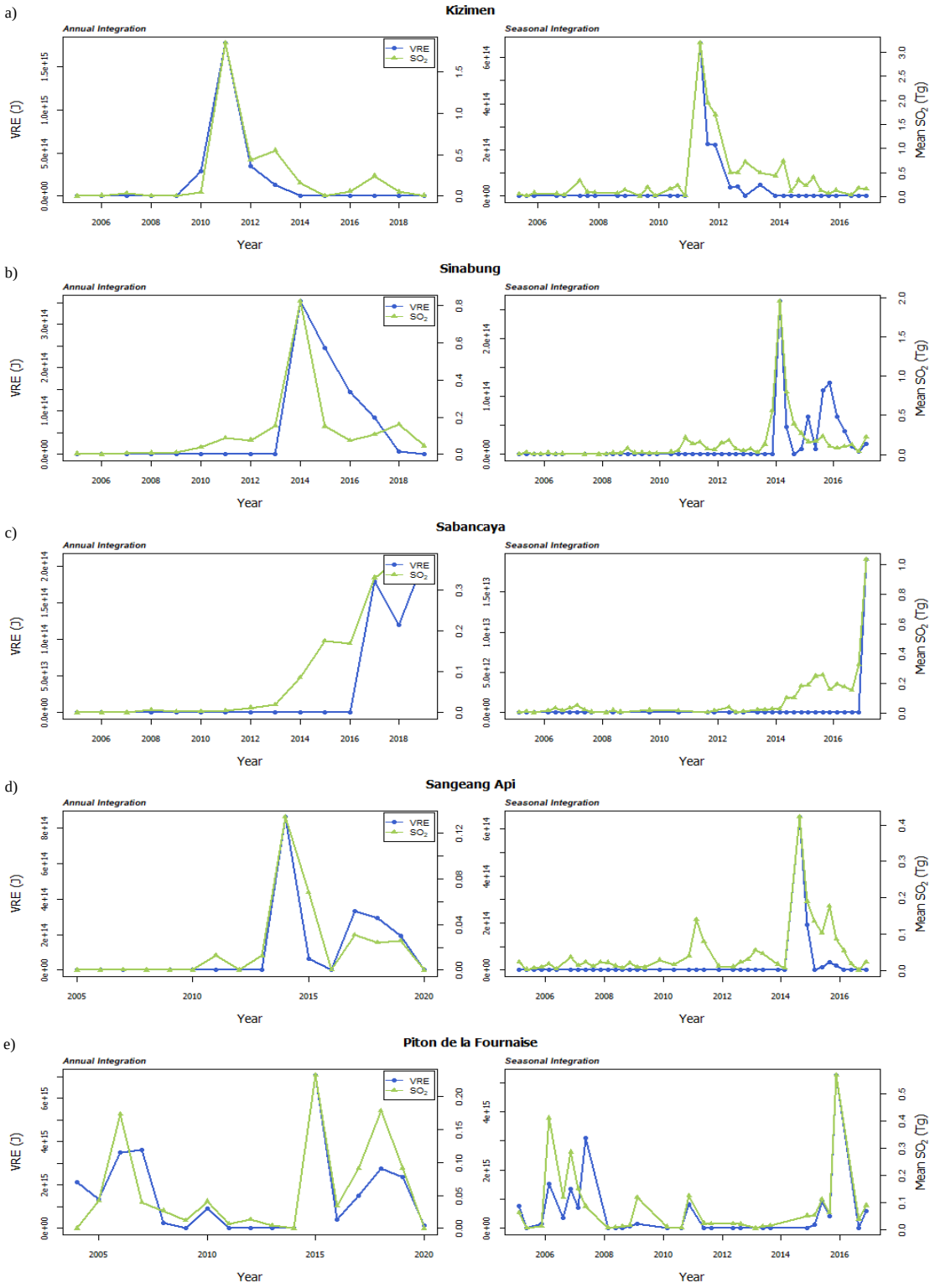

Figure 6. SO_2 flux (green) and VRE (blue) time series of Kizimen (a), Sinabung (b), Sabancaya (c) and Sangeang Api (d) and Piton de la Fournaise (e) volcanoes drawn at annual intervals (left-hand column) and seasonal intervals (right-hand column).

In addition, two thirds of the volcanoes exhibiting felsic dome or flow activity have high annual regression coefficients and qualitatively demonstrate a pattern that indicates similar simultaneous degassing and lava extrusion rates. However, this pattern is only visible in their annual time series (Figure 7). Furthermore, Soufriere Hills, Sangay and Cleveland did not return high correlation coefficients annually or seasonally and present predominant degassing activity. Sangay and Cleveland show multiple, degassing events where there was no lava extrusion. Soufriere Hills's predominant degassing activity is accompanied by proportional heat signals occurring at intervals equal to the degassing events, but at lower rates (Figure 8).

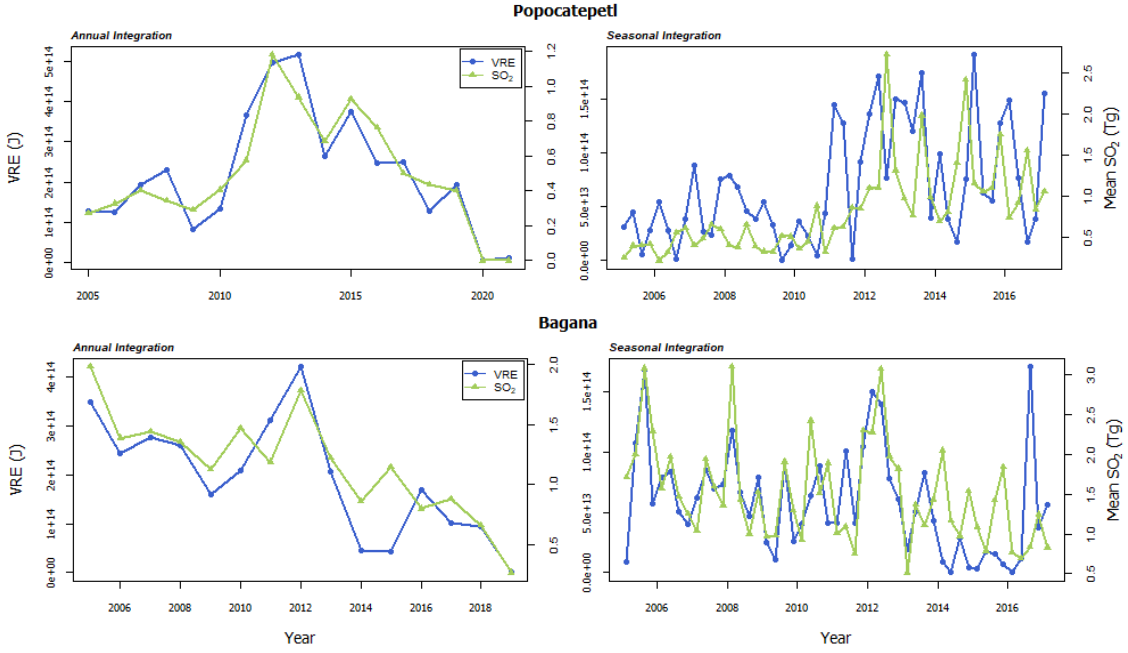

Figure 7. Showing the annual and seasonal SO_2 flux (green) and VRE (blue) time series plots for Popocatepetl and Bagana, two of the six felsic dome/flow volcanoes with high annual correlation coefficients and low seasonal correlation coefficients.

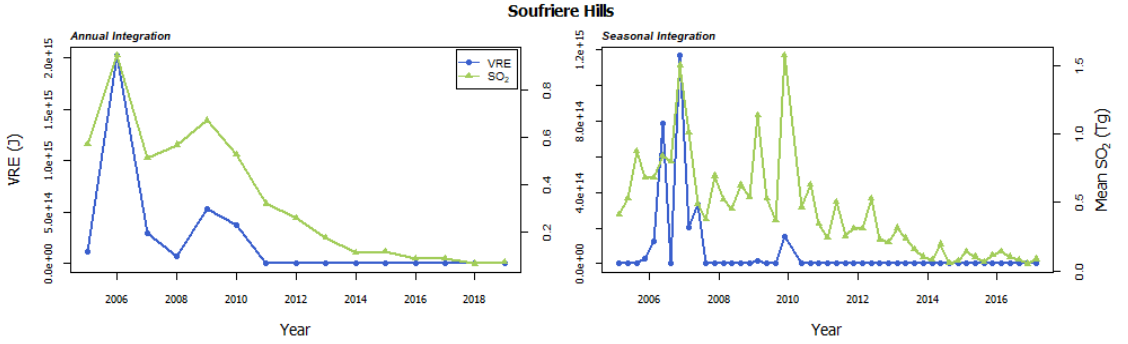

Figure 8. SO_2 flux (green) and VRE (blue) time series of Soufriere Hills drawn at annual and seasonal intervals.

Other cases, such as those of Kilauea and Ambrym, show long term, distinct transitions from mainly degassing activity to mainly eruptive activity that can be perceived in both the annual and seasonal time frames (Figure 9 a-b). The GVP (2013a), bulletin reports for Ambrym describe a general increase in lava flow forming eruptive activity beginning in July 2013. For Kilauea, the plots show that the same type of change occurs in early to mid-2013 and corresponds to initial lava flow activity from the Pu'u 'O'o cinder and spatter cone, and persistence of the Kilauea summit lava lake (GVP, 2013b).

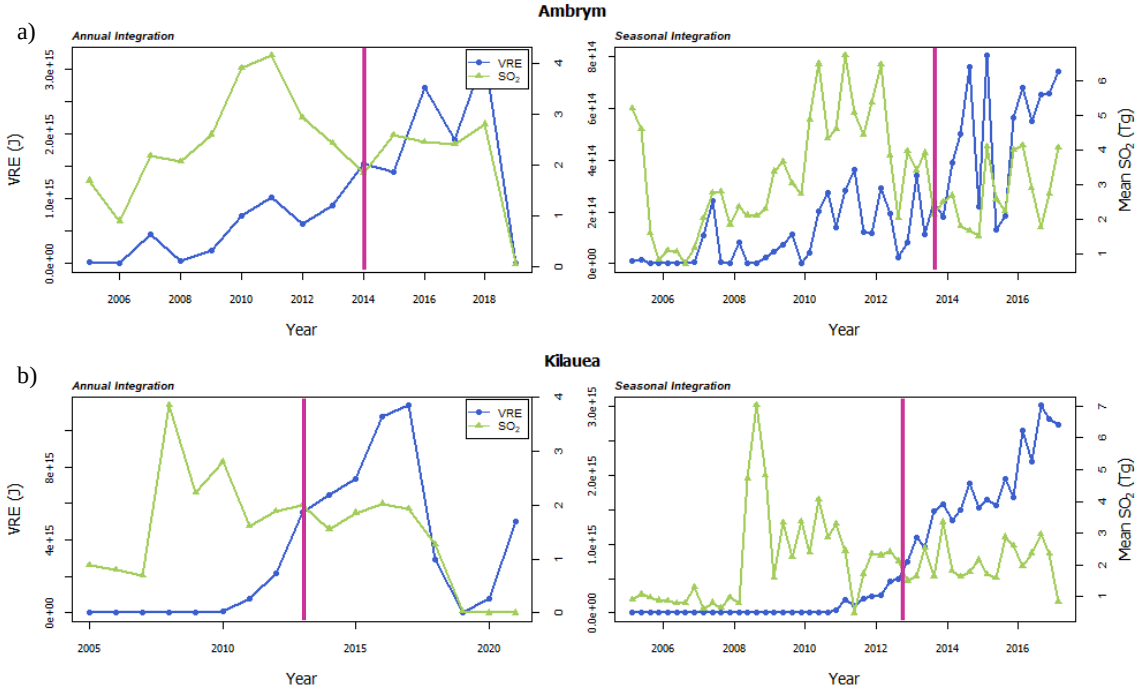

Figure 9. O_2 flux (green) and VRE (blue) time series of Ambrym (a) and Kilauea (b) volcanoes drawn at annual intervals (left-hand column) and seasonal intervals (right-hand column). The pink lines mark the approximated time periods where the activity transitioned from primarily degassing activity to primarily eruptive activity.

The time series for Shiveluch presents an inverted scenario to that of Ambrym and Kilauea, where lava-producing eruptive activity seems to decrease compared to a general and persistent increase in SO_2 degassing. Unlike with Ambrym and Kilauea, the transition period does not show on the time series plots as occurring during the same time periods. The annual integration time series demonstrates it to occur during mid-2009, while in the seasonal integration time series, it occurs during late 2010 or early 2011 (Figure 10). Both spikes in VRE occur at the same time as high-activity dome growth episodes (GVP, 2010; GVP, 2011).

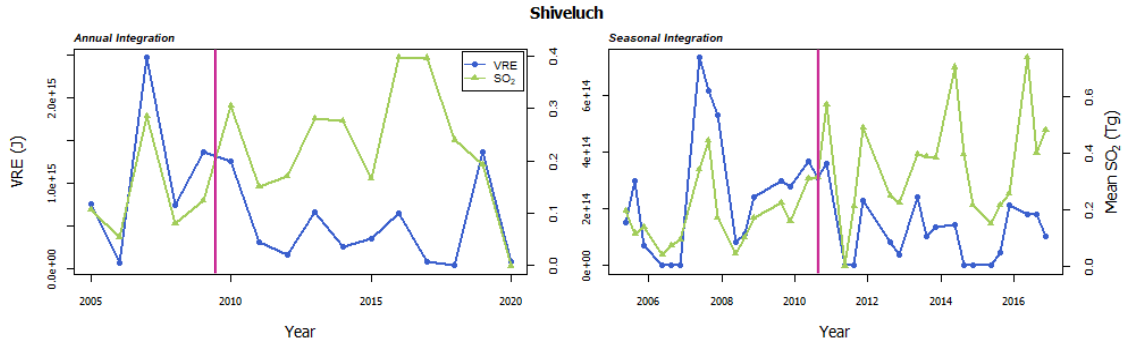

Figure 10. SO_2 flux (green) and VRE (blue) time series of Shiveluch drawn at annual intervals (left) and seasonal intervals (right). The pink lines mark the approximated time periods where the activity transitioned from primarily eruptive activity to primarily degassing activity.

The Ambrym, Kilauea and Shiveluch time series demonstrate instances where a change from primarily degassing activity to primarily lava-producing activity, or vice-versa, occurs over long periods of time. The seasonal time series plot for the Dukono volcano shows that this transition can also occur within shorter time spans followed by a return to the originally predominant form of activity (Figure 11). In this case, predominantly degassing activity "instantaneously" decreases at the same time as spikes in eruptive activity occur. Although this change of behavior occurs three times in both the annual and seasonal time series, the times at which they occur do not align. This is likely due to a lack of seasonal data during the increase in heat emitting activity.

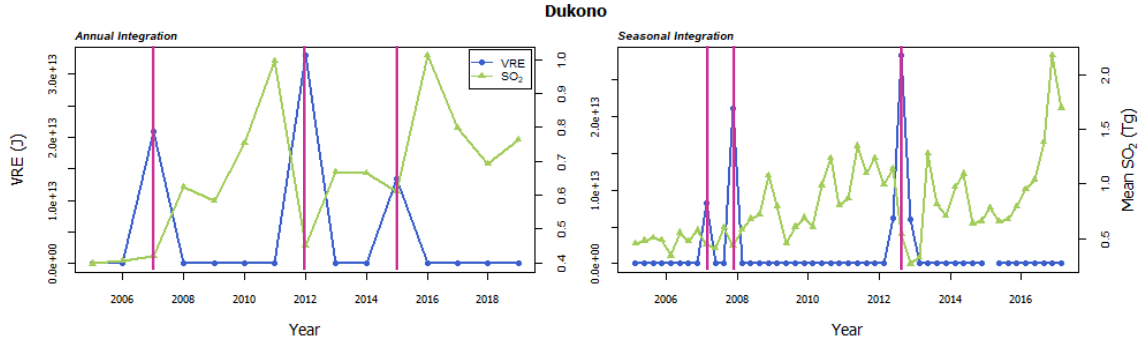

Figure 11. SO_2 flux (green) and VRE (blue) time series of Shiveluch drawn at annual intervals (left) and seasonal intervals (right). The pink lines mark the approximated time periods where the activity momentarily "switched" to increased eruptive activity.

4.3 Excess Sulfur Analysis

A representative measurement of the amount of degassed sulfur (in ppm) was extracted from the VRE-SO^2 relationship of 15 volcanoes through calculations involving their corresponding magma densities and c_{rad} values. This measurement was then compared to the amounts of sulfur measured from magma inclusions recorded in the literature (i.e., petrologically derived sulfur estimate), which is representative of the amount of sulfur dissolved in the magma. The results of this analysis are summarized in Table 2 and can be visualized in Figure 12.

Yasur, Popocatepetl, Tungurahua, Barren Island, Merapi, Soufriere Hills and Nishinoshima consistently returned maximum degassed S values greater than the S mass in melt inclusions. All of them are associated with subduction zones, but demonstrate different compositions ranging from basaltic to dacitic, and a variety of activity types (mafic lava flows, mafic lava lakes, felsic domes/flows, and explosive) (GVP, 2013c).

Sinabung, Fuego, Santiaguito, Kliuchevskoy, Sangay, Piton de la Fournaise and Erebus returned the inverse. For these cases, S values from melt inclusions in these volcanoes surpassed the degassed S estimates. However, the difference between these two values was relatively narrow in Piton de la Fournaise and Erebus compared to the others, which demonstrate a very wide offset. These two last volcanoes are also the only ones in this group that result from hotspot volcanism; the rest are associated with subduction zone volcanism (GVP, 2013c). Overall, there is a wide variety in terms of type of activity (mafic lava flows, mafic lava lakes, felsic domes/flows, and explosive) and compositions range from basaltic to andesitic (GVP, 2013c).

The excess S analysis for Mayon and Erta Ale returned inclusion derived values below the maximum degassed sulfur estimate but above the minimum degassed sulfur estimate. Erta Ale is associate with rift volcanism, is basaltic in nature and has a mafic lava lake; Mayon is associated with subduction zone volcanism, produces basaltic andesite lavas, and generates activity consisting of lava flows (GVP, 2013c).

Table 2. Excess S analysis results. The volcanoes were divided using the IUGS classification of volcanic rocks into basic (45-52 wt.% SiO_2), intermediate (52-63 wt.%) and acidic (> 63%) based on the mode of their reported erupted products from eruptions within the las 100 years. Tectonic setting was identified as hot spot (HS), rift (R), or subduction zone (S). The magma density (ρ) range is the minimum and maximum magma density given its SiO_2 content.

* Data for calculating the SiO_2 wt% mode were downloaded from the GEOROC database (https://georoc.eu/) on May and June 2022, using the following parameters: Geography = (Volcano Name) and material type = whole rock.

Volcano	**Tectonic Environment**	**Activity Type**	**m (J/Tg)**	**c_{rad} (± 50%) (J/m^3)**	**ρ Range (kg/m^3)**	**Degassed S Range (ppm)**	**Inclusion Derived S (ppm)**	**Sources**
Basalts								
Piton d. l. Fournaise	HS	mlf	3.15E-17	1.8E+08	2700-3300	867-1060	1415	Wright et al. (2015), Di Muro et al. (2014) *
Erta Ale	R	mll	4.35E-17	1.7E+08	2700-3300	1147-1402	1218	Field et al. (2012), de Moor et al. (2013) *
Barren Island	S	mlf	1.69E-16	1.2E+08	2700-3300	2938-3591	1026	Chandrasekharam et al. (2009), Luhr and Haldar (2006) *
Basaltic Andesites								
Kliuchevskoy	S	mlf	4.77E-17	6.8E+07	2400-2800	534-639	3515	Bergal-Kuvikas et al., (2017) *

Fuego	S	mlf	7.88E-17	6.2E+07	2400-2800	741-905	2250	Wright et al. (2015), Lloyd et al. (2014) *
Merapi	S	fdf	1.94E-16	4.7E+07	2400-2800	1484-1775	535	Wright et al. (2015), Preece et al. (2014)
Mayon	S	mlf	4.15E-16	4.7E+07	2400-2800	3174-3797	3300	Wright et al. (2015), Maximo and Walker (2010)
Erebus	HS	mll	2.74E-17	3.9E+07	2400-2800	190-221	375	Le Losq et al. (2015), Oppenheimer et al. (2011)
Andesites								
Sangay	S	fdf	2.46E-17	3.5E+07	2400-2800	143-171	5473	Monzier et al. (1999), Narvaez et al. (2018)
Yasur	S	ex	1.29E-15	3.2E+07	2400-2800	7424-1000	1000	Firth et al. (2021), Metrich et al. (2011)
Tungurahua	S	ex	7.38E-16	2.5E+07	2400-2800	3255-1800	1800	Myers et al. (2014), Myers et al. (2014)

Nishinoshima	S	mlf	5.66E-17	2.1E+07	2400-2800	210-245	19	Tamura et al. (2018), Ueda and Sakai (1984)
Santiaguito	S	fdf	1.91E-16	2.1E+07	2400-2800	720-834	1656	Pyle and Stock (2015)
Soufreire Hills	S	fdf	4.07E-16	2.1E+07	2400-2800	1507-1758	149	Wright et al. (2015), Edmonds et al. (2001)
Sinabung	S	ex	1.52E-15	1.8E+07	2400-2800	4740-5530	8500	Nakada et al. (2019), Sinuhaji et al. (2018) *
Dacites								
Popocatepetl	S	fdf	1.99E-15	1.3E+07	2350-2700	4073-4872	1980	Witter et al. (2005), Witter et al. (2005) *

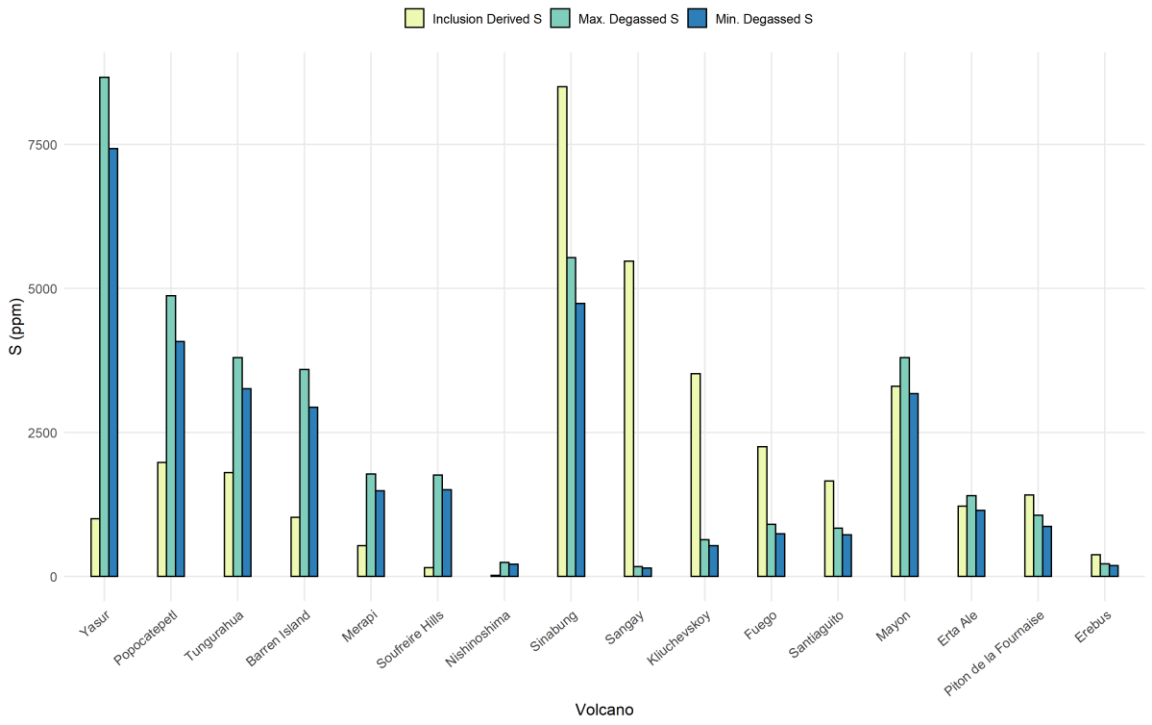

Figure 12. Bar plot depicting the estimated maximum and minimum fractions of degassed sulfur (S; in ppm) and the amount of S present in melt inclusions from each corresponding volcano. The S measurements from the inclusions are sourced from the literature and their references are included in Table 2.

4.4 SO_2 Flux Extrapolation Analysis

By extrapolating the annual or seasonal SO_2 flux emission from eight of the volcanoes, we aimed to explore the usefulness of the VRE-SO_2 relationship for volcanic monitoring purposes and to gain insight into the sulfur dioxide emission patterns of these volcanoes prior to the launch of the OMI satellite. The resulting lower and upper confidence limits of the data used are shown in Table 3. Table 3 also shows whether the annual or seasonal data was used and reiterates the correlation coefficient, regression standard error and p-value associated with each regression. All p-values proved to be below the significance level ($\alpha = 0.05$).

Time series plots depicting the 2000-2005 predicted SO_2 values and VRE signals for annual and seasonal data are shown on the left columns of Figures 14 and 15, respectively. The write columns show each volcano's corresponding simple linear regression plot, which contains the points used for the regression (data from 2005-2019), a fitted line, and 95% confidence and prediction intervals.

Table 3. Shows the confidence intervals at a statistical significance of $\alpha = 0.05$ and the integration interval used to extrapolate 2000-2005 data.

Volcano	**Integration Interval**	**R^2**	**SSR**	**P-Value**	**95% CI [LL, UL]**
Bagana	annual	0.72	0.24	0.000	[0.327, 0.842]
Barren Island	seasonal	0.6	0.127	0.000	[-0.004, 0.112]
Erta Ale	annual	0.89	0.049	0.000	[-0.018, 0.04]
Kliuchevskoy	annual	0.44	0.17	0.005	[0.015, 0.252]
Piton de la Fournaise	seasonal	0.68	0.073	0.000	[0.001, 0.062]
Popocatepetl	annual	0.86	0.124	0.000	[-0.059, 0.175]
Santiaguito	annual	0.55	0.023	0.002	[0.045, 0.079]
Yasur	annual	0.49	0.186	0.002	[0.008, 0.513]

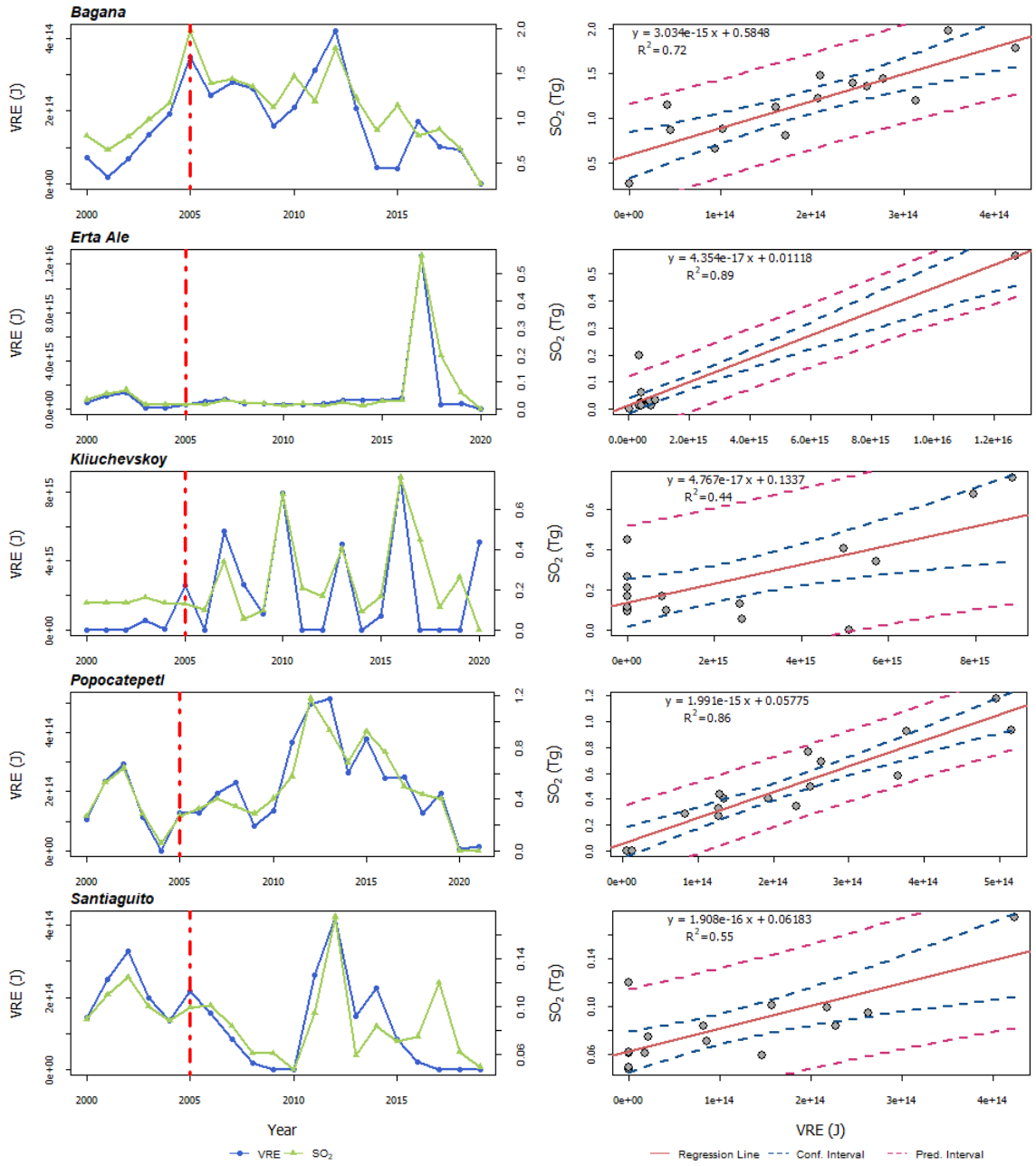

Figure 13. The left column shows the VRE (blue) and SO_2 (green) time series plots of the volcanoes whose annual data was used for predicting the SO_2 flux values. The dotted red line marks the division between predicted values (prior to 2005) and satellite measured values. The right column shows the volcano's respective VRE-SO_2 regression points in grey; the solid red lines, blue dashed lines and green dashed lines represent their regression lines, confidence intervals and prediction intervals, respectively. The regression plots also include the regression equation and correlation coefficient (R^2) value.

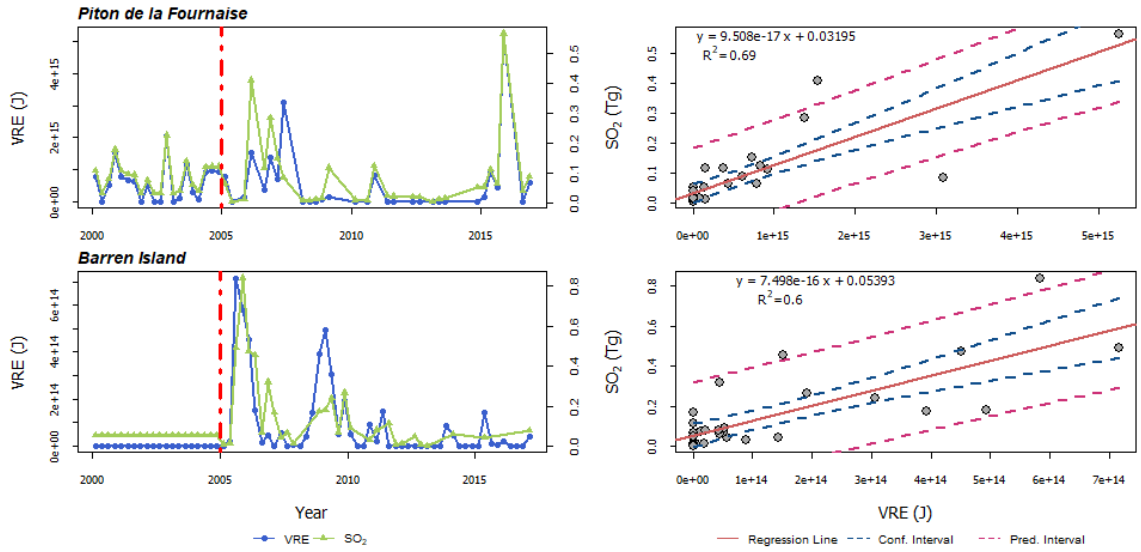

Figure 14. The left column shows the VRE (blue) and SO_2 (green) time series plots of the volcanoes whose seasonal data was used for predicting the SO_2 flux values. The dotted red line marks the division between predicted values (prior to 2005) and satellite measured values. The right column shows the volcano's respective VRE-SO_2 regression points in grey; the solid red lines, blue dashed lines and green dashed lines represent their regression lines, confidence intervals and prediction intervals, respectively. The regression plots also include the simple linear regression equation and correlation coefficient (R^2) value.

5 Discussion

5.1 Activity patterns

The relationship between satellite measured, volcanic sulfur dioxide emissions and volcanic heat emissions help to obtain insight into changes in volcanic activity. In the previous section, we highlight some of the most outstanding patterns identified by qualitatively analyzing the volcanic data's annual and seasonal time series plots. We then used them to gain insight into the extent and nature of each volcano's VRE-SO_2 relationship and how it varies depending on the type of activity.

Kizimen, Sinabung, Sabancaya, Sangeang Api and Piton de la Fournaise initially stood out due to demonstrating VRE-SO_2 correlations equal to or higher than 60% when using both annually and seasonally integrated data. The degree of the correlation is also similar in both time frames for each volcano (see Table 1). This suggests that, within the study period, the average amount of sulfur dioxide degassed in a trimester "equaled" the amount of heat emitted by superficial lava within the same interval. For example, the Kizimen 2012 eruption, recorded both in the GVP bulletin reports (GVP, 2013d) and in the time series constructed in this investigation (Figure 4a), is a clear example of an event in which SO2 degassing and lava extrusion (heat emission) occur "spontaneously" and at similar rates during a geologically short time period (~ 5 years). Sinabung, Sabancaya and Sangeang Api (Figures 4b-d) also show such individual peaks in activity that can be associated to relatively isolated events in geologic history, even if their eruptive periods were or have been slightly longer than that of Kizimen. Due to SO_2 flux and VRE being numerically close to zero at most other times before and after, their corresponding regression lines are controlled by these "bursts" of activity and their regression analyses result in high correlation coefficients.

Piton de la Fournaise is like the aforementioned volcanoes in the sense that its data also returned a high correlation coefficient between the SO_2 flux and VRE. However, Piton has a more mafic composition and is known for producing lava flows (Michon et al., 2013) and the correlation coefficient of the regression seems to depend on several peaks in activity and not on a single event (Fig. 4e). Also, unlike Kizimen, Sabancaya, Sinabung and Sangeang Api, these peaks in activity do not always "line up" at maximum activity, which can be seen as degassing begins before Piton's eruption in 2007 and is followed by a period of heat emissions with little SO_2 flux. Later in 2015-2016, another eruptive event occurs in which degassing, and heat emissions do occur at similar rates. In any of these cases, the SO_2 degassing is proportional to peaks in heat emissions, which might explain why the correlation is still high despite some of the differences in timing. Lower silica concentrations also make it easier for a gaseous phase to escape simultaneously, or close to simultaneously, when lava is extruded as a flow (Carn, 2016).

Moreover, the time series plots for Soufriere Hills and Galeras suggest that SO_2 degassing gradually increased prior to an eruption and reached its maximum at roughly the same time as its maximum lava-producing activity. It then decreased proportionally to decreasing heat emissions, although much more gradually. For these two volcanoes, it can be interpreted that degassing was caused by an influx of magma at depth and that it generated the magmatic overpressure required to produce eruptions or eruptive periods

with strong heat emissions (Wadge, 2014). These occurred as a dome collapse in 2006 for Soufriere Hills and as a series of vulcanian eruptions in 2009 and 2010 for Galeras.

For the remaining three volcanoes (Cleveland, Sangay, and Shiveluch), the correlation coefficients were below 0.20 for both the annual and seasonal data and the time series showed a predominance of degassing activity over lava extrusion. The Shiveluch time series will be discussed later as a comparison to the time series of two mafic volcanoes that show some similarities. Furthermore, it is possible that the relationship between SO_2 and VRE is ultimately linear for all volcanoes if evaluated over a long enough time frame (specific of each volcanic system). Given that we only have access to degassing during a short time period (15-20 years), it might be difficult to prove this for volcanoes that take decades or centuries to produce lava extruding eruptions.

The annual and seasonal time series for Ambrym and Kilauea, both of which are characterized by lava lake activity, show that predominant degassing activity is succeeded by a long-term increase in effusive activity. Research suggests that long-lasting, lava lake volcanoes go through stages of "endogenous growth" (Francis, 1993). For these types of mafic systems, magma must be close to the surface to produce copious amounts of degassing such as those emitted by Kilauea (Francis, 1993), for example, between the 2008 onset of activity at Halemaumau crater and growing effusive activity from Pu'u O'o, Halemaumau and the East Rift Zone beginning around 2011. However, superficial heat emissions data can be contradictory of this as heat signals are often comparatively scarce during these periods (GVP, 2010) (Figure 9b). The term endogenous growth (opposite to exogenous growth) is used to explain how a volcano is capable of "growing" despite constant heat loss. In other words, influxes of magma capable of driving large amounts of degassing and heat loss producing convection are continuously occurring without signs of the volcano cooling itself out and despite a reduction in heat signals (Coppola et al., 2019). Francis et al. (1993) describes that endogenous growth occurs in mafic volcanoes with complex dyke and lava tube systems that impede the lava from surfacing or can cause it to be erupted on the seafloor. It can also occur when cumulates of solidifying magma are built up in the lower crust under the volcanoes, or when cooling and subsequent crystallization helps drive convection in the overlying reservoir (Coppola et al., 2019). For example, GVP bulletin reports suggest that endogenous growth in Kilauea between 2008~2011 is a result of the first mechanism (GVP, 2007; GVP, 2009; GVP, 2010; GVP, 2013e). While an increase in SO_2 emissions was triggered by intrusion of magma to a shallow chamber in the Mauna Ulu area in 2008, the movement of magma towards the regions whose activity would later characterize a peak in heat emissions in 2016 (Pu'u Oo, Halemaumau and the East rift Zone) was taking place in the sub surface and could not, in its majority, be detected by the MODIS satellites (GVP, 2009; GVP, 2016a; GVP, 2016b). Additionally, major degassing events can develop thick cloud coverage that limits the acquisition of heat signal data to a certain extent.

The seasonal time series for Shiveluch suggests a transition opposite to that of Ambrym and Kilauea: a predominance in heat emitting activity changes to predominantly degassing activity sometime during 2011. Even though the terms exogenous and endogenous growth are commonly used to describe sinks in lava-producing activity in mafic volcanic systems, it can be argued that they could be applied to activity in more felsic systems, such as Shiveluch. When studied closely, the peaks in VRE signals in Shiveluch's

data during the 2000's coincide with eruptions and activity related to dome growth (pyroclastic flows). Until the October 2010 eruption, heat emissions predominated SO_2 degassing. However, after an overall sink in activity succeeding the eruption, there was visual evidence that explosive-effusive-extrusive activity continued. In addition, the bulletin reports from the GVP do not provide distinct evidence that SO_2 flux should have been overwhelming heat emissions, especially given the amount of lava and pyroclastic flow activity that was still occurring at the time. The GVP (2013f), however, mentions that cloud coverage over the volcano can interrupt accurate heat emissions data for months at a time, which could explain the overall lower VRE signals. More data on possible changes suffered by the volcanic system after the 2010 eruption are needed to conclude whether lack of data due to cloud coverage is the cause of this dilemma.

A closer look at Bagana's seasonal time series shows almost perfect VRE-SO_2 correlation until late 2013, when SO_2 emissions start to dominate after a simultaneous increase in heat emissions and decrease in degassing. This "alternating" pattern where a decrease in one parameter is simultaneous with an increase in the opposite parameter keeps occurring seasonally after 2014. This correlates to McCormick et al's. (2019) description of Bagana's recent activity, which consists of continuous lava flows from 2000 through 2014. In 2014, the volcano started persistently producing ash plumes and sparse thermal anomalies, suggesting a change in the overall eruptive activity (GVP, 2014). However, most of the information regarding activity for this time period is only available through satellite monitoring due to the volcano's remoteness and inaccessibility. In addition, although the GVP reports evidence of heat emitting lava extrusion at the summit, the constant ash plume coverage impedes more detailed descriptions on whether lava flow activity has effectively transitioned to dome building activity (GVP, 2019). Even though it is difficult to describe the exact circumstances, the overall dominance of SO_2 emissions for several years after 2014 and a cease in its distinctive effusive activity suggests that this volcano underwent a period of endogenic growth.

5.2 Excess Sulfur and the VRE-SO_2 relationship

The "excess" S problem is a term used to refer to the much larger mass of sulfur degassed during eruptions compared to what would be expected based on the sulfur concentrations in melt inclusions (Shinohara et al., 2008). "Excess" sulfur can be degassed during a variety of eruption types, from persistent degassing to Plinian activity, and is a common occurrence independently of magma composition. However, eruptive activity and magma composition, along with tectonic setting, do influence the degree at which it excess degassing occurs (Shinohara, 2008).

In this investigation, we chose 15 volcanoes showing good VRE-SO_2 correlations ($R^2 > 0.50$) with available, inclusion-derived sulfur concentration data to better understand their degassing patterns. We then calculated an estimate of their maximum and minimum mass fractions of degassed sulfur using Coppola et al.'s (2013) radiant density and each volcano's silica content, magma density and VRE-SO_2 regression line slope. We then converted these masses to ppm and compared them to sulfur concentrations in melt inclusions recorded in the literature.

The results of this analysis prompted us to divide the volcanoes into four groups: those which returned degassed S estimates higher than inclusion derived S values, those

whose inclusion derived S values surpassed the degassed S estimates by a wide margin, those whose inclusion derived S values surpassed the degassed S estimates by a close margin, and those who showed inclusion values in between the maximum and minimum degassed S estimates.

Yasur, Popocatepetl, Tungurahua, Barren Island, Merapi, Soufriere Hills and Nishinoshima consistently returned maximum degassed S estimates greater than the S mass in melt inclusions. All are associated with subduction zone volcanism and have compositions ranging from basalts to dacites. There is not a clear suggestion of similarities between them in terms of primary type of activity given that two of them produce explosive activity, three produce felsic domes or flows, and three produce mafic lava flows.

The excess S analysis for Sinabung, Fuego, Santiaguito, Kliuchevskoy and Sangay shows inclusion derived S values that are 50-97% greater than the maximum degassed S estimate. All of these formed through subduction zone volcanism, have basaltic-andesitic or andesitic compositions, and show either explosive, mafic lava flow forming or felsic lava dome/flow forming activity. Sinabung, Piton de la Fournaise and Erebus also exhibit the same pattern, although the degassed S estimates are below the inclusion derived values by 35%, 25% and 41%, respectively.

Erta Ale and Mayon are basaltic and basaltic-andesite volcanoes that show inclusion derived sulfur values in between the maximum and minimum degassed S estimates. Erta Ale is associated with rift volcanism and has a lava lake, while Mayon commonly exhibits mafic flow activity and is associated with a subduction zone.

Shinohara (2008) concludes that the mechanisms that drive excess degassing, as well as how they relate to factors such as activity style, composition, and tectonic setting, are still a subject of debate. The excess S analysis done here agrees with these expressions given the lack of clear connections between the three aforementioned factors. A more in-depth study is needed to constrain the degree at which each of these factors influence the "excess" S quantities degassed by the volcanoes, or if this relationship grows stronger given more specific combinations of factors in each case.

5.3 The VRE-SO_2 relationship and Latitude

OMI and MODIS sensors have been known to have limitations concerning their ability to obtain accurate SO2 flux and heat emission measurements during unfavorable weather (Carn et al., 2013; GVP, 2019). Because of this, we hypothesized that the degree of the VRE-SO_2 relationship would be strongly influenced by latitude location. We expected volcanos at higher latitudes to show weaker VRE-SO_2 relationships due to the long-term cloud coverage present in winter months. A visualization of this analysis is presented in Figure 5. We plotted correlation coefficients of annual and seasonal regression analyses against the latitude of each volcano and found that there is no clear link between a volcano's location and its VRE-SO_2 relationship. This is partly because long term cloud coverage is not necessarily limited to higher latitudes. Many tropical locations experience months-long rainy seasons. The altitude of some volcanic edifices also promotes the generation of microclimates independent of the surrounding regional climate that can cause measurement uncertainties independent of latitude.

The vertical spread on both annual and seasonal time series plots suggests that the VRE-SO_2 relationship is more likely dependent on a combination of activity type and

timeframe over which the data is averaged. The timeframe component can be readily appreciated as the correlation coefficients of many of the volcanoes drop significantly when the integration period is reduced to three months rather than a year. The persistence of some of the explosive (strombolian) and mafic-lava-flow type volcanoes above the R = 0.50 mark suggest that main activity type and magma composition are another determining factor.

5.4 2000-2005 SO_2 flux Extrapolation

Scientist began using satellites to measure volcanic degassing in 1982 after the Total Ozone Mapping Spectrometer (TOMS) registered SO_2 emissions from a large eruption of El Chichón in Mexico (Carn et al., 2016). At this point, TOMS had been in orbit for approximately four years. Given that there it was not initially intended to be a volcanic monitoring tool, it's capacity for registering anything else than SO_2 output from the largest eruptions and copious passive degassing was limited (Carn et al, 2016). However, some data is better than no data at all, and, from its launch in 1978 and four TOMS missions later, it provided "near-continuous multi-spectral, global, nadir UV observations at low spatial resolution" until 2005, albeit with several small data gaps and a large, 19-month gap (Carn et al., 2016). The Solar Backscatter Ultraviolet Instrument (SBUV) and the High-resolution Infrared Radiation Sounder (HIRS), also launched in 1978 and with their own limitations in volcanic monitoring, helped fill in those data gaps (Carn et al., 2016). Later on, newer satellites, such as the Global Ozone Monitoring Instrument (GOME; 1995), were launched with optimized spectral resolutions that permitted an increased sensitivity to SO_2 at tropospheric levels (Carn et al., 2016). Nevertheless, an inventory of the data these mid-late 1990's satellites gathered has not been widely reported. Between a limited TOMS and a poorly kept, post-1995 SO_2 emissions record, there is some of a blur in satellite sensed volcanic SO_2 data prior to the launch of OMI in mid-2004.

In this investigation, we used the assumption of linearity between SO_2 flux and VRE measurements to extrapolate SO_2 emission measurements based on volcanic heat emissions data obtained from the Terra MODIS (launched in 1999). For this analysis, we chose six volcanoes with correlation coefficients $R^2 > 0.50$ and one with $R^2 = 0.44$ (Table 3).

An assessment of the VRE-SO_2 regressions' P-values and correlation coefficients strongly suggests that all the regressions are statistically significant. In other words, for the volcanoes in Figures 14 and 15, there is statistical relationship between how much heat emitting activity a volcano produces and how much SO_2 is degassed. However, whether VRE can be used by itself to predict or 'hind-cast' these volcanoes' SO_2 emissions still merits deeper consideration.

6 Conclusion

Through this investigation we were able to use the relationship between Volcanic Radiative Energy and SO_2 degassing to gain new insight into the eruptive processes and activity patterns of over 50 volcanoes located at varying latitudes. Even though the statistical correlations between VRE and SO_2 emissions were relatively weak at many of the volcanoes, this study demonstrates the value of analyzing time series of both parameters because they provide insight into volcanic processes such as endogenous and exogenous growth, and transitions between them. For this investigation they revealed that, specifically for volcanoes with felsic/dome flow activity, strong linear relationships between VRE and SO_2 flux on annual timescales can break down when integrating the data over shorter, seasonal time periods. One possible interpretation of this is a decoupling between SO_2 emissions and heat flux on shorter timescales, where volatiles (such as SO_2) degassed from fresh magma at depth are transferred to the surface more rapidly than the associated heat flux.

The excess sulfur content analysis conducted for volcanoes whose VRE-SO_2 relationship was stronger produced variable results. There were no clear patterns in terms of whether excess sulfur tended to be stronger based on specific combinations of tectonic setting, composition, and activity type. More information and further study are needed to better understand how these factors relate to excess S degassing. Nevertheless, for some volcanoes, measured SO_2 emissions show a reasonable agreement with emissions predicted from melt inclusion sulfur contents, given the significant uncertainties inherent to this analysis. At other volcanoes (e.g., Yasur, Vanuatu), this analysis confirms the large excess sulfur degassing expected at such persistently active volcanic systems.

Some of the volcanoes returned very strong VRE-SO_2 relationships and were subjected to extrapolation of SO_2 values for 2000-2005 based solely on VRE measurements for that time. The lack of SO_2 degassing data for that period impeded having something to compare our estimates with. In addition, some volcanoes, such as Santiaguito and Bagana, demonstrated a break in the initial activity pattern and underwent persistent degassing stages. Given that we only tested the data with simple linear regressions, such a deviation from the "norm" prior to 2005 could easily exist and increase the error of our estimates.

Overall, this study demonstrates the potential value of monitoring both SO_2 emissions and VRE concurrently to improve our understanding of global volcanic activity and detect key transitions in volcano behavior. Although this analysis was based on OMI SO_2 and MODIS VRE data, future analyses could achieve better sensitivity by incorporating new SO_2 data from the Tropospheric Monitoring Instrument (TROPOMI) aboard the Sentinel-5 Precursor satellite, and heat flux data from the Visible Infrared Imaging Radiometer Suite (VIIRS) aboard the Suomi-NPP and NOAA-20 satellites, which have higher spatial resolution than OMI and MODIS, respectively.

7 Works Cited

Bergal-Kuvikas, O., Nakagawa, M., Kuritani, T., Muravyev, Y., Malik, N., Klimenko, E., Amma-Miyasaka, M., Matsumoto, A. and Shimada, S., 2017, A petrological and geochemical study on time-series samples from Klyuchevskoy volcano, Kamchatka arc: Contributions to Mineralogy and Petrology, v. 172, np. 5, p. 35.

Carn, S. A., Krotkov, N. A., Yang, K., Krueger, A. J., Pyle, D. M., Mather, T. A., and Biggs, J., 2013, Measuring global volcanic degassing with the Ozone Monitoring Instrument (OMI), Remote Sensing of Volcanoes and Volcanic Processes: Integrating Observation and Modelling, v. 380, Geological Society of London, p. 0.

Carn, S. A., 2016, On the detection and monitoring of effusive eruptions using satellite SO_2 measurements: Geological Society of London Special Publications v. 426, pp. 277.

Carn, S. A., Clarisse, L., Prata, A. J., 2016, Multi-decadal satellite measurements of global volcanic degassing: Journal of Volcanology and Geothermal Research, v. 311, p. 35.

Carn, S. A., Fioletov, V., McLinden, C., Li, C. and Krotkov, N., 2017, A decade of global volcanic SO2 emissions measured from space: Scientific Reports, v. 7, pp. 44095.

Chandrasekharam, D., et al. (2009). "Volcanological and petrological evolution of Barren Island (Andaman Sea, Indian Ocean)." Journal of Asian Earth Sciences 35(5): 469-487.

Coppola, D., Laiolo, M., Piscopo, D. and Cigolini, C., 2013, Rheological control on the radiant density of active lava flows and domes: Journal of Volcanology and Geothermal Research, v. 249, p. 39-48.

Coppola, D., Laiolo, M., Massimetti, S. and Cigolini, C., 2019, Monitoring endogenous growth of open-vent volcanoes by balancing thermal and SO2 emissions data derived from space: Scientific Reports, v. 9, pp. 9394.

de Moor, J. M., Fischer, T. P., Sharp, Z. D., King, P. L., Wilke, M., Botcharnikov, R. E., Cottrell, E., Zelenski, M., Marty, B., Klimm, K., Rivard, C., Ayalew, D., Ramirez, C. and Kelley, K. A., 2013, Sulfur degassing at Erta Ale (Ethiopia) and Masaya (Nicaragua) volcanoes: Implications for degassing processes and oxygen fugacities of basaltic systems: Geochemistry, Geophysics, Geosystems, v. 14, no. 10, p. 4076-4108.

Di Muro, A., Métrich, N., Vergani, D., Rosi, M., Armienti, P., Fougeroux, T., Deloule, E., Arienzo, I., Civetta, L., 2014, The Shallow Plumbing System of Piton de la Fournaise Volcano (La Réunion Island, Indian Ocean) Revealed by the Major 2007 Caldera-Forming Eruption: Journal of Petrology, v. 55, no. 7, p. 1287-1315.

Edmonds, M., Pyle, D. and Oppenheimer, C., 2001, A model for degassing at the Soufrière Hills Volcano, Montserrat, West Indies, based on geochemical data: Earth and Planetary Science Letters, v. 186, p. 159–173.

Edmonds, M., Oppenheimer, C. M., Pyle, D. M., Herd, R. A., Thompson, G., 2003, SO2 emissions from Soufrière Hills Volcano and their relationship to conduit permeability, hydrothermal interaction, and degassing regime: Journal of Volcanology and Geothermal Research, vol. 124, p. 23-43.

Farooq, S., 2021, Rock Density: www.geol-amu.org/notes/m10-1-1b.htm (Accessed December 2021).

Field, L., Barnie, T., Blundy, J., Brooker, R. A., Keir, D., Lewi, E., Saunders, K., 2012, Integrated field, satellite, and petrological observations of the November 2010 eruption of Erta Ale: Bulletin of Volcanology, v. 74, n. 10, p. 2251-2271.

Fioletov, V. E., McLinden, C. A., Krotkov, N. A., Li, C., Joiner, J., Theys, N., Carn, S. A. and Moran, M. D., 2016, A global catalogue of large SO2 sources and emissions derived from the Ozone Monitoring Instrument: Atmospheric Chemistry and Physics, v. 16, p. 11497-11519.

Firth, C. W., Turner S. P., Handley H. K., Turner M. B., Cronin S. J., Girard G., Smith I. E. M., 2021, Rapid magmatic processes drive persistently active volcanism: Lithos v. 380-381, p. 14. https://doi.org/10.1016/j.lithos.2020.105868

Flower, V. J. B., and S. A. Carn, 2015, Characterising volcanic cycles at Soufriere Hills Volcano, Montserrat: Time series analysis of multi-parameter satellite data: Journal of Volcanology and Geothermal Research, v. 304, p. 82-93.

Francis, P. W., Oppenheimer, C., Stevenson, D. L., 1993, Endogenous growth of persistently active volcanoes: Nature, v. 366, p. 554-557. Global Volcanism Program, 2013a, Report on Ambrym (Vanuatu): In: Wunderman (ed.), Bulletin of the Global Volcanism Network, 38:5. Smithsonian Institution, https://doi.org/10.5479/si.GVP.BGVN201305-257040

Global Volcanism Program, 2013b, Report on Kilauea (United States): In: Wunderman (ed.), Bulletin of the Global Volcanism Network, 38:5. Smithsonian Institution, https://doi.org/10.5479/si.GVP.BGVN201305-332010

Global Volcanism Program, 2013c, Volcanoes of the World, v. 4.11.0 (08 Jun 2022). Venzke, E (ed.). Smithsonian Institution. Downloaded 24 Jun 2022. https://doi.org/10.5479/si.GVP.VOTW4-2013.

Global Volcanism Program, 2013d, Report on Kizimen (Russia) (Herrick, J.A., and Wunderman, R., eds.). Bulletin of the Global Volcanism Network, 38:4. Smithsonian Institution. https://doi.org/10.5479/si.GVP.BGVN201304-300230

Global Volcanism Program, 2013e, Report on Kilauea (United States) (Wunderman, R., ed.). Bulletin of the Global Volcanism Network, 38:2. Smithsonian Institution. https://doi.org/10.5479/si.GVP.BGVN201302-332010

Global Volcanism Program, 2007, Report on Kilauea (United States) (Wunderman, R., ed.). Bulletin of the Global Volcanism Network, 32:6. Smithsonian Institution. https://doi.org/10.5479/si.GVP.BGVN200706-332010

Global Volcanism Program, 2009, Report on Kilauea (United States) (Wunderman, R., ed.). Bulletin of the Global Volcanism Network, 34:3. Smithsonian Institution. https://doi.org/10.5479/si.GVP.BGVN200903-332010

Global Volcanism Program, 2010, Report on Kilauea (United States) (Wunderman, R., ed.). Bulletin of the Global Volcanism Network, 35:1. Smithsonian Institution. https://doi.org/10.5479/si.GVP.BGVN201001-332010

Global Volcanism Program, 2013e, Report on Kilauea (United States) (Wunderman, R., ed.). Bulletin of the Global Volcanism Network, 38:2. Smithsonian Institution. https://doi.org/10.5479/si.GVP.BGVN201302-332010

Global Volcanism Program, 2016a, Report on Kilauea (United States) (Crafford, A.E., and Venzke, E., eds.). Bulletin of the Global Volcanism Network, 41:2. Smithsonian Institution. https://doi.org/10.5479/si.GVP.BGVN201602-332010

Global Volcanism Program, 2016b, Report on Kilauea (United States) (Crafford, A.E., and Venzke, E., eds.). Bulletin of the Global Volcanism Network, 41:8. Smithsonian Institution. https://doi.org/10.5479/si.GVP.BGVN201608-332010

Global Volcanism Program, 2013f, Sheveluch (300270) in Volcanoes of the World, v. 4.11.0 (08 Jun 2022). Venzke, E (ed.). Smithsonian Institution. Downloaded 24 Jun 2022 (https://volcano.si.edu/volcano.cfm?vn=300270). https://doi.org/10.5479/si.GVP.VOTW4-2013

Global Volcanism Program, 2014, Report on Bagana (Papua New Guinea) (Wunderman, R., ed.). Bulletin of the Global Volcanism Network, 39:12. Smithsonian Institution. https://doi.org/10.5479/si.GVP.BGVN201412-255020

Global Volcanism Program, 2019, Report on Bagana (Papua New Guinea) (Bennis, K.L., and Venzke, E., eds.). Bulletin of the Global Volcanism Network, 44:12. Smithsonian Institution. https://doi.org/10.5479/si.GVP.BGVN201912-255020

Global Volcanism Program, 2010, Report on Sheveluch (Russia): In: Wunderman (ed.), Bulletin of the Global Volcanism Network, 33:3. Smithsonian Institution, https://doi.org/10.5479/si.GVP.BGVN201003-300270

Global Volcanism Program, 2011. Report on Sheveluch (Russia): In: Wunderman (ed.), Bulletin of the Global Volcanism Network, 36:4. Smithsonian Institution, https://doi.org/10.5479/si.GVP.BGVN201104-300270

Harris, A. J. L., Favalli, M., Steffke, A., Fornaciai, A., Boschi, E., 2010, A relation between lava discharge rate, thermal insulation, and flow area set using lidar data. Geophysical Research Letters, v. 37, doi: 10.1029/2010GL044683.

Koeppen, W. C., Patrick, M., Orr, T., Sutton, A. J., Dow, D. & Wright, R., 2013, Constraints on the partitioning of Kı¯lauea's lavas between surface and tube flows, estimated from infrared satellite data, sulfur dioxide emission rates, and field observations: Bulletin of Volcanology, v. 75, pp. 716, http://doi.org/10.1007/s00445-013-0716-3.

Le Losq, C., Neuville, D., Moretti, R., Kyle, P. and Oppenheimer, C., 2015, Rheology of phonolitic magmas – the case of the Erebus lava lake: Earth and Planetary Science Letters, v. 411, p. 53-61.

Li, C., Joiner, J., Krotkov, N. A., and Bhartia, P. K., 2013, A fast and sensitive new satellite SO2 retrieval algorithm based on principal component analysis: Application to the ozone monitoring instrument: Geophysical Research Letters, v. 40, no. 23, p. 6314-6318.

Lloyd, A. S., Ruprecht, P., Hauri, E. H., Rose, W., Gonnermann, H. M., Plank, T., 2014, NanoSIMS results from olivine-hosted melt embayments: Magma ascent rate during explosive basaltic eruptions: Journal of Volcanology and Geothermal Research, v. 283, p. 1-18.

Luhr, J. F. and D. K. Haldar, 2006, Barren island volcano (NE Indian Ocean) : Island-arc high-alumina basalts produced by troctolite contamination: Journal of Volcanology and Geothermal Research, v. 149, p. 177-212.

Maximo, R. R. and J. A. Walker, 2010, Composition and volatile contents of melt inclusions from Mayon Volcano, Philippines, 2010: V53C-2266, https://ui.adsabs.harvard.edu/abs/2010AGUFM.V53C2266M

McCormick Kilbride, B. T., Mulina, K., Wadge, G., Johnson, R. W., Itikarai, I., Edmonds, M., 2019, Multi-year Satellite Observations of Sulfur Dioxide Gas Emissions and Lava Extrusion at Bagana Volcano, Papua New Guinea: Frontiers in Earth Science, v. 7.

Métrich, N., Allard, P., Aiuppa, A., Bani, P., Bertagnini, A., Shinohara, H., Parello, F., Di Muro, A., Garaebiti, E., Belhadj, O. and Massare, D., 2011, Magma and Volatile Supply to Post-collapse Volcanism and Block Resurgence in Siwi Caldera (Tanna Island, Vanuatu Arc): Journal of Petrology, v. 52, no. 6, p. 1077-1105.

Michon, L., Di Muro, A., Villeneuve, N., Saint-Marc, C., Fadda, P., Manta, F., 2013, Explosive activity of the summit cone of Piton de la Fournaise volcano (La Réunion island): A historical and geological review: Journal of Volcanology and Geothermal Research, v. 264, p. 117-133.

Monzier, M., Robin, C., Samaniego, P., Hall, M. L., Cotten, J., Mothes, P. and Arnaud, N., 1999, Sangay volcano, Ecuador: structural development, present activity and petrology, Journal of Volcanology and Geothermal Research, v. 90, no. 1, p. 49-79.

Myers, M. L., Geist, D. J., Rowe, M. C., Harpp, K. S., Wallace P. J. and Dufek, J., 2014, Replenishment of volatile-rich mafic magma into a degassed chamber drives mixing and eruption of Tungurahua volcano: Bulletin of Volcanology, v. 76, no. 11, p. 872.

Nakada, S., Z. A., Yoshimoto, M., Maeno, F., Suzuki, Y., Hokanishi, N., Sasaki, H., Iguchi, M., Ohkura, T., and Gunawan, H. and Triastuty, H., 2019, Growth process of the lava dome/flow complex at Sinabung Volcano during 2013–2016: Journal of Volcanology and Geothermal Research, v. 382, p. 120-136.

Narvaez, D. F., Rose-Koga, E. F., Samaniego, P., Koga, K. T. and Hidalgo, S., 2018, Constraining magma sources using primitive olivine-hosted melt inclusions from Puñalica and Sangay volcanoes (Ecuador): Contributions to Mineralogy and Petrology, v. 173, no. 10, p. 80.

OMI Team, 2009, Ozone Monitoring Instrument (OMI) Data User's Guide, Guidebook, p. 1-64.

Oppenheimer, C., Moretti R., Kyle, P. R., Eschenbacher, A., Lowenstern, J. B., Hervig, R.L., Dunbar, N. W., 2011, Mantle to surface degassing of alkalic magmas at Erebus volcano, Antarctica: Earth and Planetary Science Letters, v. 306, no. 3, p. 261-271.

Preece, K., Gertisser, R., Barclay, J., Berlo, K., Herd, R. A., and Edinburgh Ion Microprobe Facilit, 2014, Pre- and syn-eruptive degassing and crystallisation processes of the 2010 and 2006 eruptions of Merapi volcano, Indonesia: Contributions to Mineralogy and Petrology, v. 168, no. 4, p. 1061.

Scott, J. A. J., et al. (2015). "Insights into the behaviour of S, F, and Cl at Santiaguito Volcano, Guatemala, from apatite and glass." Lithos 232: 375-394

Rodríguez, N., 2019, Analysis of SO2 Emissions from the Santiaguito, Fuego, and Pacaya Volcanoes in Guatemala, Using Images from OMI [Undergraduate Research]: University of Puerto Rico, 40 p.

Shinohara, H., 2008, Excess degassing from volcanoes and its role on eruptive and intrusive activity: Reviews of Geophysics v. 46, no. 4.

Sinuhaji, P., et al. (2018). "Analysis of Composition; Topography of Volcanic Materials Erupted from Mount Sinabung, Karo Regency, Indonesia." Journal of Physics: Conference Series 1116: 032035.

Stoiber, R. E., Malinconico., L. L., and Williams, S. N., 1983, Use of the correlation spectrometer at volcanoes: In: Tazieff, H., Sabroux, J. -C. (Eds.), Forcasting Volcanic Events. Elsevier, Amsterdam, p. 425-444.

Sutton, A.J., Elias, T. and Kauahikaua, J., 2003, Lava-effusion rates for the Pu'u 'O¨ 'o¨-Ku¨paianaha eruption derived from SO2 emissions and Very Low Frequency (VLF) measurements. In: Heliker, C., Swanson, D.A. & Takahashi, T.J. (eds) The Puʻu ʻO¨ ʻo¨-Ku¨paianaha Eruption of Kı¨lauea Volcano, Hawaiʻi: The First 20 Years: US Geological Survey Professional Paper 1676, US Geological Survey, Reston, VA, p. 137–148

Theys, N., Campion, R., Clarisse, L., Brenot, H., van Gent, J., Dils, B., Corradini, S., Merucci, L., Coheur, P. F., Van Roozendael, M., Hurtmans, D., Clerbaux, C., Tait, S., and Ferrucci, F., 2013, Volcanic SO2 fluxes derived from satellite data: a survey using OMI, GOME-2, IASI and MODIS: Atmospheric Chemistry and Physics, v. 13, p. 5945–5968.

Ueda, A., and Sakai, H.,1984, Sulfur isotope study of Quaternary volcanic rocks from the Japanese Islands Arc: Grochimica et Cosmochimica Acta, v. 48, p. 1837-1848.

Vandaele, A. C., Simon, P. C., Guilmot, J. M., Carleer, M., and Colin, R., 1994, SO2 absorption cross section measurement in the UV using a Fourier transform spectrometer, Journal of Geophysical Research, v. 99, p. 25,599-25,605.

Witter, J. B., Kress, V. C., and Newhall, C. G., 2005, Volcán Popocatépetl, Mexico. Petrology, Magma Mixing, and Immediate Sources of Volatiles for the 1994–Present Eruption: Journal of Petrology, v. 46, no. 11, p. 2337-2366.

Wooster, M. J., Zhukov, B., and Oertel, D., 2003, Fire radiative energy for quantitative study of biomass burning: derivation from the BIRD experimental satellite and comparison to MODIS fire products: Remote Sensing of Environment, v. 86, no. 1, p. 83-107.

Wright, R., Flynn, L. P., Garbeil, H., Harris, A. J. L., Pilger, E., 2004, MODVOLC: near-real-time thermal monitoring of global volcanism: Journal of Volcanology and Geothermal Research, v. 135, p. 20.

Wright, R., Blackett, M., and Hill-Butler, C., 2015, Some observations regarding the thermal flux from Earth's erupting volcanoes for the period of 2000 to 2014: Geophysical Research Letters, v. 42, no. 2, p. 282-289.

Wright, R., 2016, MODVOLC: 14 years of autonomous observations of effusive volcanism from space: Geological Society, London, Special Publications, v. 426, no. 1, p. 23-53.

Zakšek, K., Shirzaei, M., Hort, M., Pyle, D. M., Mather, T. A., and Biggs, J., 2013, Constraining the uncertainties of volcano thermal anomaly monitoring using a

Kalman filter technique, Remote Sensing of Volcanoes and Volcanic Processes: Integrating Observation and Modelling: Geological Society of London, v. 380.

A Appendix

A.1 VRE-SO_2 Time Series Plots

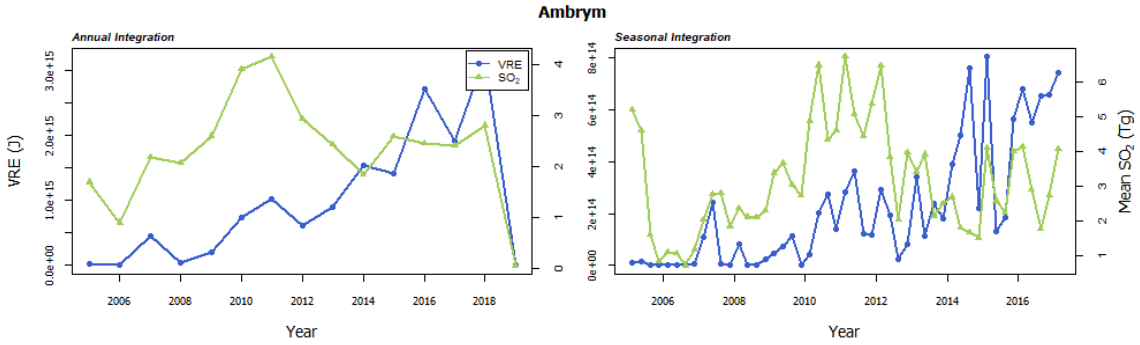

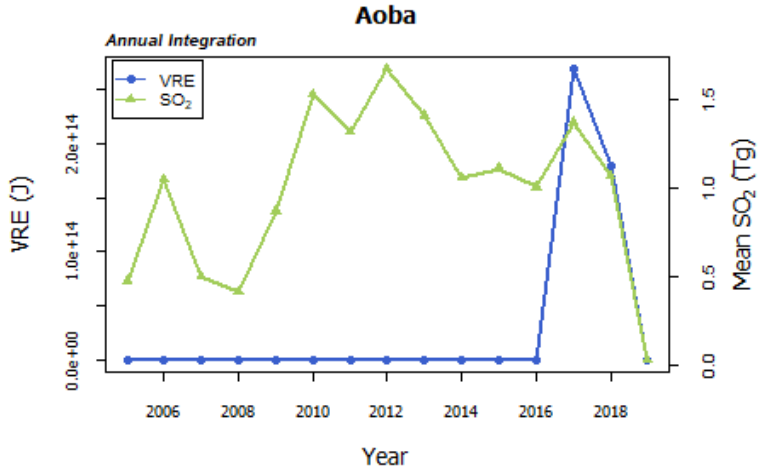

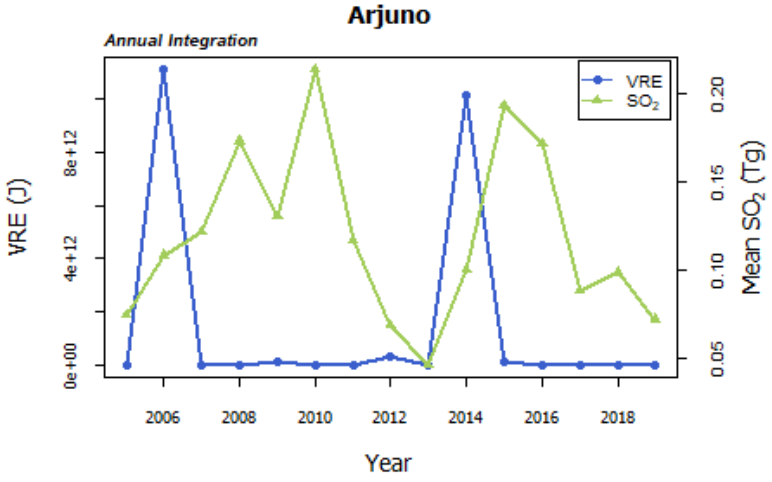

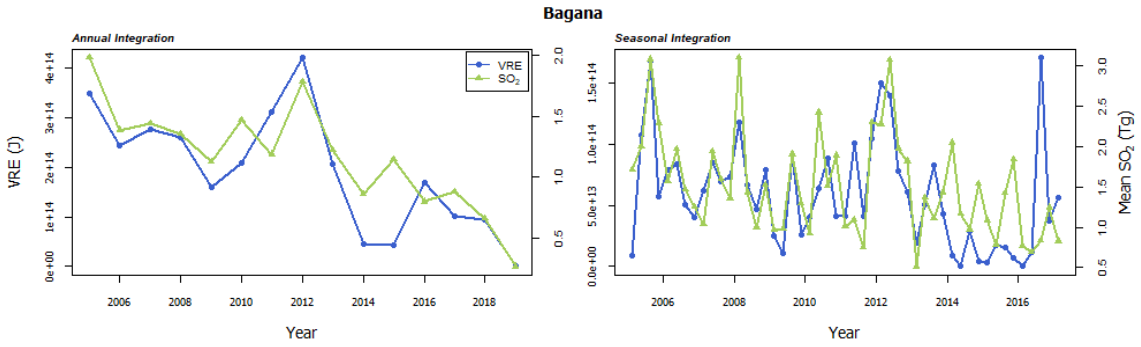
Bagana
Annual Integration
Seasonal Integration
VRE
SO2
VRE (J)
Mean SO2 (Tg)
Year

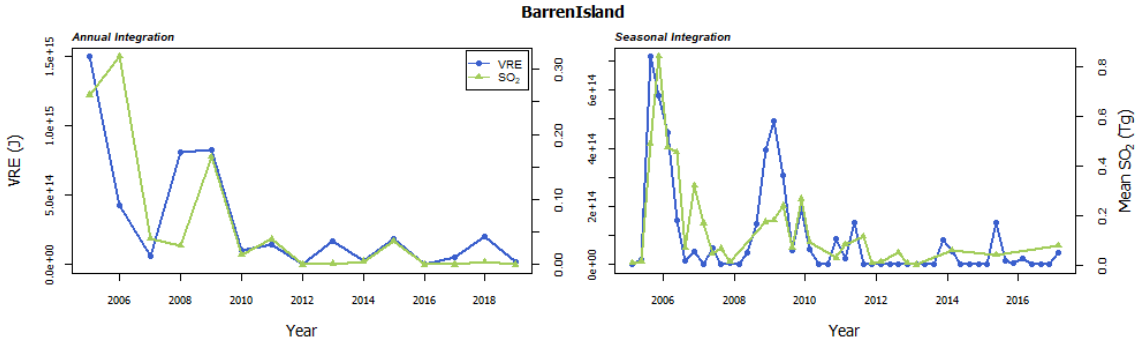
BarrenIsland
Annual Integration
Seasonal Integration
VRE
SO2
VRE (J)
Mean SO2 (Tg)
Year

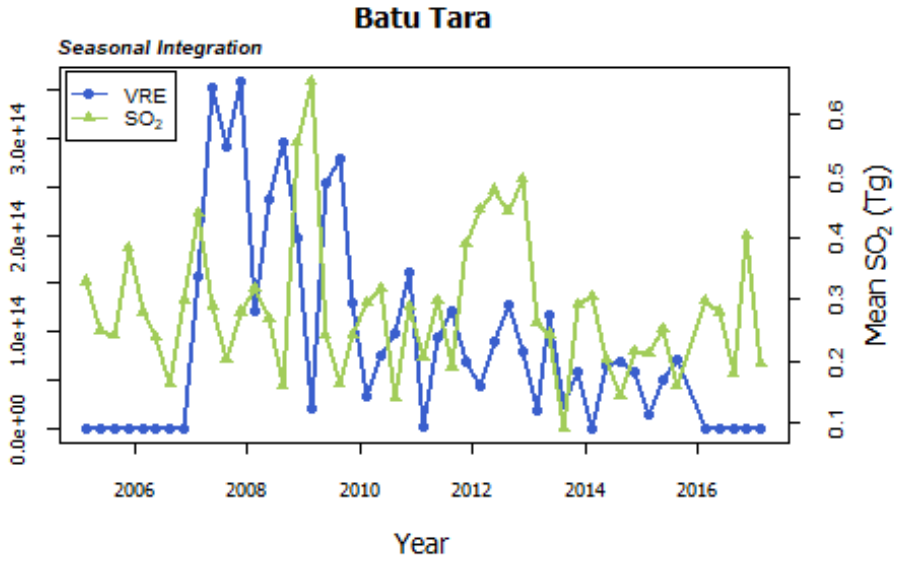
Batu Tara
Seasonal Integration
VRE
SO2
Mean SO2 (Tg)
Year

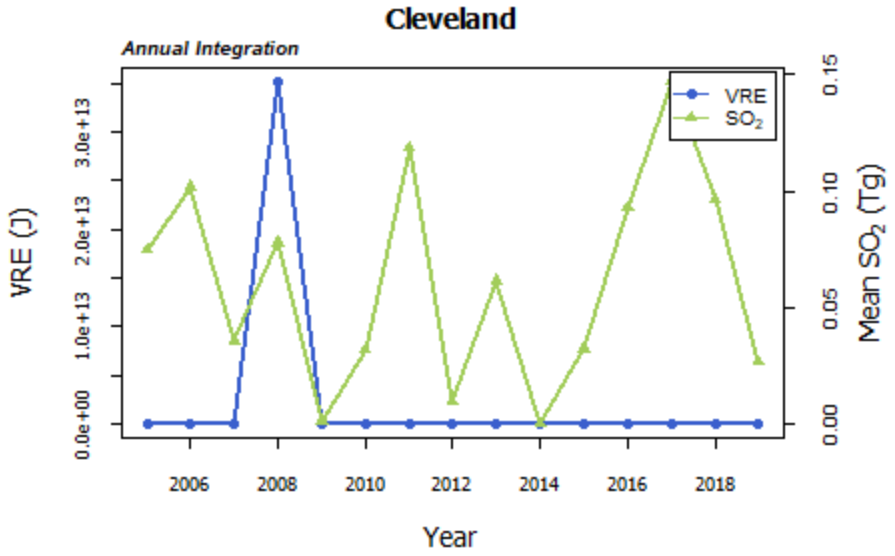
Cleveland
Annual Integration
VRE
SO2
VRE (J)
Mean SO2 (Tg)
Year

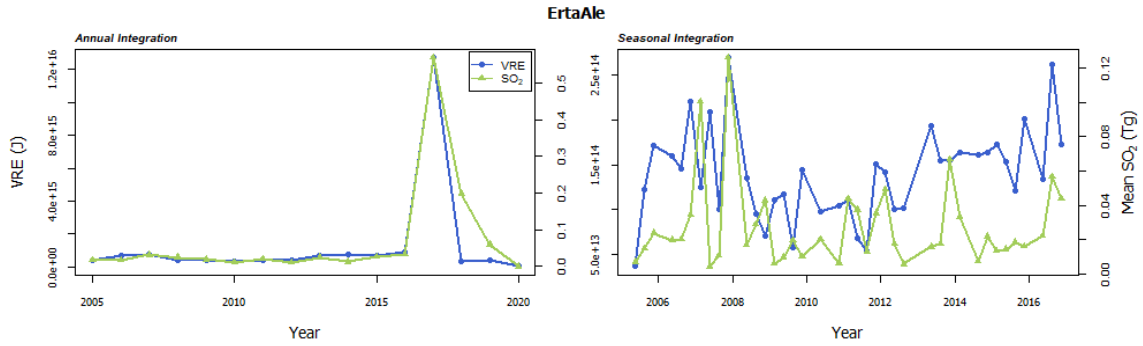
ErtaAle
Annual Integration
Seasonal Integration
VRE
SO2
VRE (J)
Mean SO2 (Tg)
Year

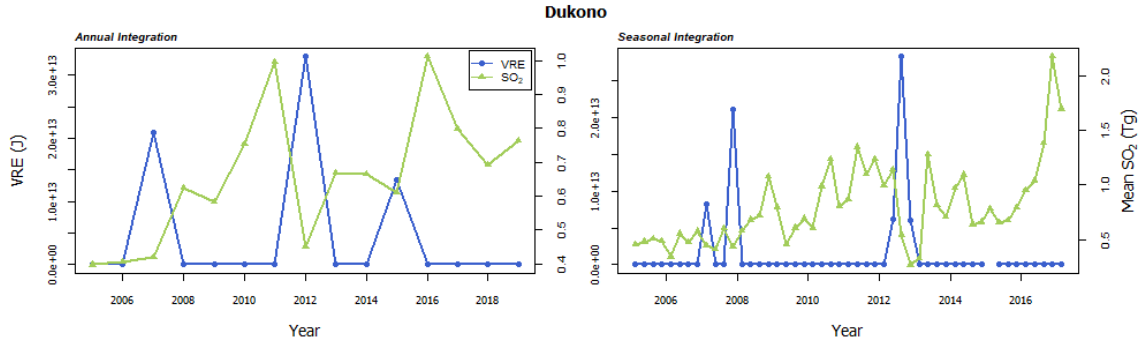
Dukono
Annual Integration
Seasonal Integration
VRE
SO2
VRE (J)
Mean SO2 (Tg)
Year

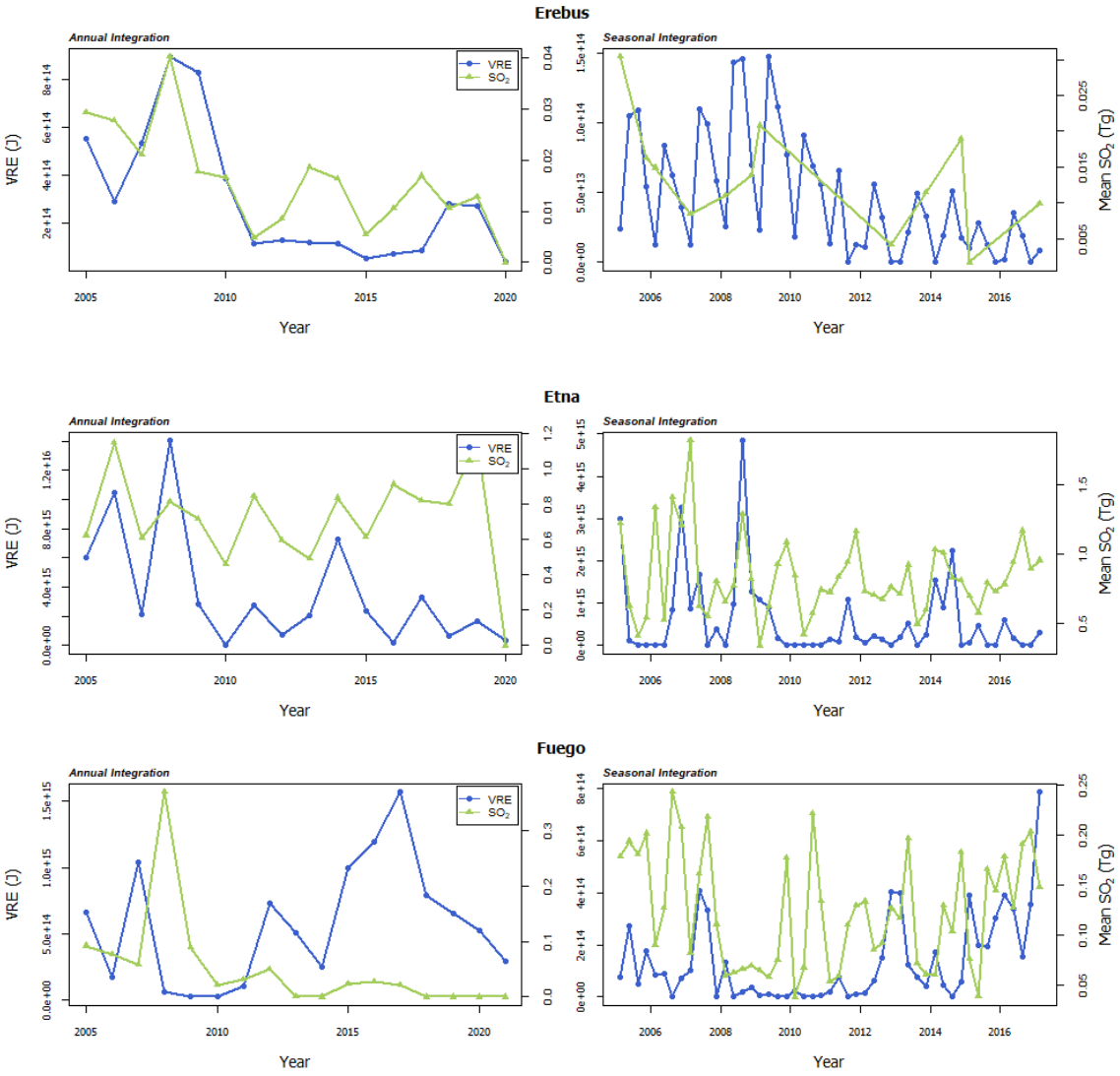
Erebus
Annual Integration
Seasonal Integration
VRE
SO2
VRE (J)
Mean SO2 (Tg)
Year
Etna
Annual Integration
Seasonal Integration
VRE
SO2
VRE (J)
Mean SO2 (Tg)
Year
Fuego
Annual Integration
Seasonal Integration
VRE
SO2
VRE (J)
Mean SO2 (Tg)
Year

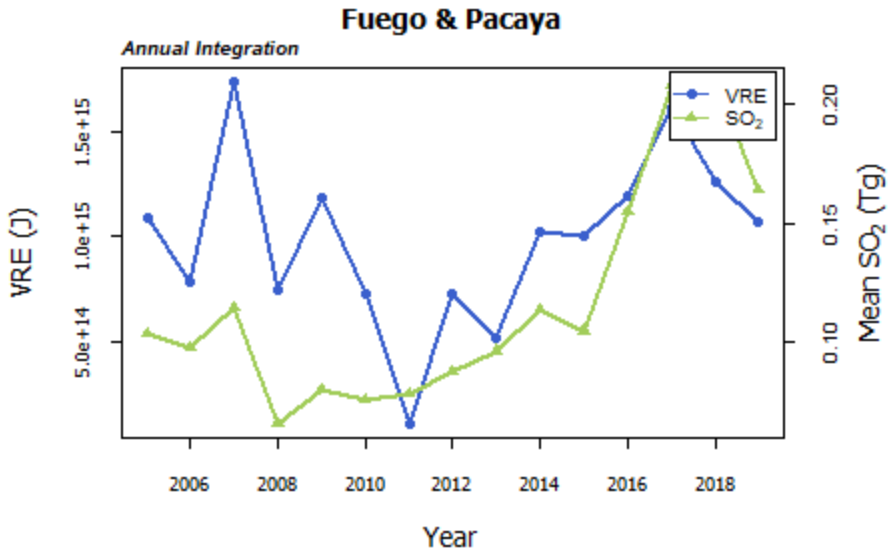
Fuego & Pacaya
Annual Integration
VRE
SO2
VRE (J)
Mean SO2 (Tg)
Year

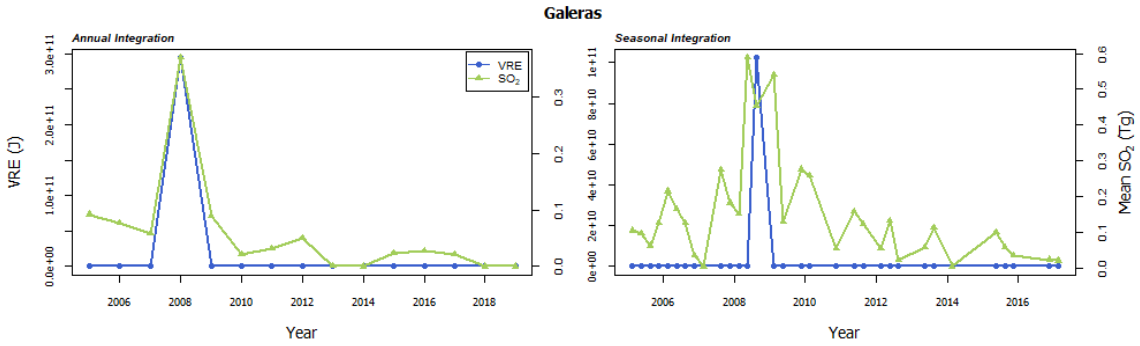
Galeras
Annual Integration
Seasonal Integration
VRE
SO2
VRE (J)
Mean SO2 (Tg)
Year

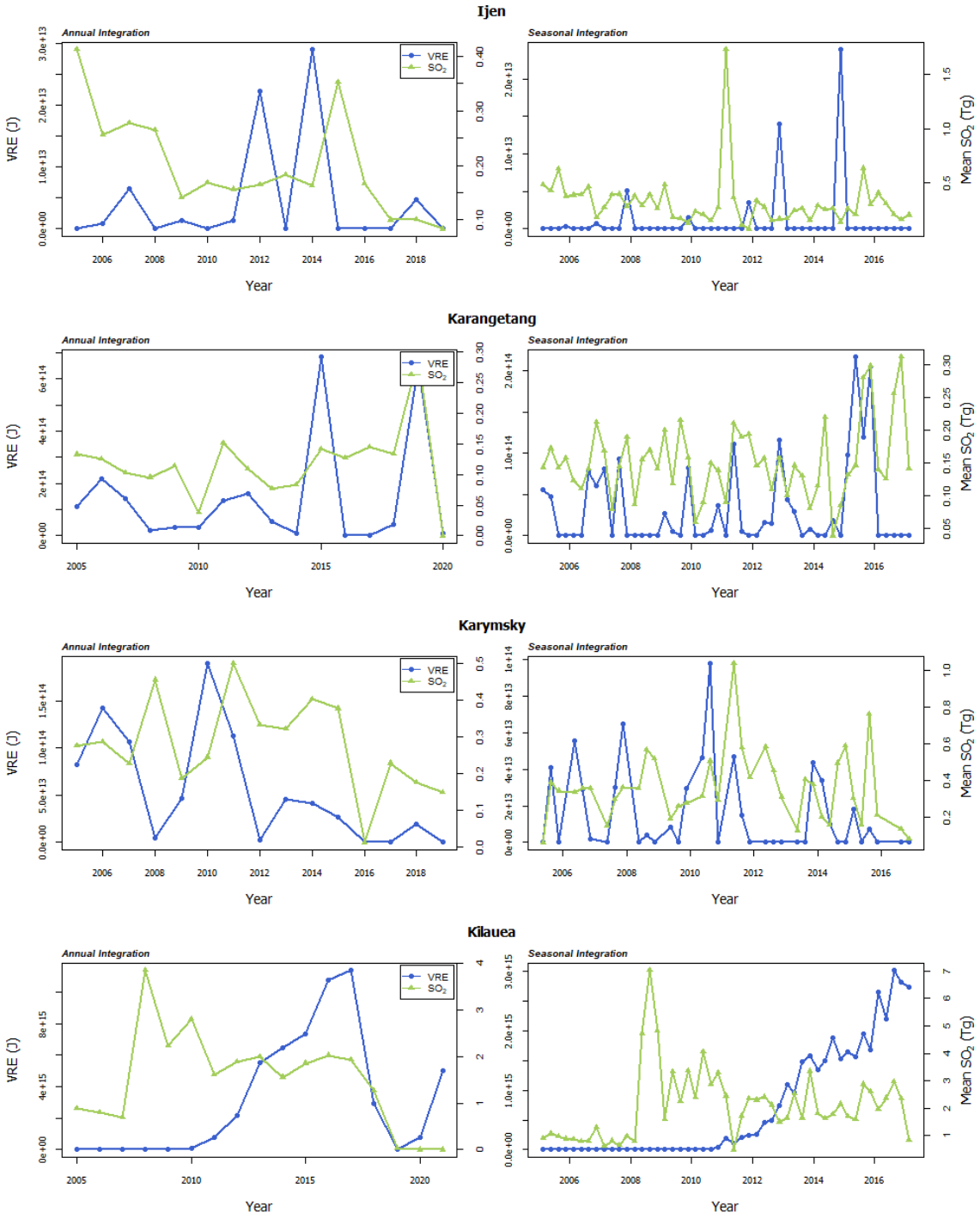
Ijen
Annual Integration
Seasonal Integration
VRE
SO2
VRE (J)
Mean SO2 (Tg)
Year
Karangetang
Karymsky
Kilauea

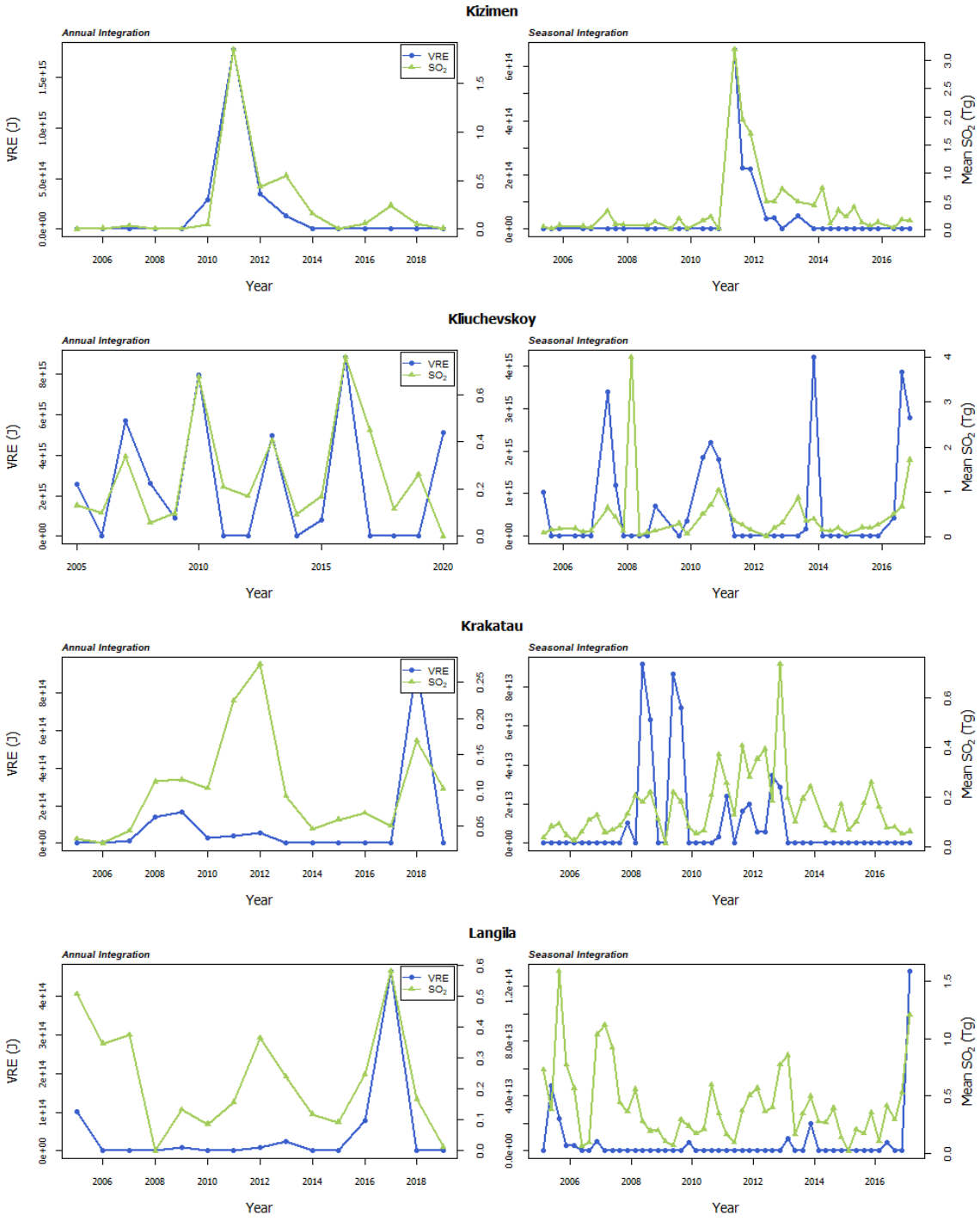
Kizimen
Annual Integration
Seasonal Integration
VRE
SO2
VRE (J)
Mean SO2 (Tg)
Year
Kliuchevskoy
Annual Integration
Seasonal Integration
VRE
SO2
VRE (J)
Mean SO2 (Tg)
Year
Krakatau
Annual Integration
Seasonal Integration
VRE
SO2
VRE (J)
Mean SO2 (Tg)
Year
Langila
Annual Integration
Seasonal Integration
VRE
SO2
VRE (J)
Mean SO2 (Tg)
Year

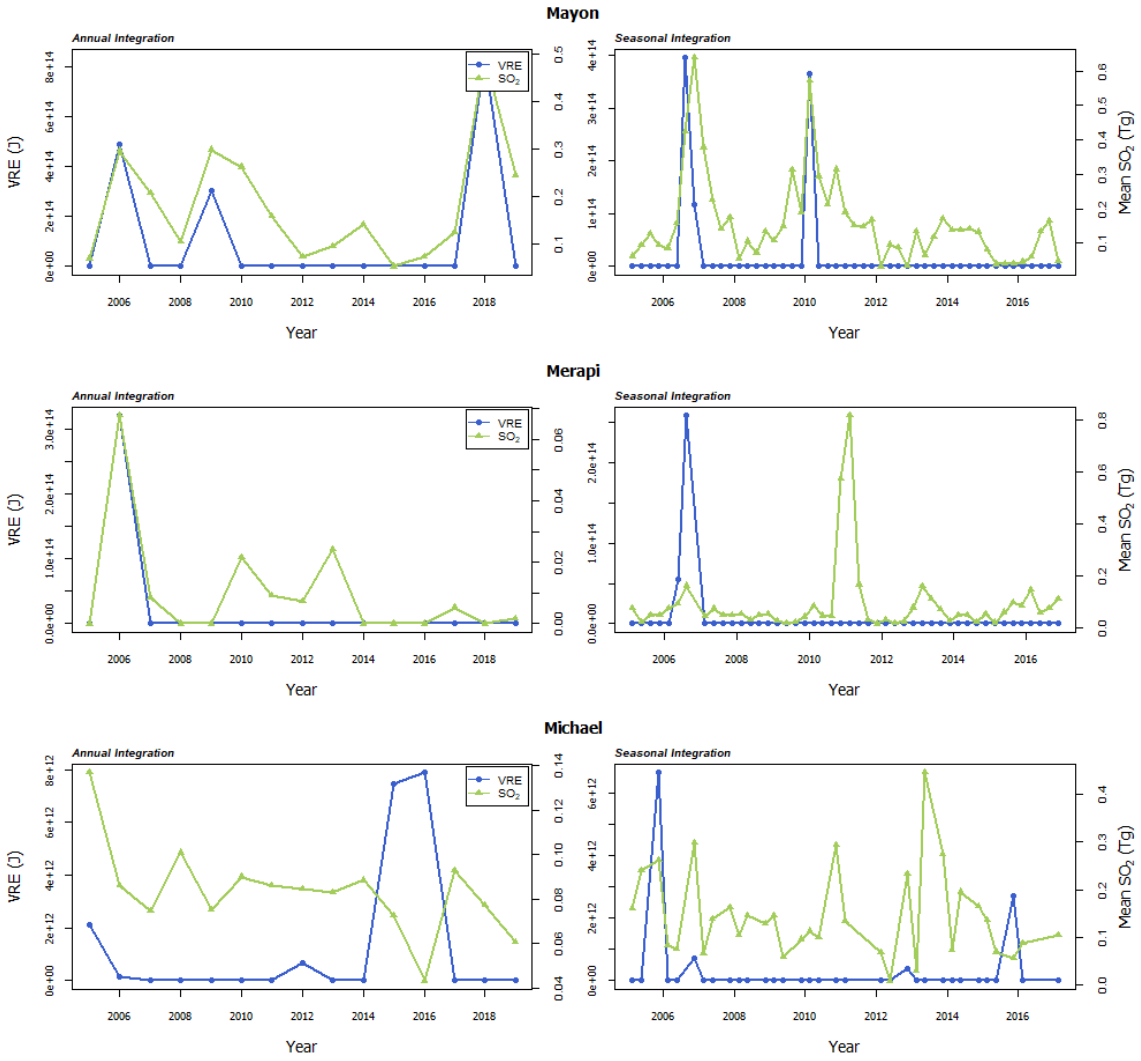
Mayon
Annual Integration
Seasonal Integration
VRE
SO2
VRE (J)
Mean SO2 (Tg)
Year
Merapi
Annual Integration
Seasonal Integration
VRE
SO2
VRE (J)
Mean SO2 (Tg)
Year
Michael
Annual Integration
Seasonal Integration
VRE
SO2
VRE (J)
Mean SO2 (Tg)
Year

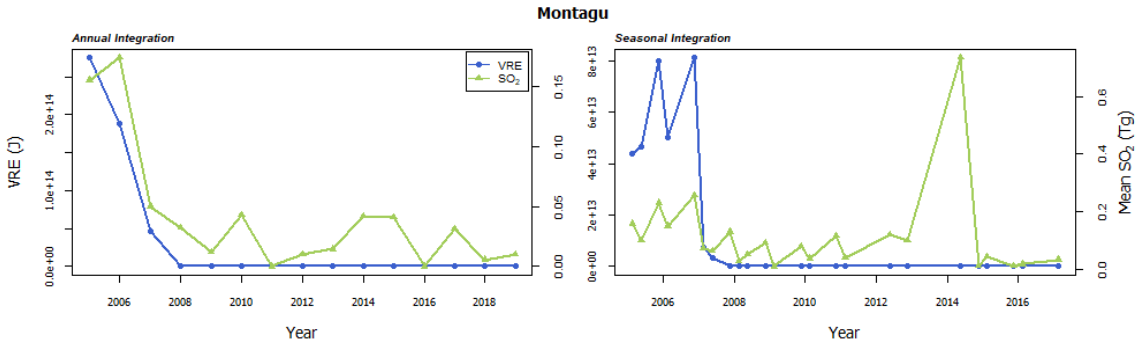
Montagu
Annual Integration
Seasonal Integration
VRE
SO2
VRE (J)
Mean SO2 (Tg)
Year

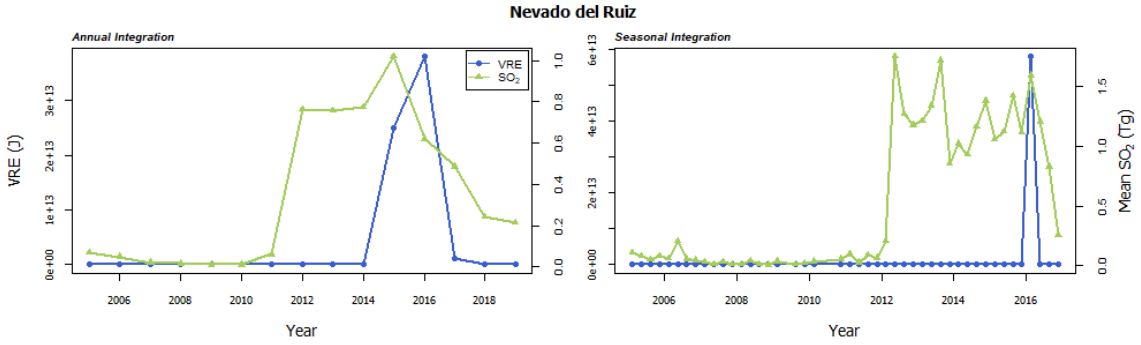
Nevado del Ruiz
Annual Integration
Seasonal Integration
VRE
SO2
VRE (J)
Mean SO2 (Tg)
Year

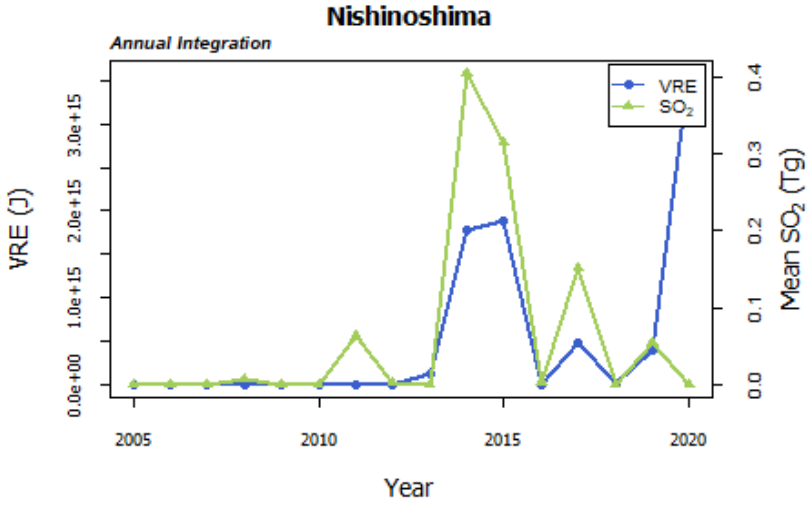
Nishinoshima
Annual Integration
VRE
SO2
VRE (J)
Mean SO2 (Tg)
Year

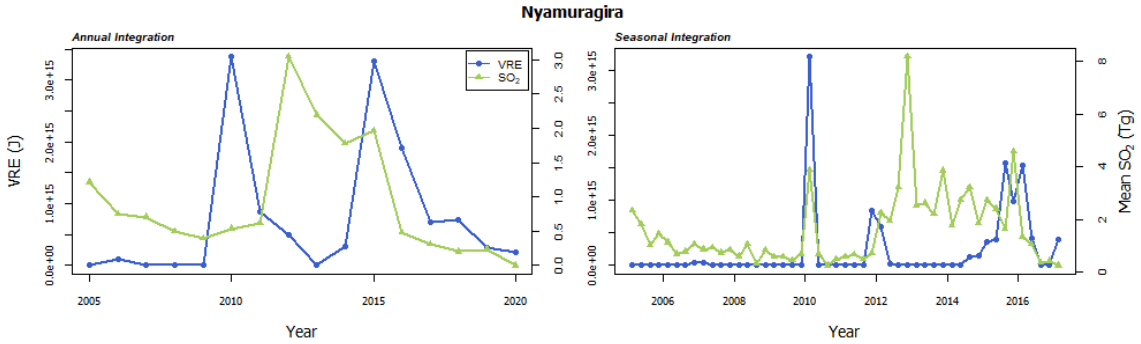
Nyamuragira
Annual Integration
Seasonal Integration
VRE
SO2
VRE (J)
Mean SO2 (Tg)
Year

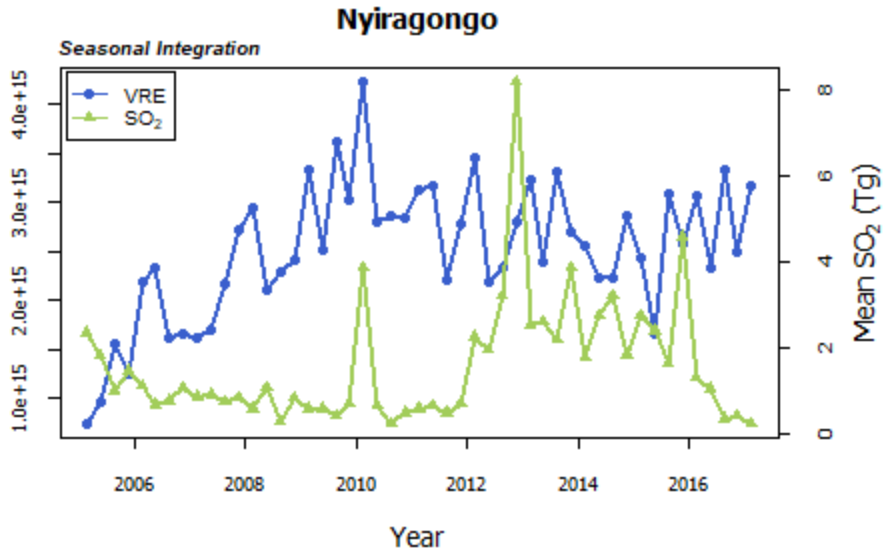
Nyiragongo
Seasonal Integration
VRE
SO2
1.0e+15
2.0e+15
3.0e+15
4.0e+15
0
2
4
6
8
Mean SO2 (Tg)
2006
2008
2010
2012
2014
2016
Year

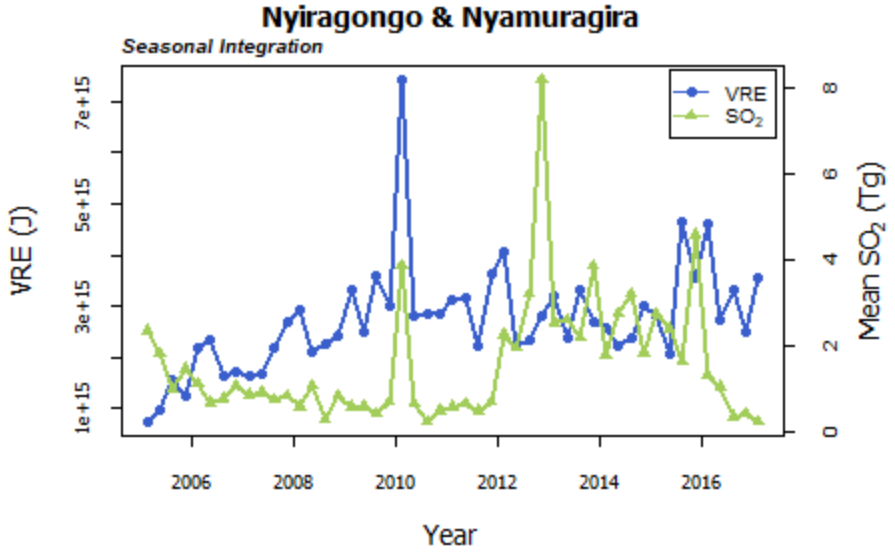
Nyiragongo & Nyamuragira
Seasonal Integration
VRE
SO2
1e+15
3e+15
5e+15
7e+15
VRE (J)
0
2
4
6
8
Mean SO2 (Tg)
2006
2008
2010
2012
2014
2016
Year

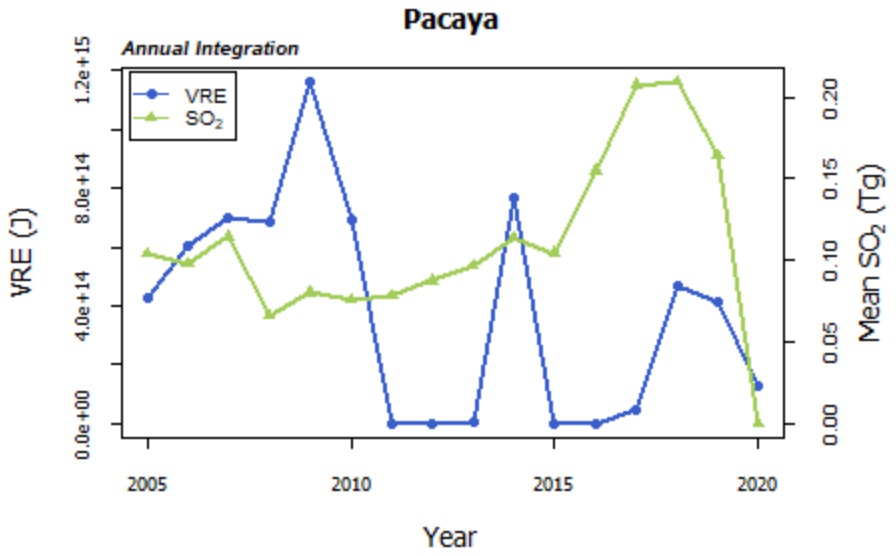
Pacaya
Annual Integration
VRE
SO2
VRE (J)
Mean SO2 (Tg)
Year

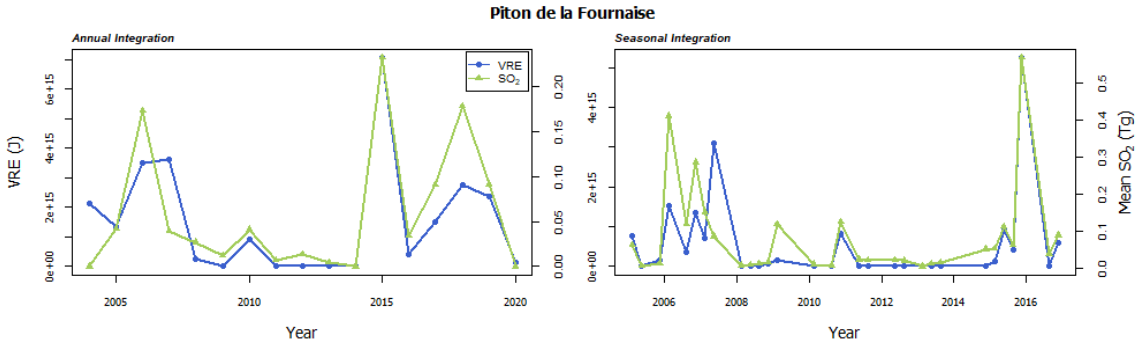
Piton de la Fournaise
Annual Integration
Seasonal Integration
VRE
SO2
VRE (J)
Mean SO2 (Tg)
Year

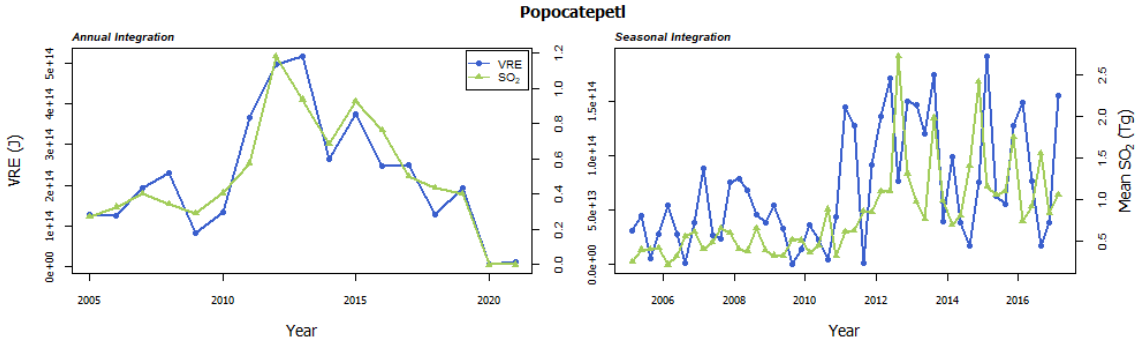
Popocatepetl
Annual Integration
Seasonal Integration
VRE
SO2
VRE (J)
Mean SO2 (Tg)
Year

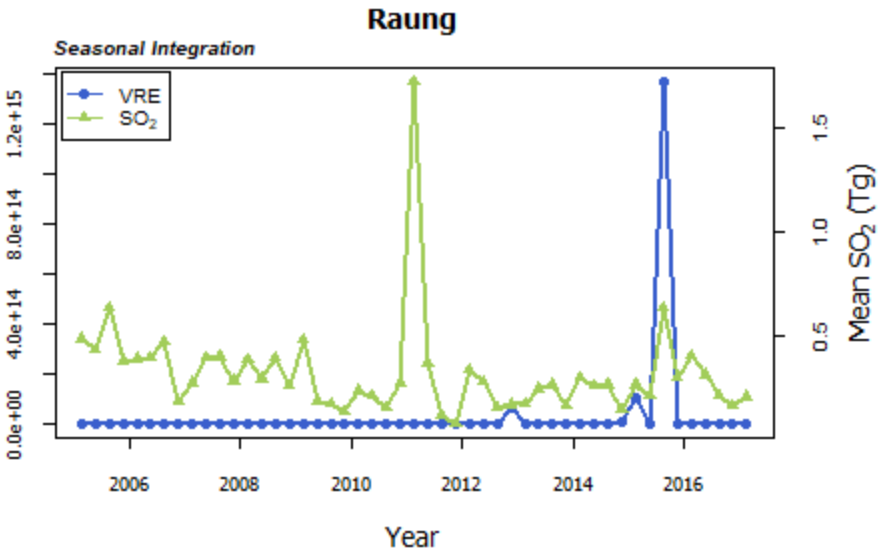
Raung
Seasonal Integration
VRE
SO2
0.0e+00
4.0e+14
8.0e+14
1.2e+15
0.5
1.0
1.5
Mean SO2 (Tg)
2006
2008
2010
2012
2014
2016
Year

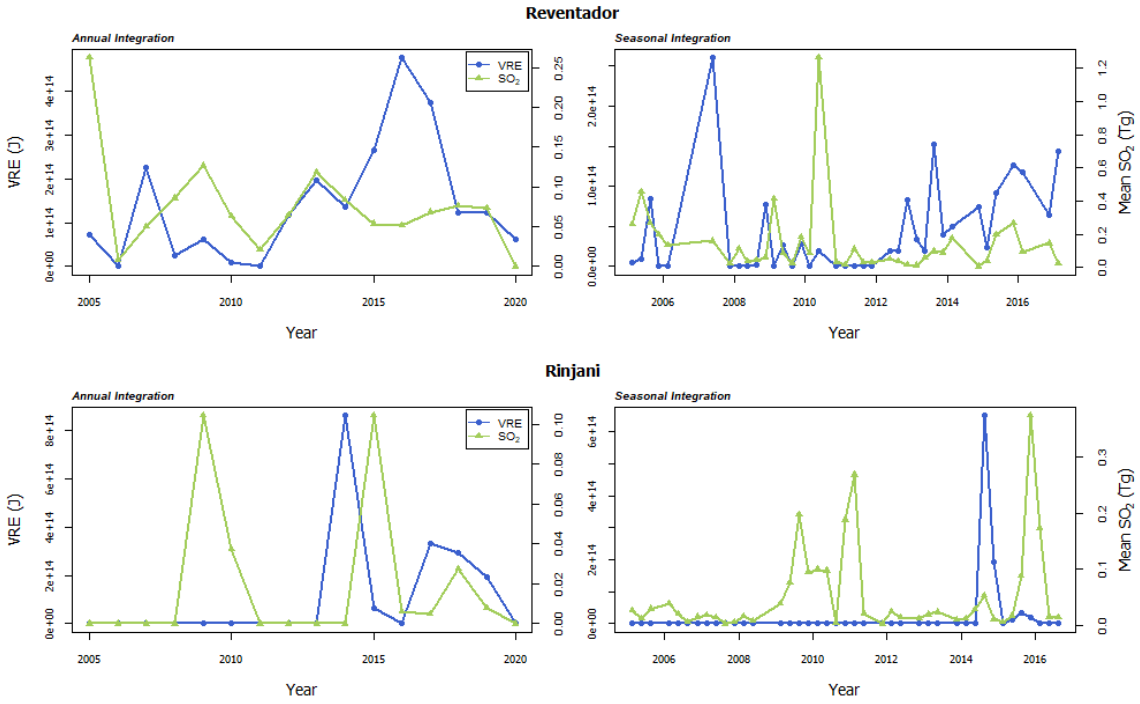
Reventador
Annual Integration
VRE
SO2
VRE (J)
Year
Seasonal Integration
Mean SO2 (Tg)
Year
Rinjani
Annual Integration
VRE
SO2
VRE (J)
Year
Seasonal Integration
Mean SO2 (Tg)
Year

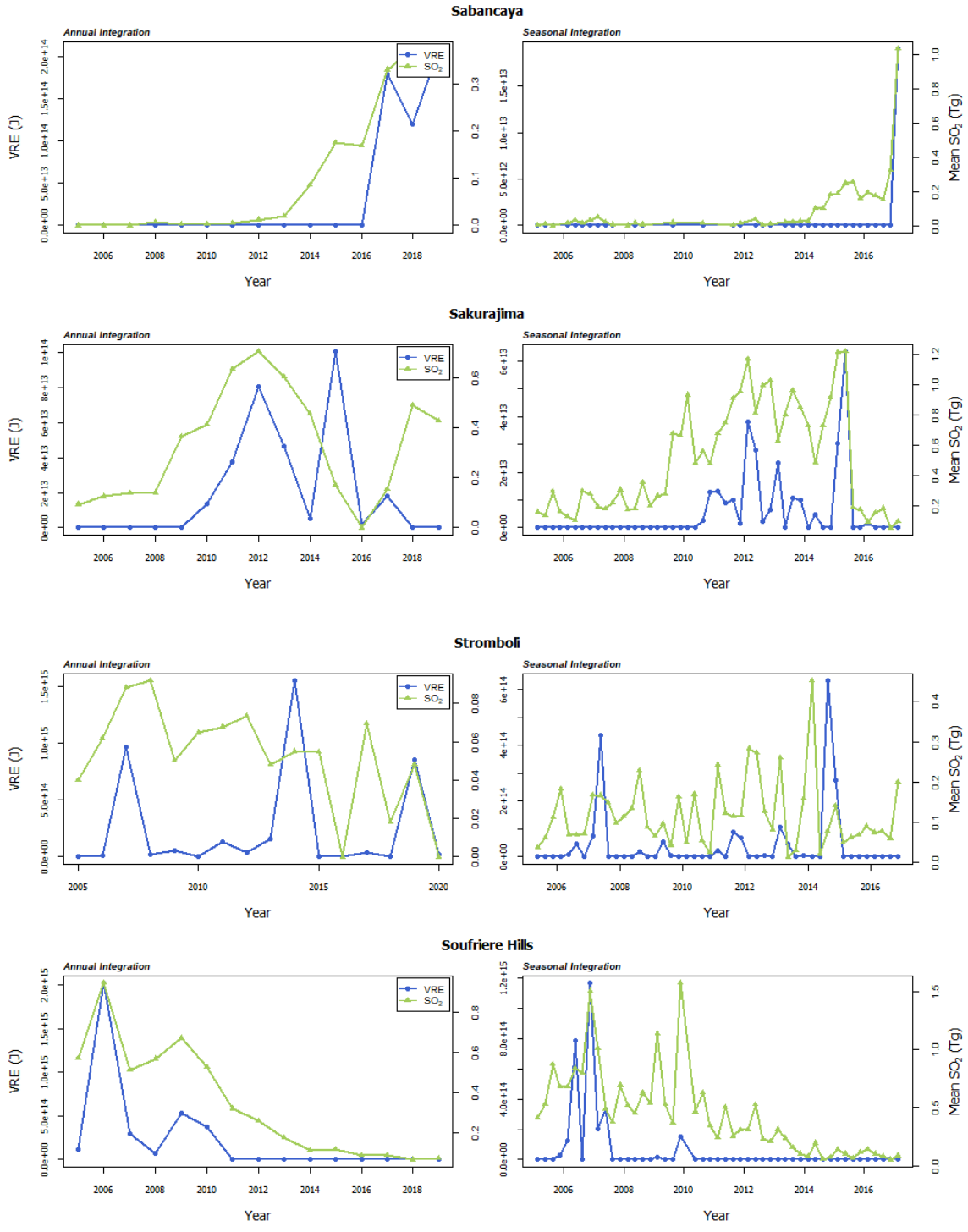
Sabancaya
Annual Integration
Seasonal Integration
VRE
SO2
VRE (J)
Mean SO2 (Tg)
Year
Sakurajima
Annual Integration
Seasonal Integration
VRE
SO2
VRE (J)
Mean SO2 (Tg)
Year
Stromboli
Annual Integration
Seasonal Integration
VRE
SO2
VRE (J)
Mean SO2 (Tg)
Year
Soufriere Hills
Annual Integration
Seasonal Integration
VRE
SO2
VRE (J)
Mean SO2 (Tg)
Year

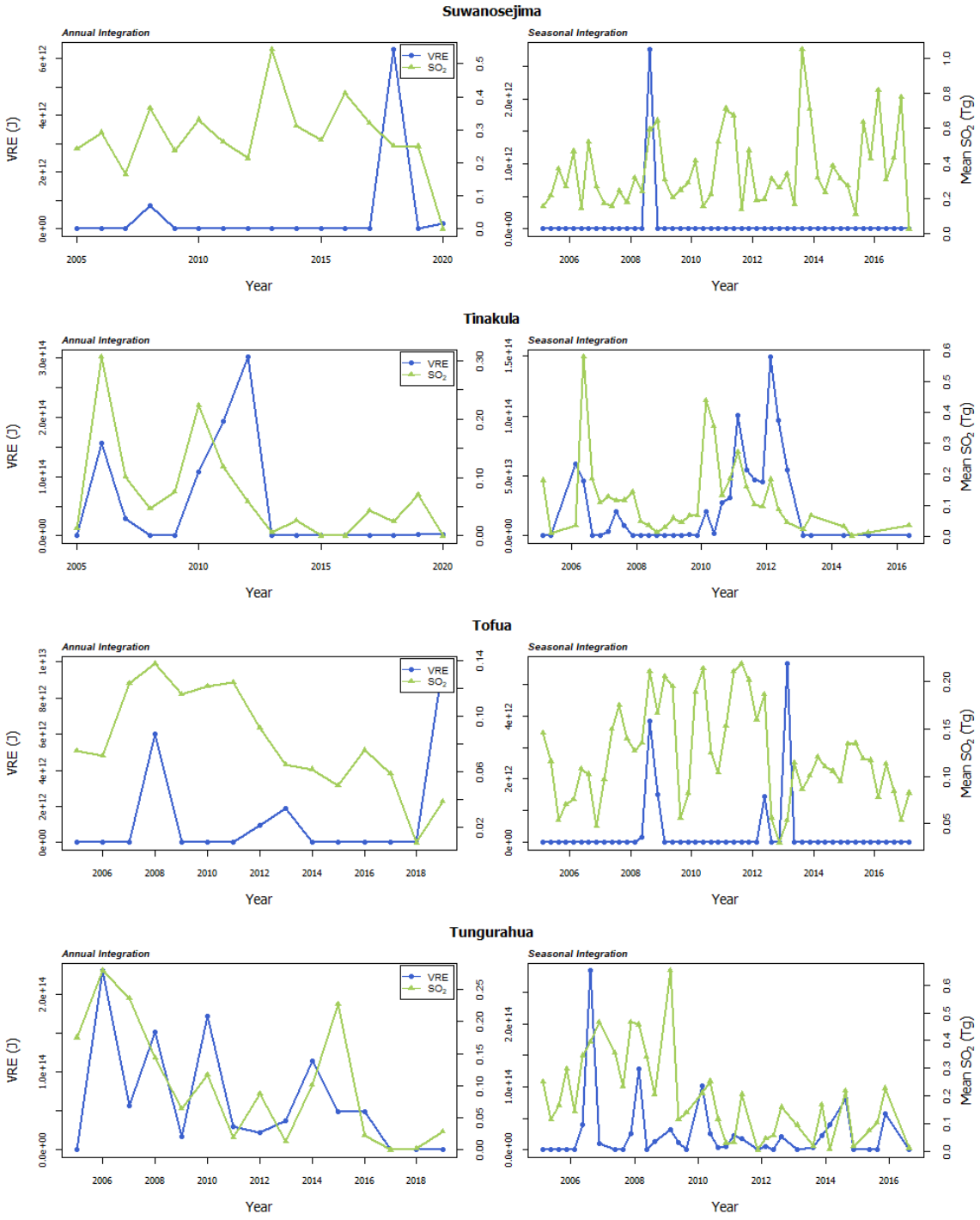
Suwanosejima
Annual Integration
Seasonal Integration
VRE
SO2
VRE (J)
Mean SO2 (Tg)
Year
Tinakula
Annual Integration
Seasonal Integration
VRE
SO2
VRE (J)
Mean SO2 (Tg)
Year
Tofua
Annual Integration
Seasonal Integration
VRE
SO2
VRE (J)
Mean SO2 (Tg)
Year
Tungurahua
Annual Integration
Seasonal Integration
VRE
SO2
VRE (J)
Mean SO2 (Tg)
Year

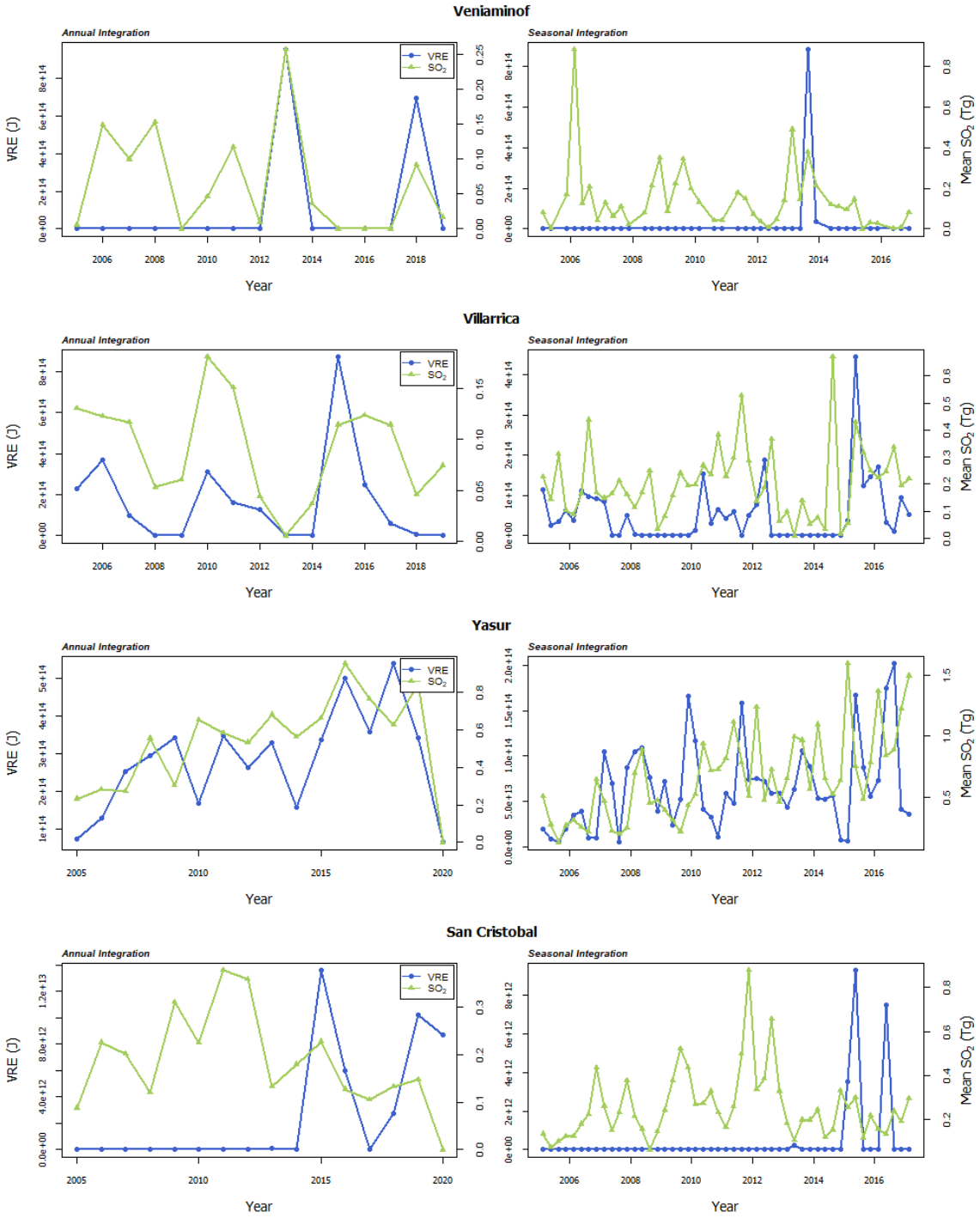
Veniaminof
Annual Integration
Seasonal Integration
VRE
SO2
VRE (J)
Mean SO2 (Tg)
Year
Villarrica
Annual Integration
Seasonal Integration
VRE
SO2
VRE (J)
Mean SO2 (Tg)
Year
Yasur
Annual Integration
Seasonal Integration
VRE
SO2
VRE (J)
Mean SO2 (Tg)
Year
San Cristobal
Annual Integration
Seasonal Integration
VRE
SO2
VRE (J)
Mean SO2 (Tg)
Year

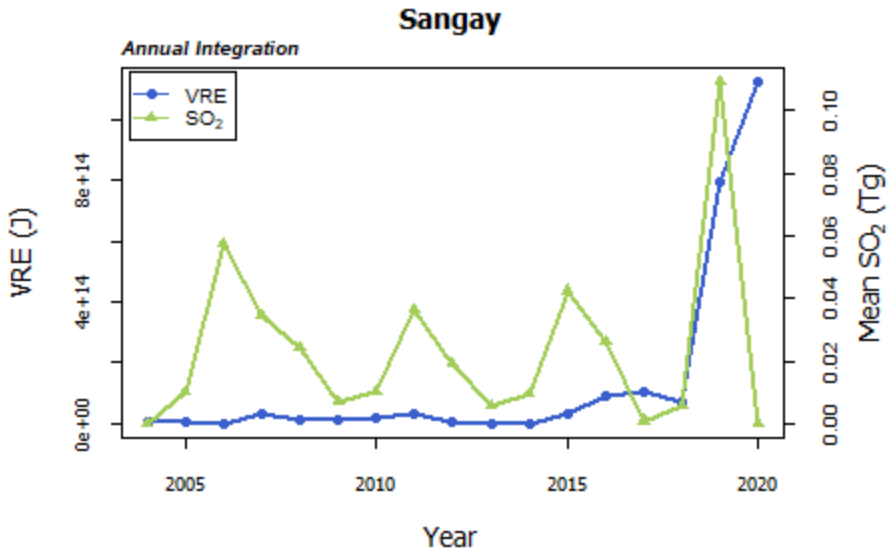
Sangay
Annual Integration
VRE
SO2
VRE (J)
Mean SO2 (Tg)
Year

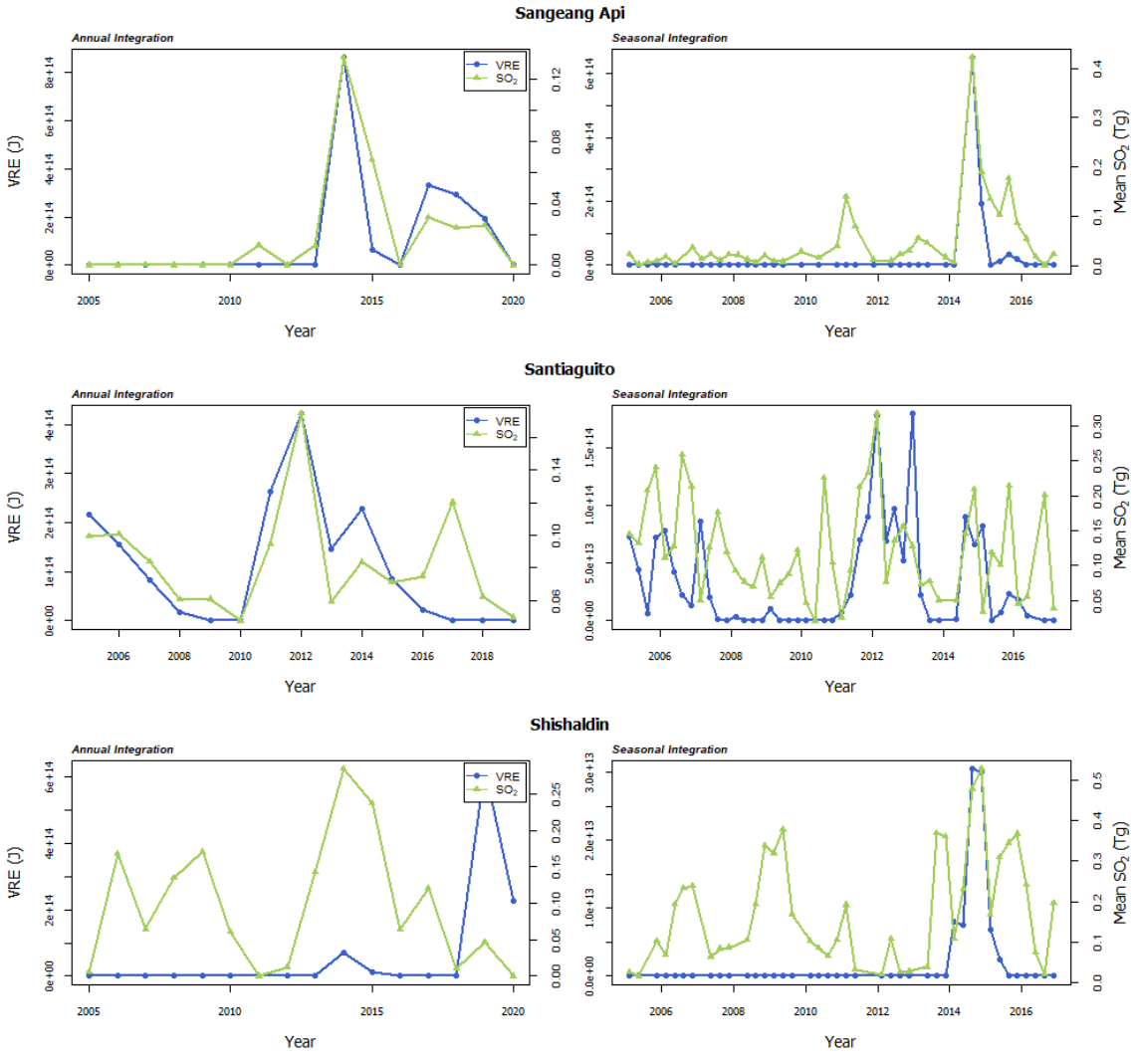
Sangeang Api
Annual Integration
Seasonal Integration
Santiaguito
Annual Integration
Seasonal Integration
Shishaldin
Annual Integration
Seasonal Integration
VRE
SO2
VRE (J)
Mean SO2 (Tg)
Year

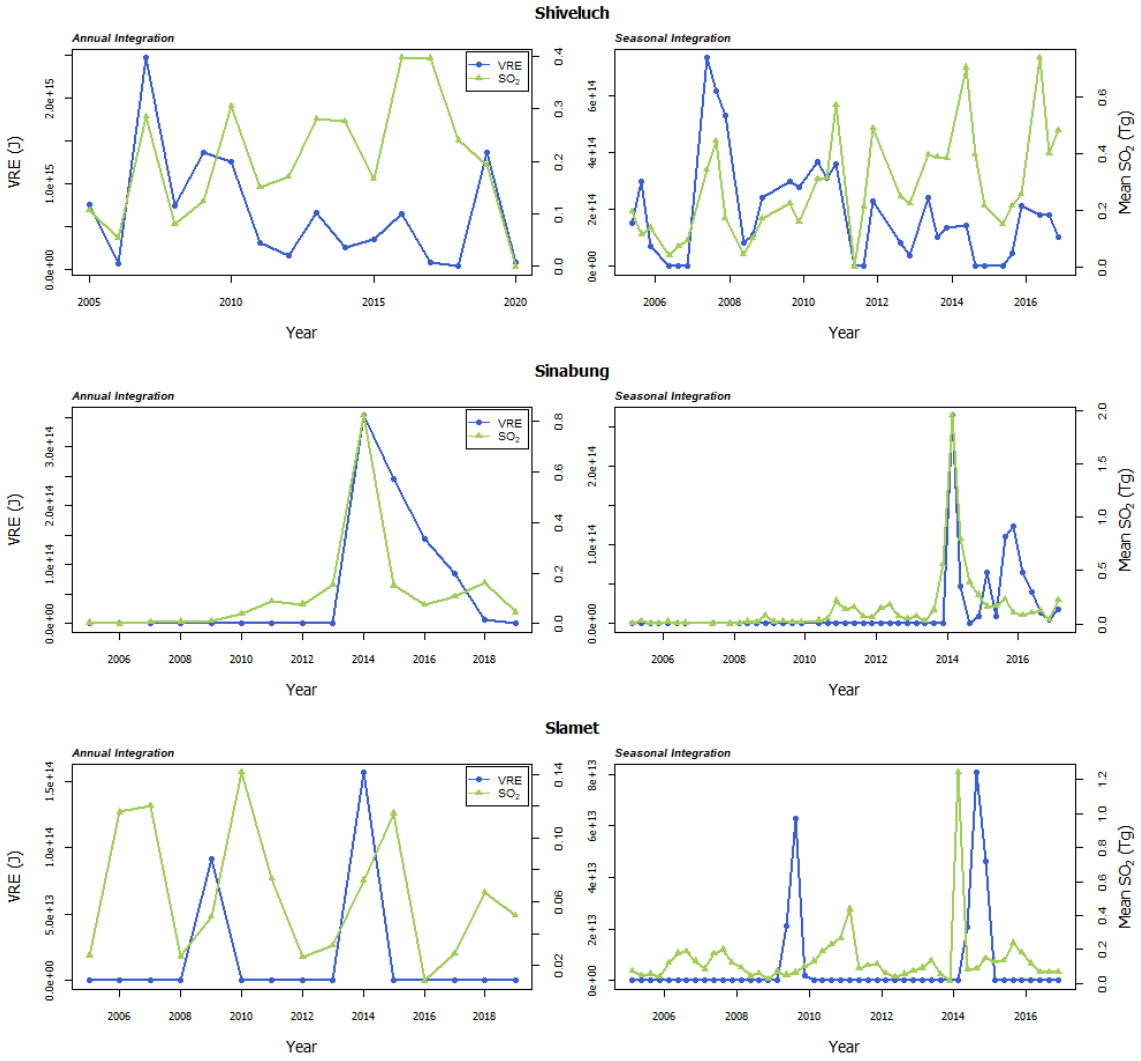
Shiveluch
Annual Integration
Seasonal Integration
VRE
SO2
VRE (J)
Mean SO2 (Tg)
Year
Sinabung
Annual Integration
Seasonal Integration
VRE
SO2
VRE (J)
Mean SO2 (Tg)
Year
Slamet
Annual Integration
Seasonal Integration
VRE
SO2
VRE (J)
Mean SO2 (Tg)
Year

A.2 VRE-SO_2 Regression Plots

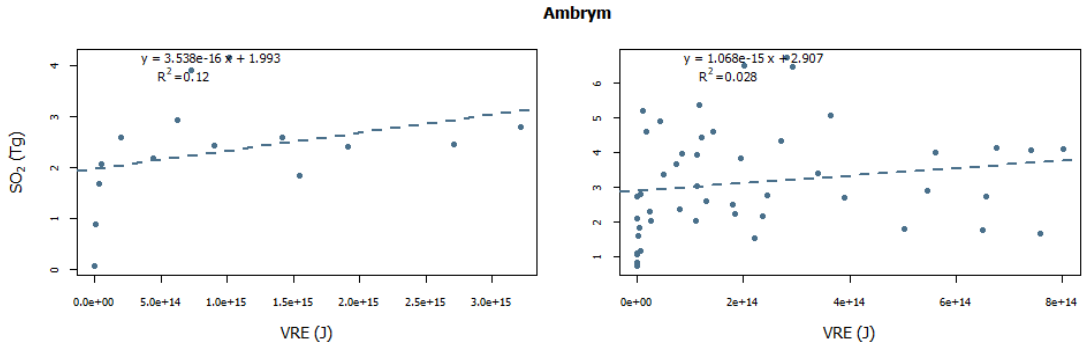

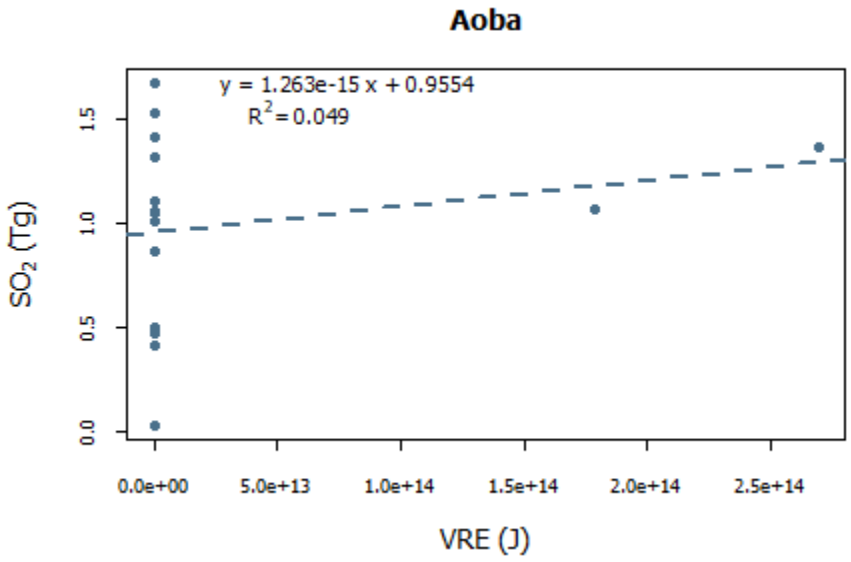

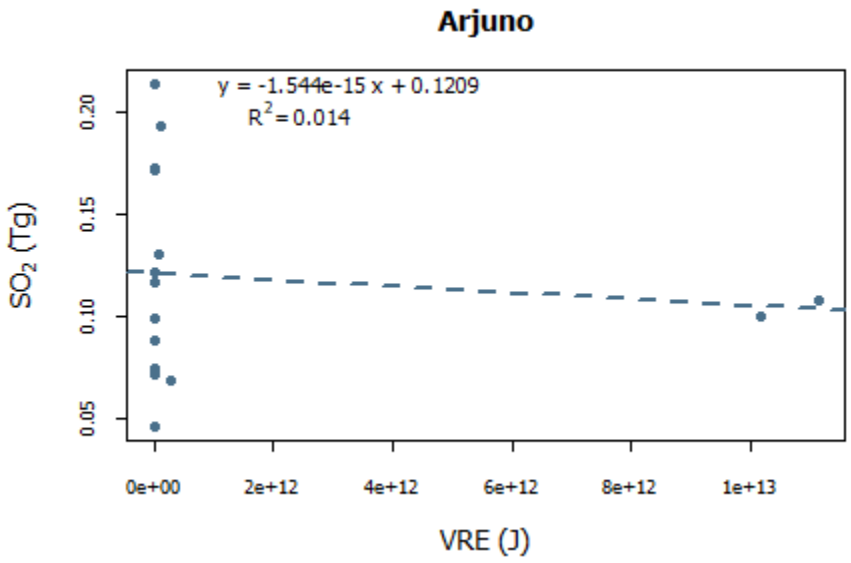

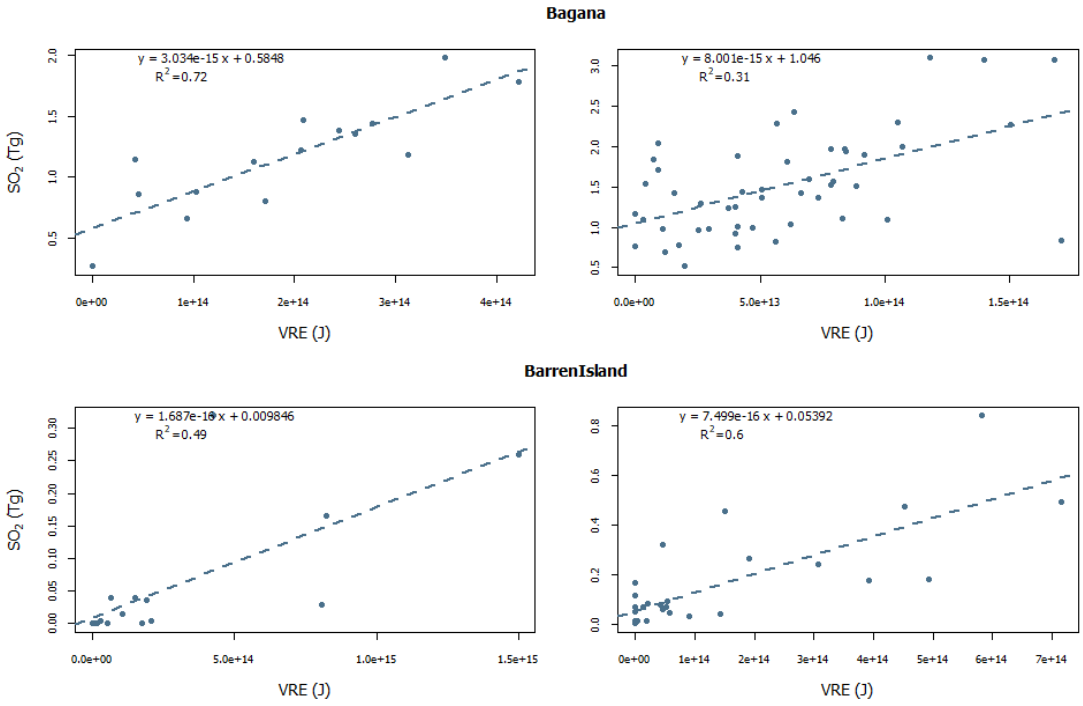
Bagana
y = 3.034e-15 x + 0.5848
R² = 0.72
y = 8.001e-15 x + 1.046
R² = 0.31
SO2 (Tg)
VRE (J)
BarrenIsland
y = 7.499e-16 x + 0.05392
R² = 0.6
SO2 (Tg)
VRE (J)

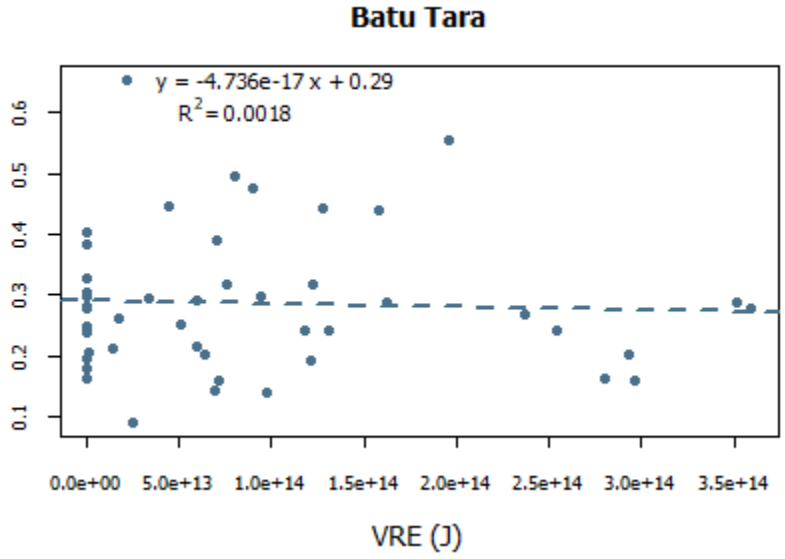
Batu Tara
y = -4.736e-17 x + 0.29
R² = 0.0018
VRE (J)

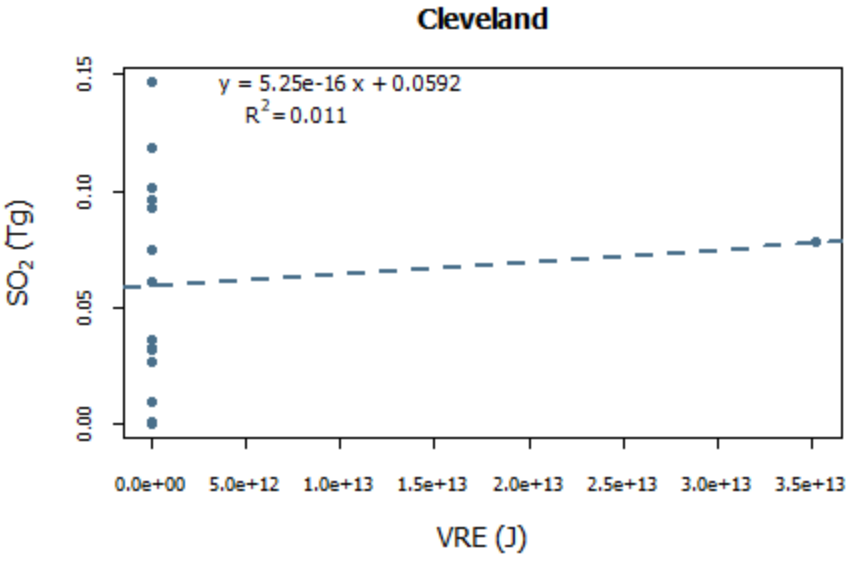
Cleveland
y = 5.25e-16 x + 0.0592
R2 = 0.011
SO2 (Tg)
0.00
0.05
0.10
0.15
0.0e+00
5.0e+12
1.0e+13
1.5e+13
2.0e+13
2.5e+13
3.0e+13
3.5e+13
VRE (J)

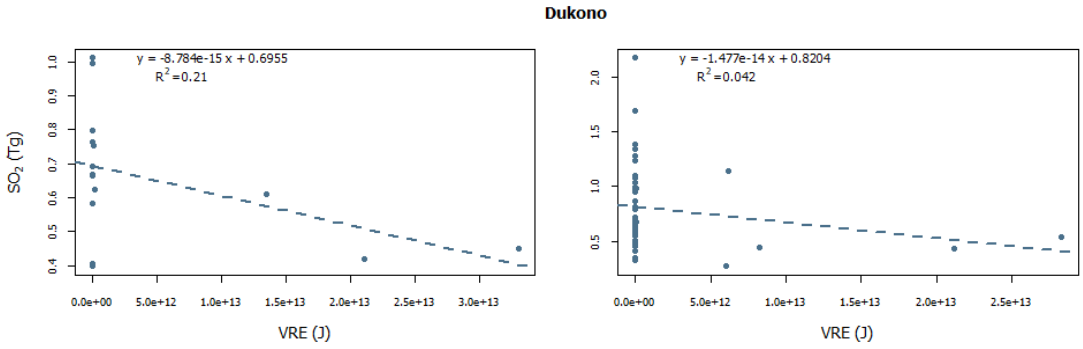
Dukono
y = -8.784e-15 x + 0.6955
R2 = 0.21
SO2 (Tg)
VRE (J)
y = -1.477e-14 x + 0.8204
R2 = 0.042
VRE (J)

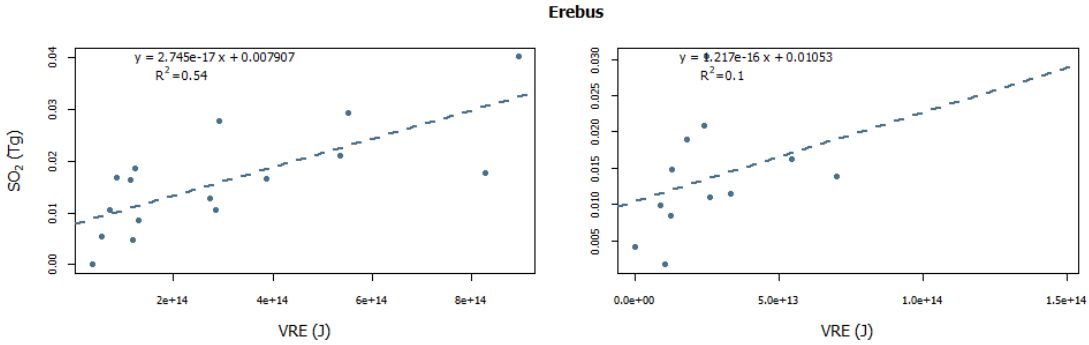
Erebus
y = 2.745e-17 x + 0.007907
R2 = 0.54
SO2 (Tg)
VRE (J)
y = 1.217e-16 x + 0.01053
R2 = 0.1
VRE (J)

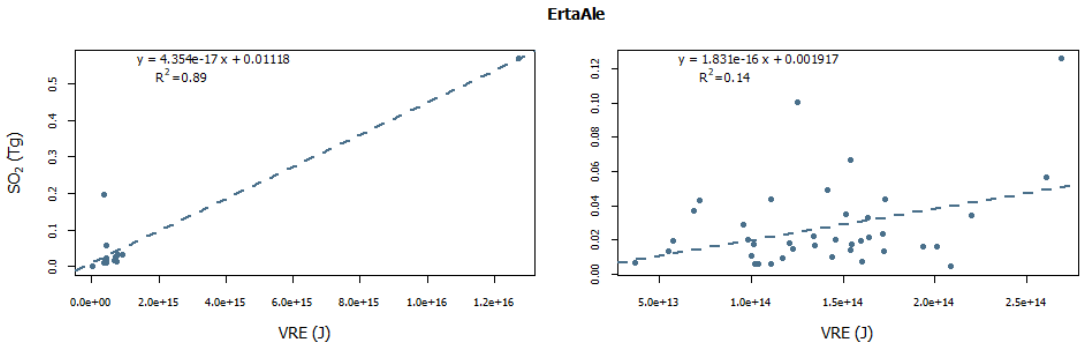
ErtaAle
y = 4.354e-17 x + 0.01118
R2 = 0.89
SO2 (Tg)
VRE (J)
y = 1.831e-16 x + 0.001917
R2 = 0.14
VRE (J)

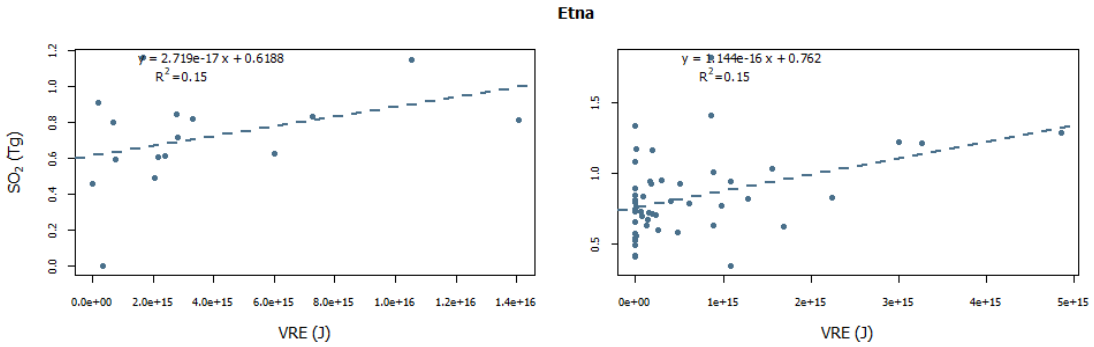
Etna
y = 2.719e-17 x + 0.6188
R2 = 0.15
y = 8.144e-16 x + 0.762
R2 = 0.15
SO2 (Tg)
VRE (J)
VRE (J)

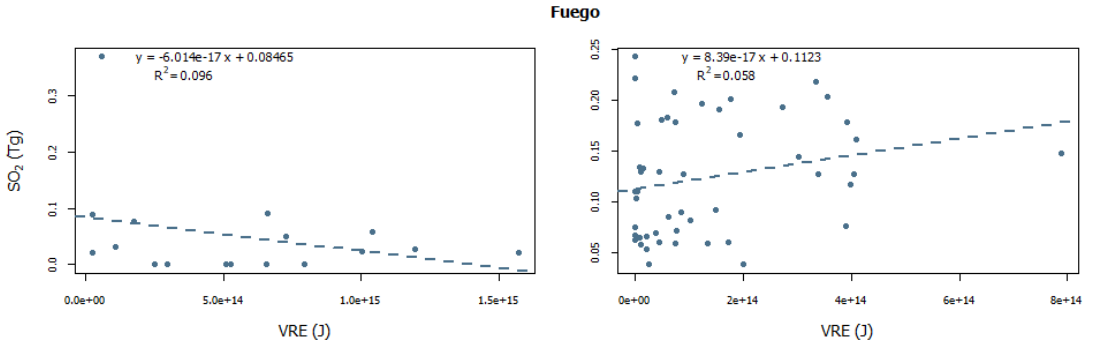
Fuego
y = -6.014e-17 x + 0.08465
R2 = 0.096
y = 8.39e-17 x + 0.1123
R2 = 0.058
SO2 (Tg)
VRE (J)
VRE (J)

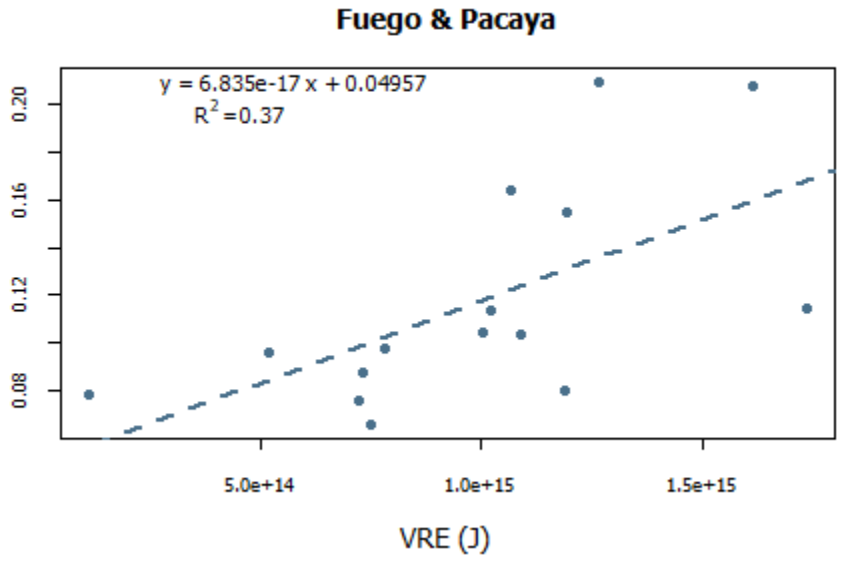
Fuego & Pacaya
y = 6.835e-17 x + 0.04957
R2 = 0.37
VRE (J)

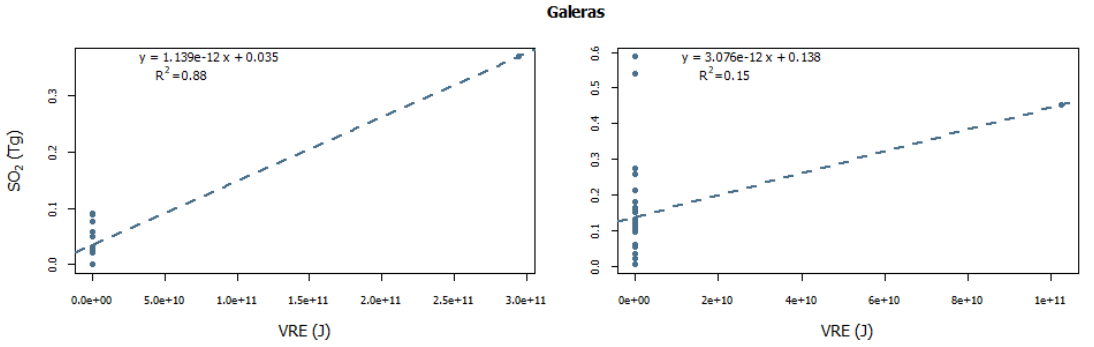
Galeras
y = 1.139e-12 x + 0.035
R2 = 0.88
y = 3.076e-12 x + 0.138
R2 = 0.15
SO2 (Tg)
VRE (J)
VRE (J)

Ijen

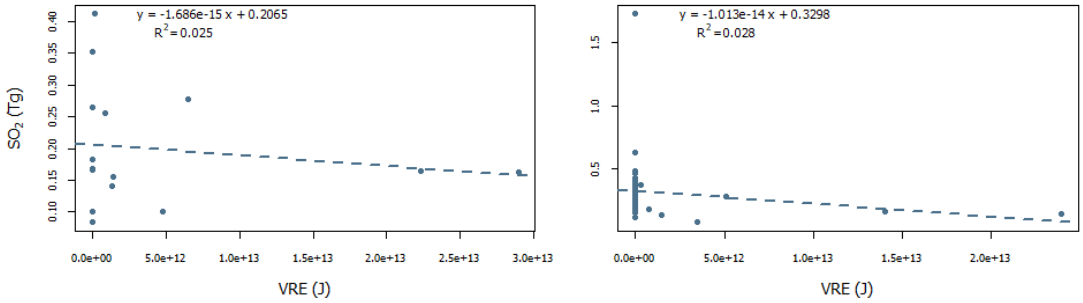

Karangetang

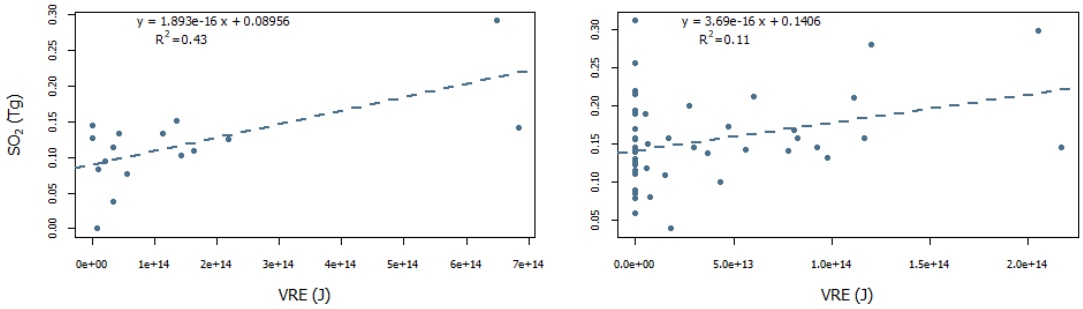

Karymsky

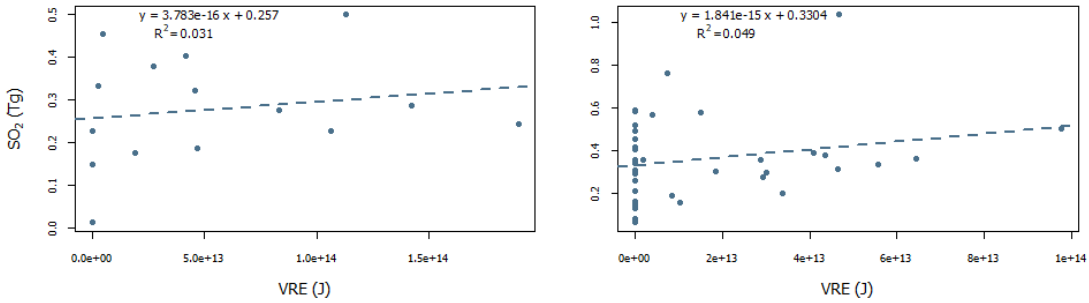

Kilauea

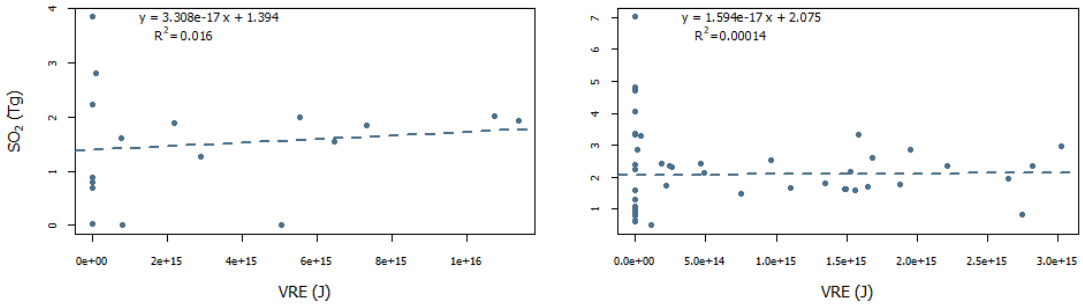

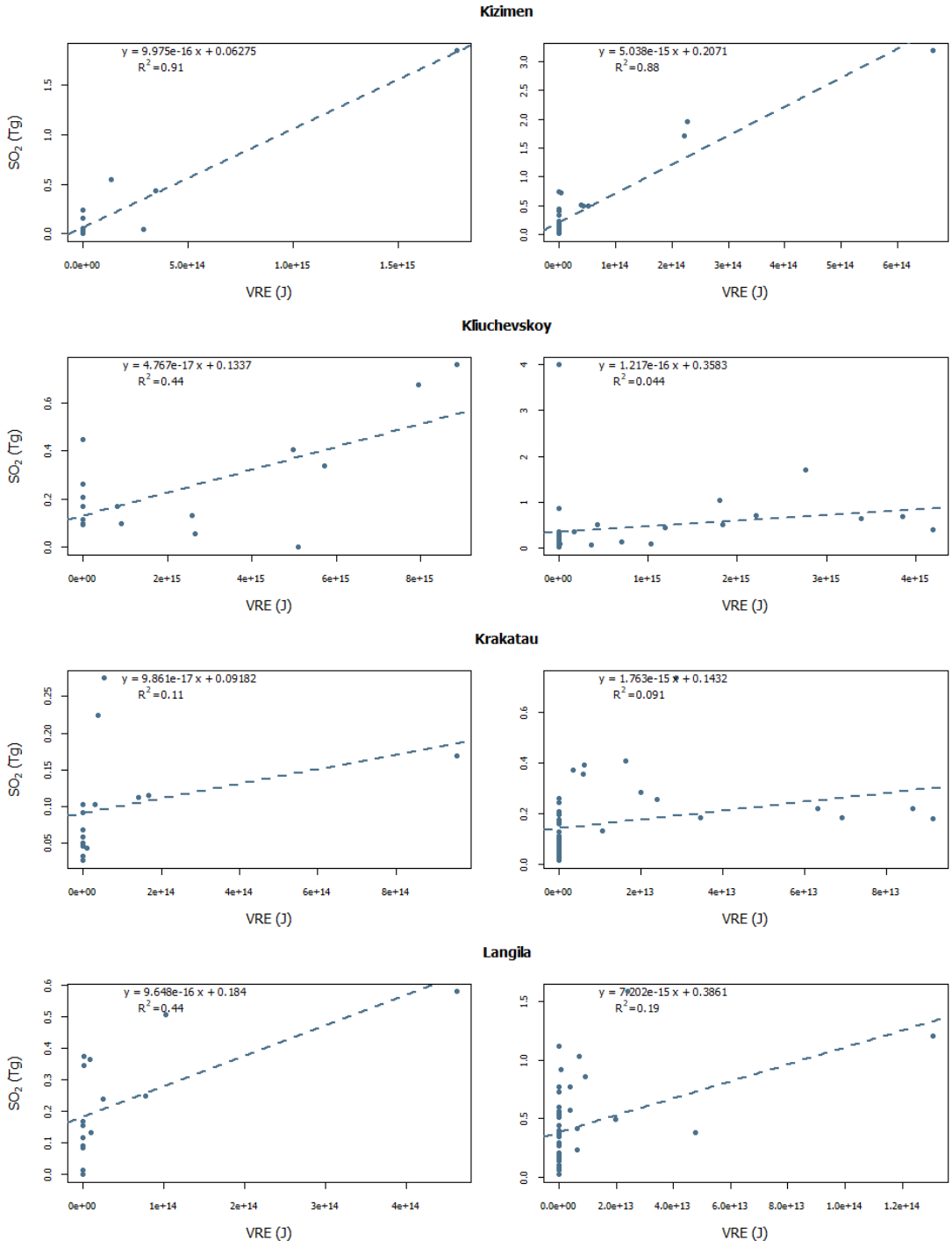
Kizimen
y = 9.975e-16 x + 0.06275
R² = 0.91
SO2 (Tg)
VRE (J)
y = 5.038e-15 x + 0.2071
R² = 0.88
VRE (J)
Kliuchevskoy
y = 4.767e-17 x + 0.1337
R² = 0.44
SO2 (Tg)
VRE (J)
y = 1.217e-16 x + 0.3583
R² = 0.044
VRE (J)
Krakatau
y = 9.861e-17 x + 0.09182
R² = 0.11
SO2 (Tg)
VRE (J)
y = 1.763e-15 x + 0.1432
R² = 0.091
VRE (J)
Langila
y = 9.648e-16 x + 0.184
R² = 0.44
SO2 (Tg)
VRE (J)
y = 7.202e-15 x + 0.3861
R² = 0.19
VRE (J)

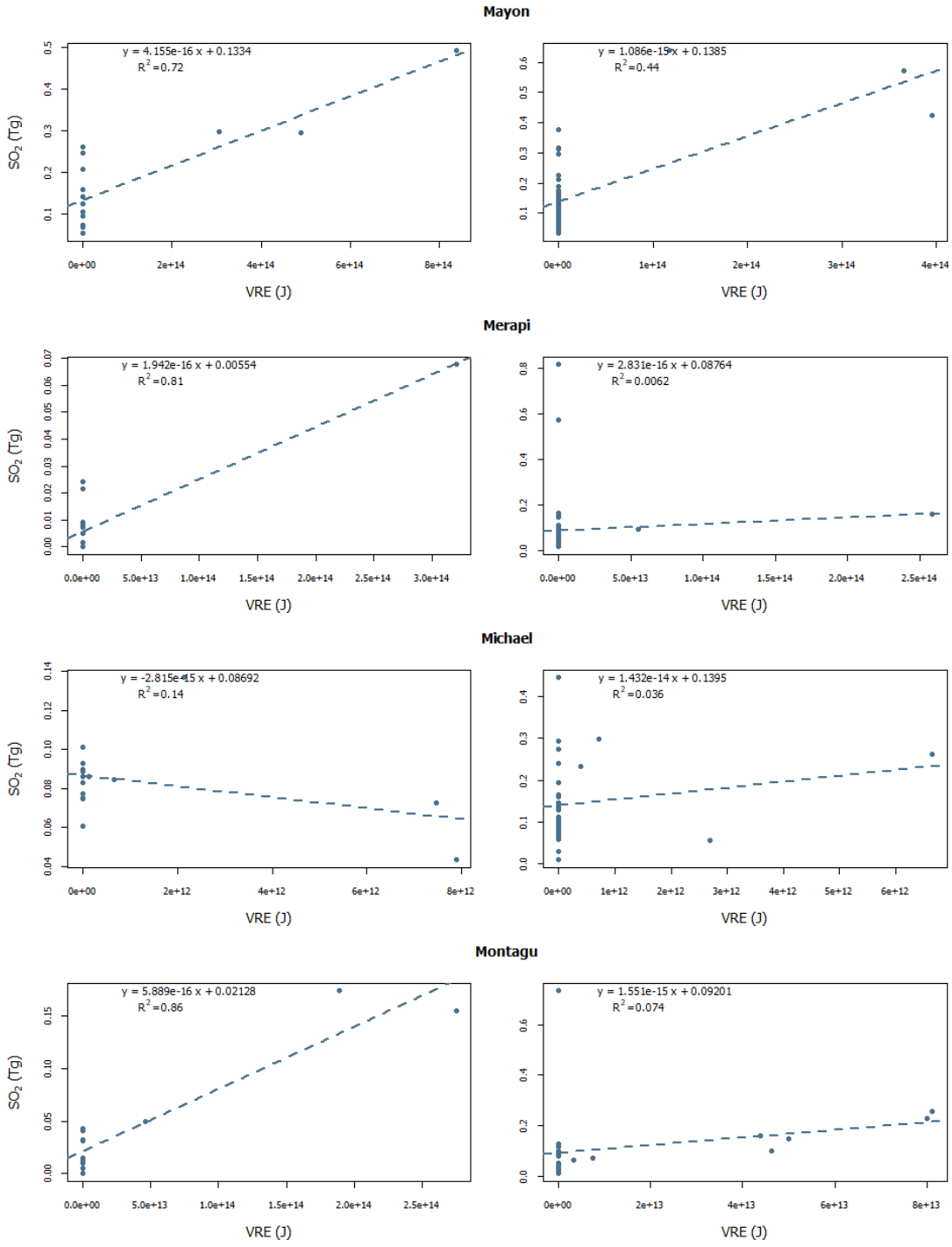
Mayon
y = 4.155e-16 x + 0.1334
R² = 0.72
y = 1.086e-15 x + 0.1385
R² = 0.44
Merapi
y = 1.942e-16 x + 0.00554
R² = 0.81
y = 2.831e-16 x + 0.08764
R² = 0.0062
Michael
y = -2.815e-15 x + 0.08692
R² = 0.14
y = 1.432e-14 x + 0.1395
R² = 0.036
Montagu
y = 5.889e-16 x + 0.02128
R² = 0.86
y = 1.551e-15 x + 0.09201
R² = 0.074
SO2 (Tg)
VRE (J)

Nevado del Ruiz

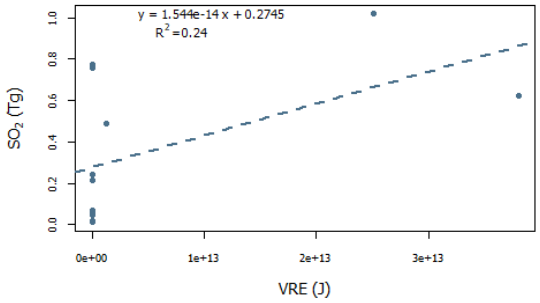

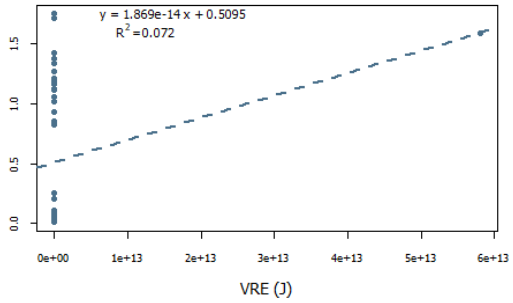

Nishinoshima

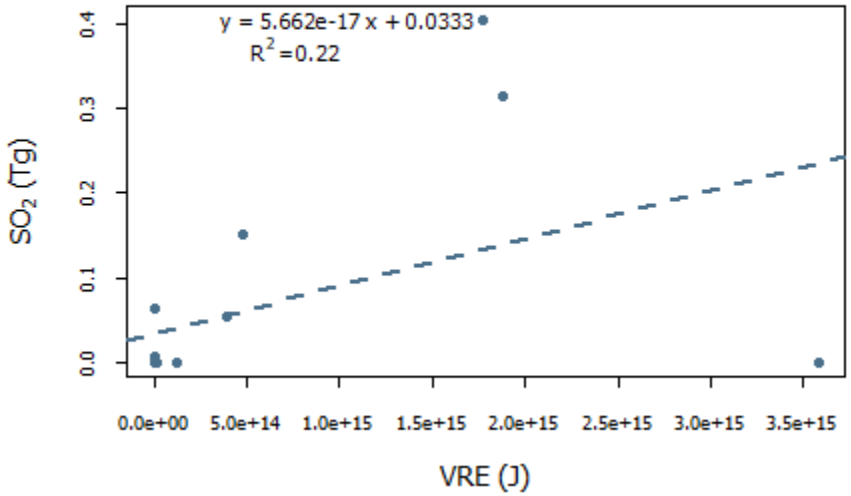

Nyamuragira

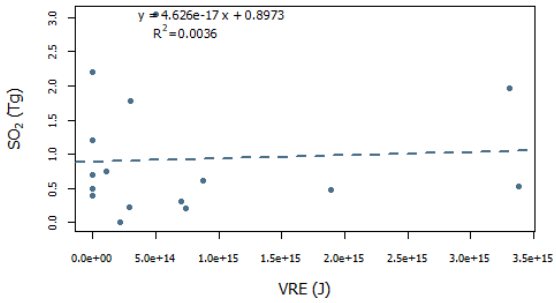

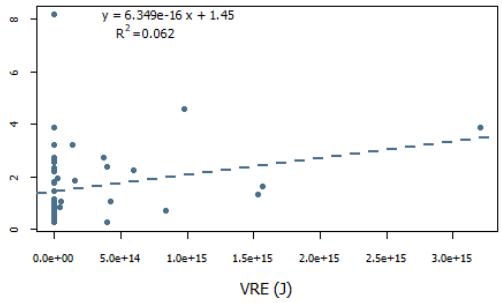

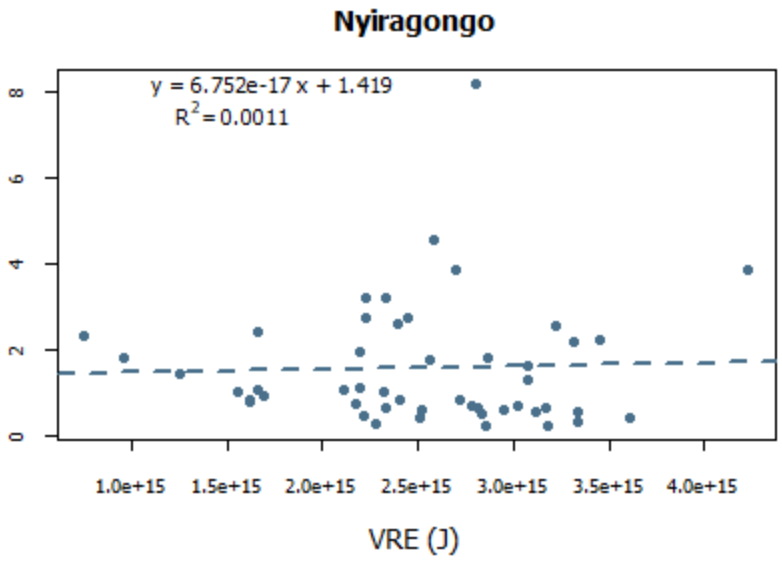
Nyiragongo
y = 6.752e-17 x + 1.419
R2 = 0.0011
0
2
4
6
8
1.0e+15
1.5e+15
2.0e+15
2.5e+15
3.0e+15
3.5e+15
4.0e+15
VRE (J)

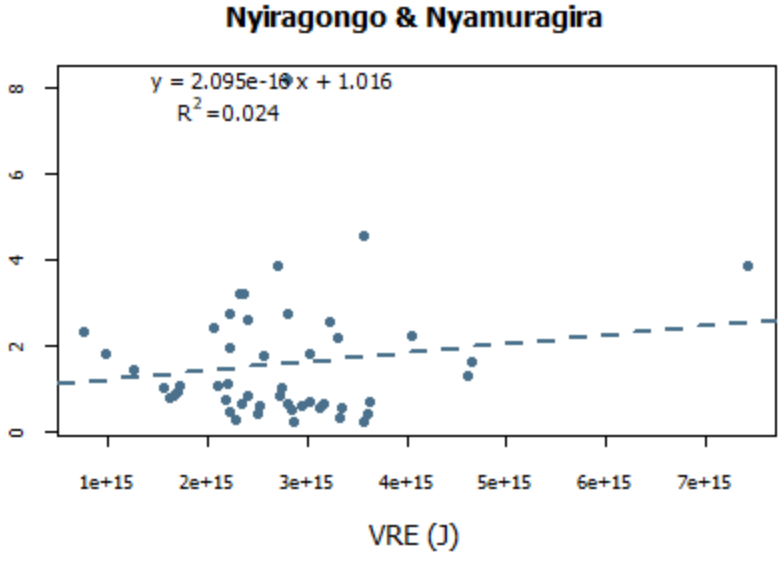
Nyiragongo & Nyamuragira
y = 2.095e-16 x + 1.016
R2 = 0.024
0
2
4
6
8
1e+15
2e+15
3e+15
4e+15
5e+15
6e+15
7e+15
VRE (J)

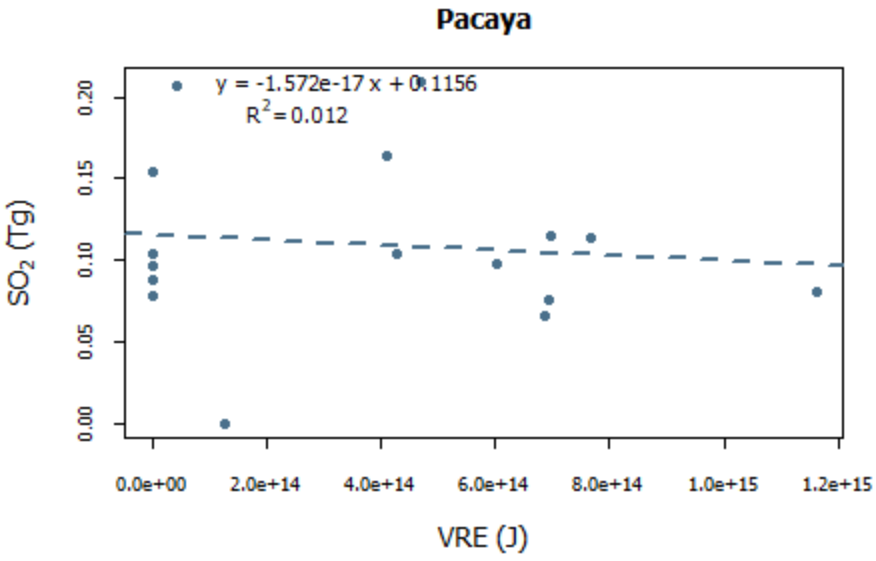
Pacaya
y = -1.572e-17 x + 0.1156
R2 = 0.012
SO2 (Tg)
VRE (J)

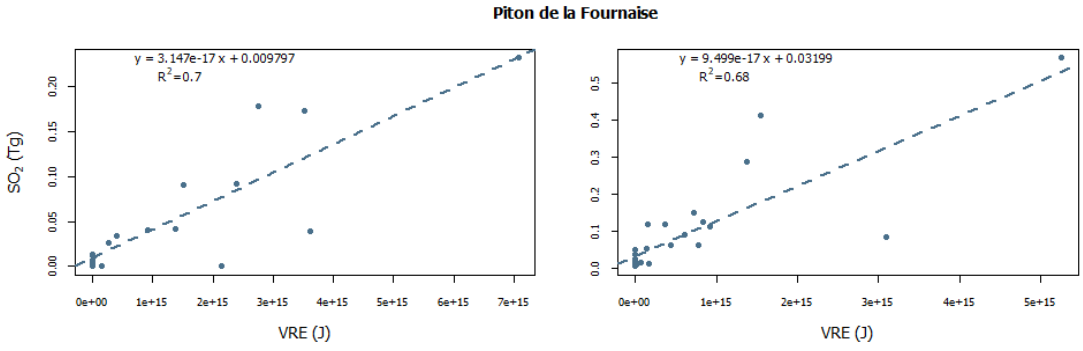
Piton de la Fournaise
y = 3.147e-17 x + 0.009797
R2 = 0.7
y = 9.499e-17 x + 0.03199
R2 = 0.68
SO2 (Tg)
VRE (J)

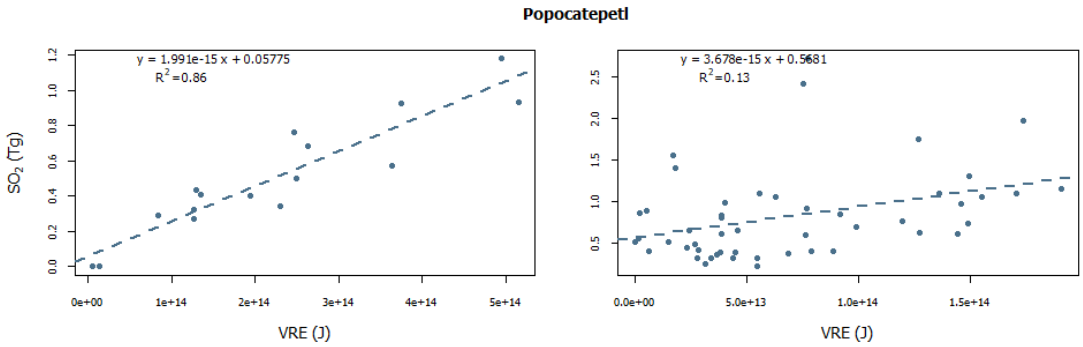
Popocatepetl
y = 1.991e-15 x + 0.05775
R2 = 0.86
y = 3.678e-15 x + 0.5681
R2 = 0.13
SO2 (Tg)
VRE (J)

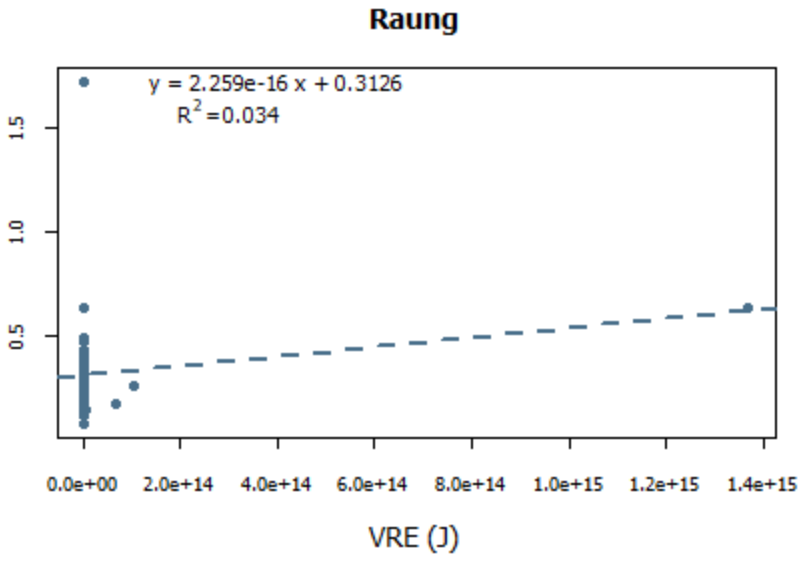
Raung
y = 2.259e-16 x + 0.3126
R2 =0.034
1.5
1.0
0.5
0.0e+00
2.0e+14
4.0e+14
6.0e+14
8.0e+14
1.0e+15
1.2e+15
1.4e+15
VRE (J)

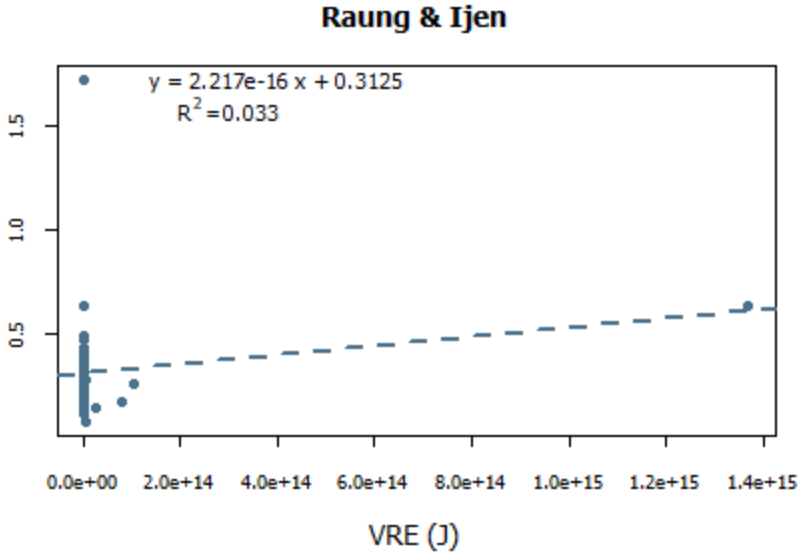
Raung & Ijen
y = 2.217e-16 x + 0.3125
R2 =0.033
1.5
1.0
0.5
0.0e+00
2.0e+14
4.0e+14
6.0e+14
8.0e+14
1.0e+15
1.2e+15
1.4e+15
VRE (J)

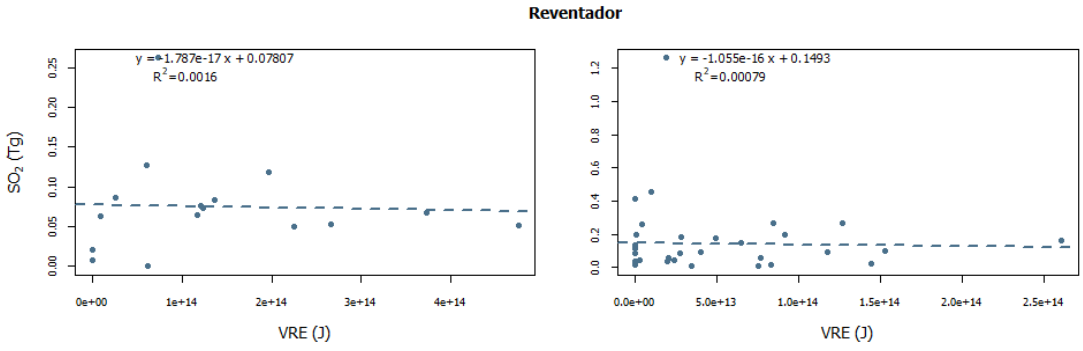
Reventador
y = -1.787e-17 x + 0.07807
R2 =0.0016
SO2 (Tg)
0.25
0.20
0.15
0.10
0.05
0.00
0e+00
1e+14
2e+14
3e+14
4e+14
VRE (J)
y = -1.055e-16 x + 0.1493
R2 =0.00079
1.2
1.0
0.8
0.6
0.4
0.2
0.0
0.0e+00
5.0e+13
1.0e+14
1.5e+14
2.0e+14
2.5e+14
VRE (J)

Rinjani

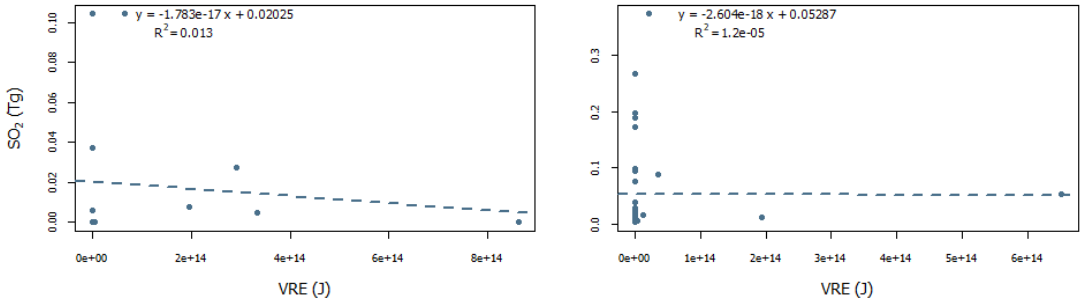

Sabancaya

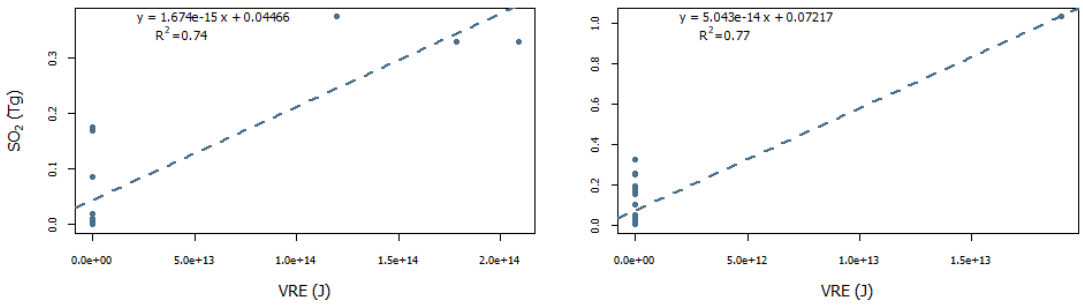

Sakurajima

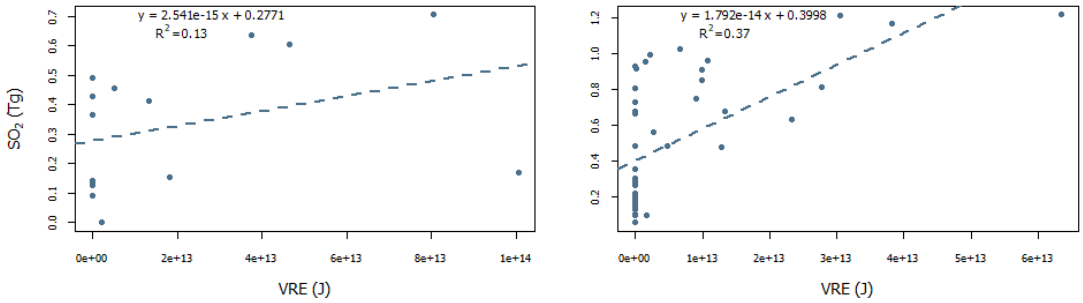

San Cristobal

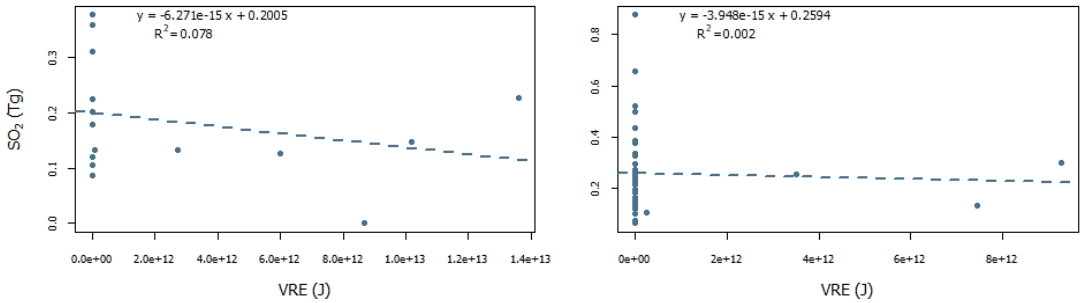

Sangay

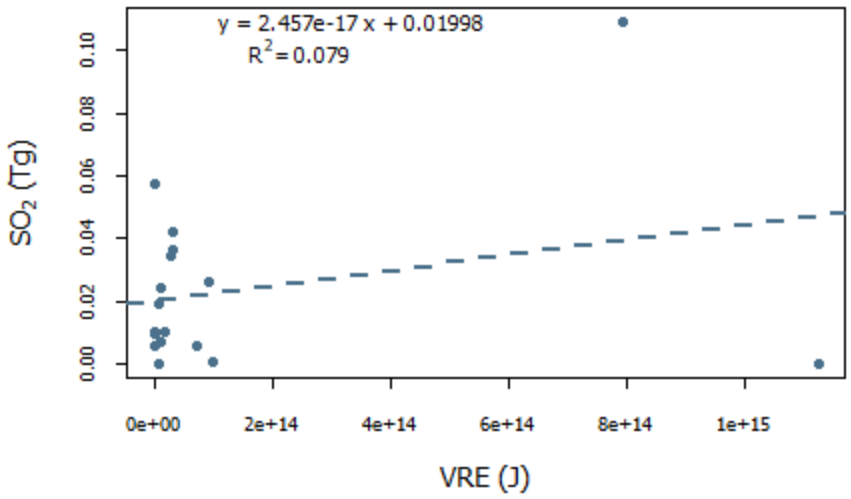

Sangeang Api

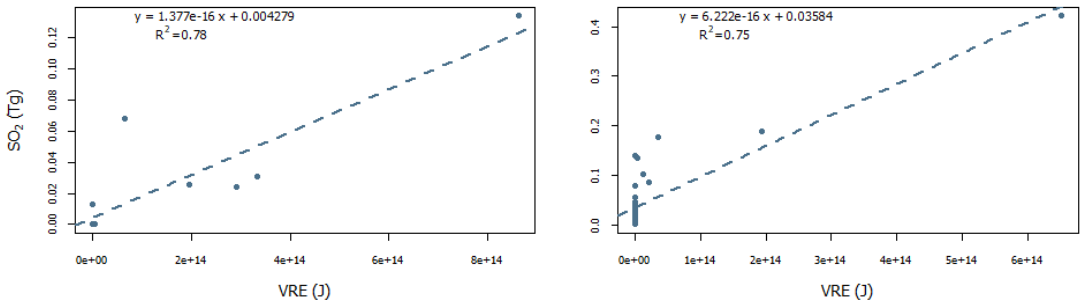

Santiaguito

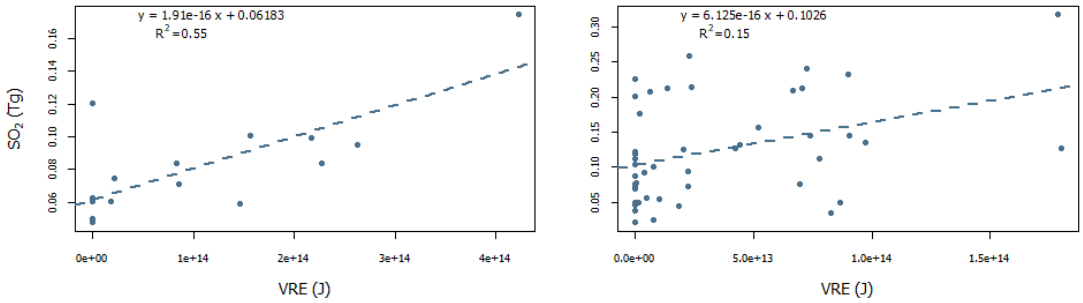

Shishaldin

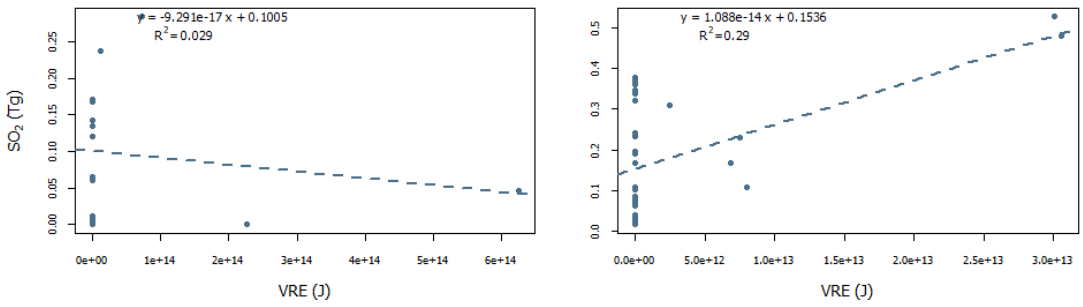

Shiveluch

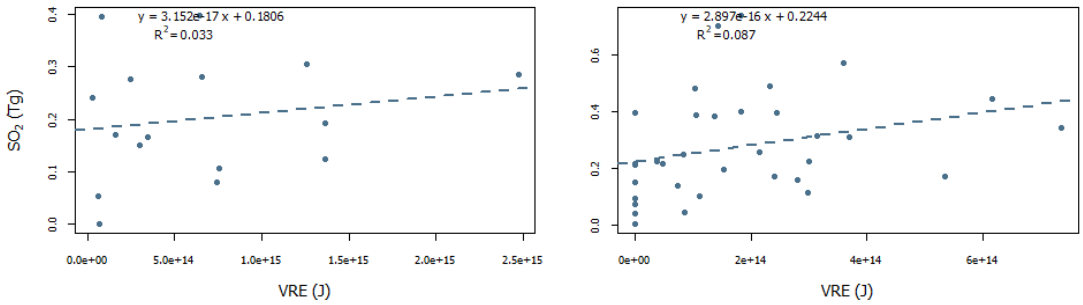

Sinabung

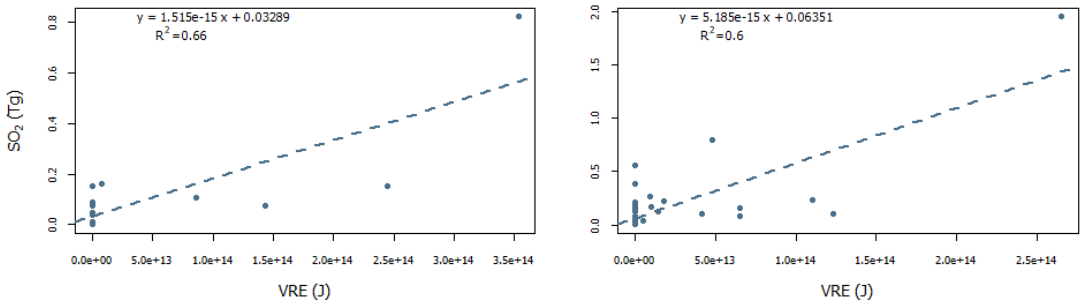

Slamet

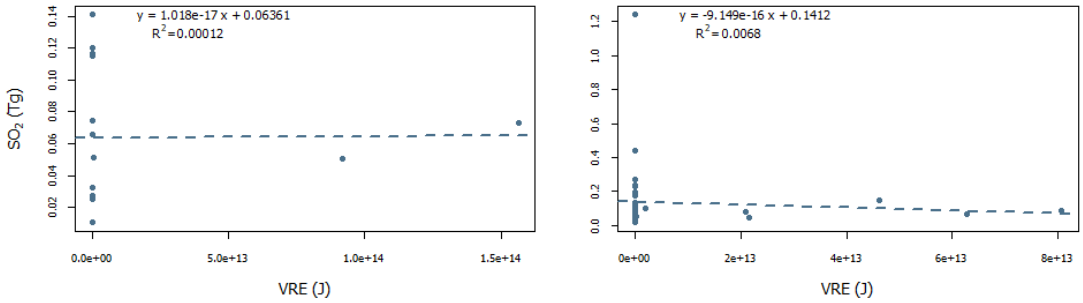

Stromboli

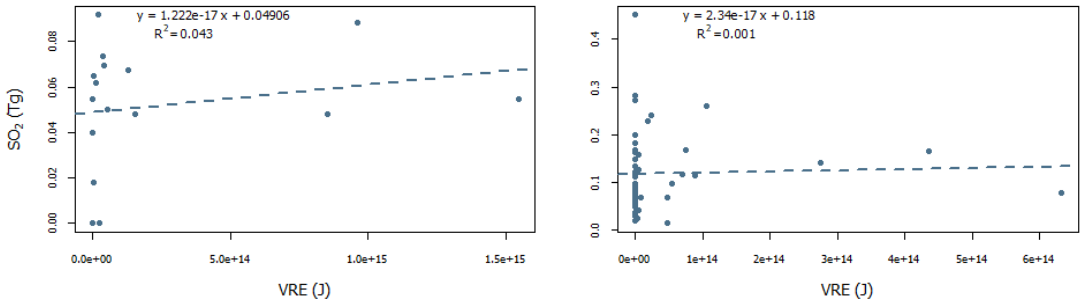

Soufriere Hills

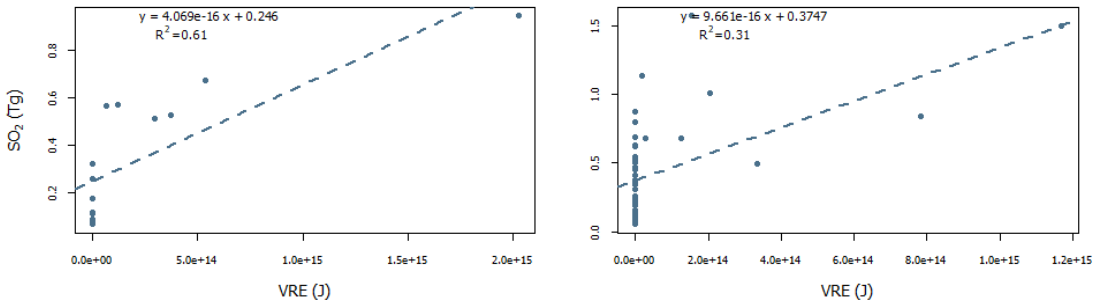

Suwanosejima

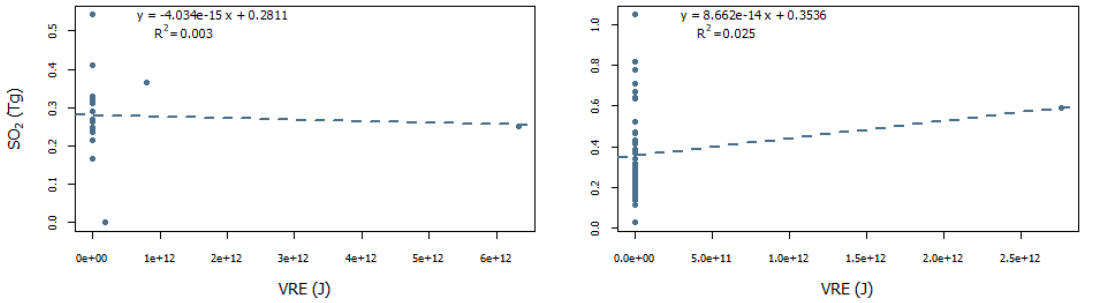

Tinakula

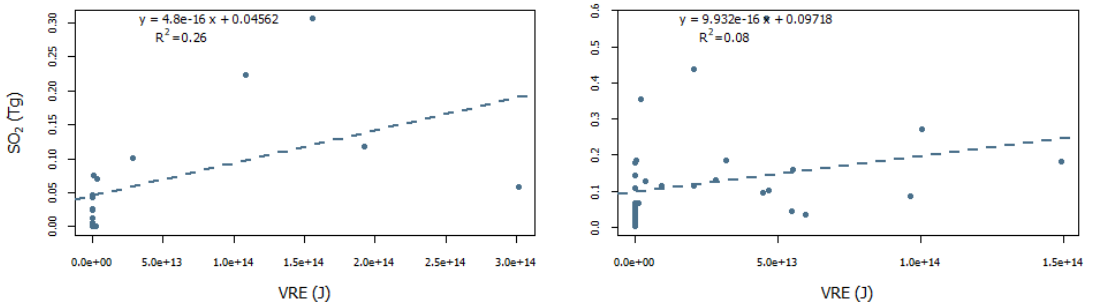

Tofua

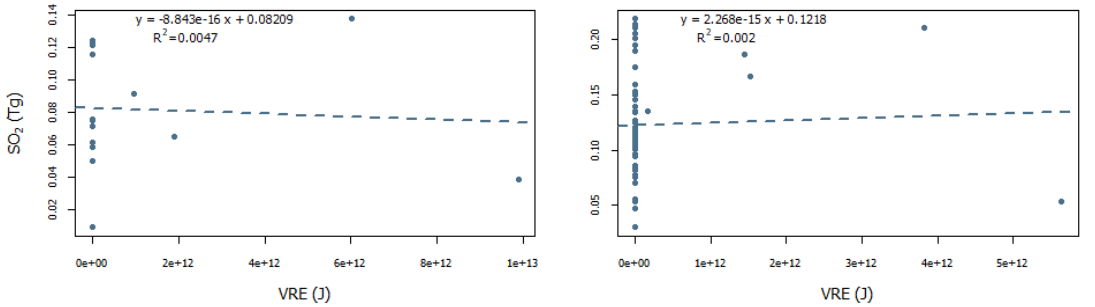

Tungurahua

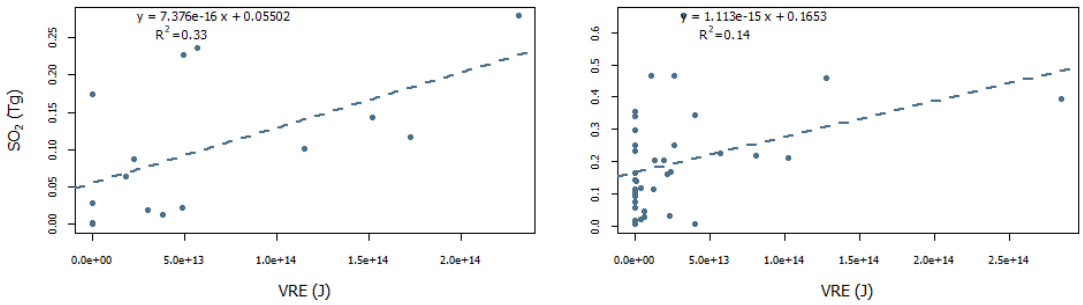

Veniaminof

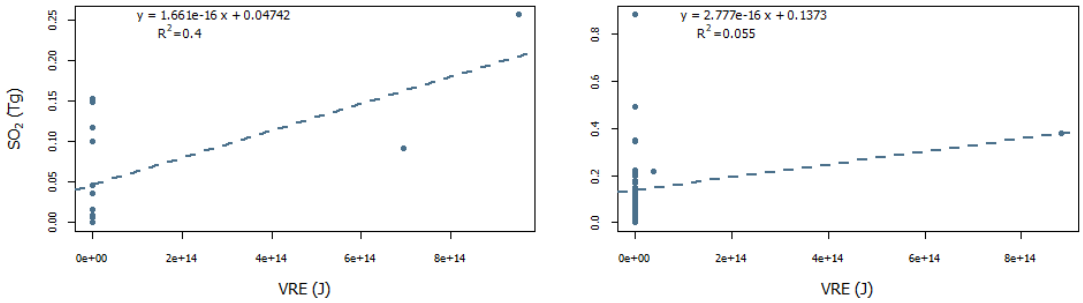

Villarrica

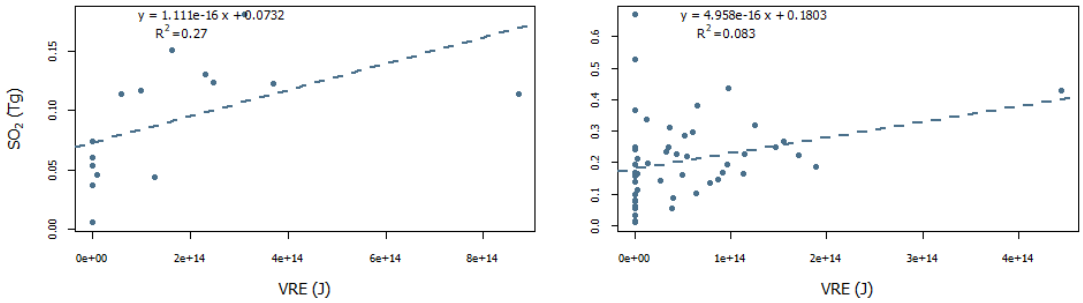

Yasur